First-principles studies on oxide nanoclusters in bcc Fe

DISSERTATION

zur Erlangung des akademischen Grades
Doctor rerum naturalium
(Dr. rer. nat.)

Vorgelegt
dem Bereich Mathematik und Naturwissenschaften
der Technischen Universität Dresden

von

Muthu Vallinayagam

geboren am 17.11.1988 in Mannar Kovil (Tamil nadu)

Eingereicht am 05. März 2020

Die Dissertation wurde in der Zeit von November 2016 bis May 2020 am Institut für Ionenstrahlphysik und Materialforschung am Helmholtz-Zentrum Dresden-Rossendorf e.V. angefertigt.

1. Gutachter: Prof. Dr. Jürgen Fassbender
Technische Universität Dresden, Deutschland

2. Gutachter: Prof. Dr. Karsten Albe
Technische Universität Darmstadt, Deutschland

3. Gutachter: Prof. Dr. Roger Smith
Loughborough University, UK

Datum der Einreichung: 05.03.2020

Datum der Verteidigung: 21.07.2020

….to my mother

Abstract

The worldwide growing demand for clean energy leads to necessity for new energy generation methods. Nuclear power generators are an excellent solution for these demands. The feasibility of nuclear power production depends on the performance of structural materials under the harsh conditions in nuclear reactors such as high radiation flux and high temperature. The development of structural materials to withstand such conditions is a big challenge and crucial for advanced nuclear fission and fusion reactors. Several materials are developed, amongst them Oxide Dispersion Strengthened (ODS) steels also called Nanostructured Ferritic Alloys (NFA). NFA consist of Fe-Cr based ferritic/martensitic steels that contain highly dispersed nanometer-size Y-Ti-O nanoclusters, and are manufactured via powder metallurgy. The presence of nanoclusters leads to high temperature stability and radiation resistance. Despite many research activities using advanced analytical techniques such as Transmission Electron Microscopy and Atom Probe Tomography as well as theoretical calculations many properties of the nanoclusters, such as the detailed atomic structure and composition as well as their efficiency for trapping He, vacancies and self-interstitial atoms (SIA), are still not completely understood.

In the first part of this thesis work, six different structural models for atomic clusters in bcc Fe which may contain O, Y, Ti, and vacancies (v) are investigated by Density Functional Theory (DFT) calculations. Results for clusters with identical numbers of constituents (O, Y, Ti, and v) are compared. The most important finding consists in the statement that the data on the stability or energetics of the relaxed clusters are comparable although their atomic configurations are often different. This contradicts the prevailing opinion in the related theoretical literature that favors the so-called structure-matching model, which is also investigated in this work. In all studied cases, the absolute value of the total binding energy per cluster constituent becomes lower if Y is partially replaced by Ti, i.e. the driving force for the growth of O-Y clusters is higher than that of O-Y-Ti clusters. This may be correlated with the experimental observation that the presence of Ti leads to a reduction of the size of the oxide clusters in NFA and to a higher dispersion. A further major result is the finding that cage-

like (CL) clusters and clusters with an oxygen atom in the center (cage) have a similar total binding energy. If Ti is not present such clusters are slightly more stable than the corresponding CL clusters. The opposite holds for clusters with Ti. It is also shown that adding O atoms to CL cluster leads to structures with O in the center. Vacancies are an important for the stabilization of the cluster due to the very strong binding with O. We infer that the Ov pair may be the origin for cluster nucleation growth. Because of limited computational resources, the dimension of clusters investigated by DFT is still below or close to the limit of the experimental resolution of methods allowing for a simultaneous determination of atomic structure and composition of the clusters. These small clusters may be considered as nuclei for further structural evolution and growth during which a selection of the most favored cluster structures could occur.

In the second part of the work four different cluster structures are used to investigate their ability to trap irradiation defects He, v and SIA. These defects are inserted on different positions inside and in the environment of the clusters, the total energy of the corresponding supercell is minimized by DFT, and the binding and incorporation energy of the three kinds of defects is determined. He in the center of a CL cluster is more stable than on interfacial vacant sites (IVS). In CL O-Y clusters, He on an IVS is more stable than in clusters with oxygen in the center, whereas there is no significant difference between the two kinds for clusters with Ti. Up to a distance of 1.5 times the iron lattice constant from the cluster center He is not stable on most of the octahedral and tetrahedral interstitial sites in the Fe matrix. Instead, He is shifted towards positions closer to the cluster. Relaxation occurs to known IVS as well as to previously unknown interfacial interstitial sites (IIS). Moreover, two or three He atoms are placed on sites found to be stable after adding a single He. The corresponding binding and incorporation energies obtained after relaxation are nearly equal to the sum of the values for the interaction with a single He atom. However, placing He dimers or trimers in the environment of a vacancy that belongs to the cluster may also lead to relatively low values of the incorporation energy. Also, He jump barriers between interfacial sites and the center of CL clusters are determined. In the CL O-Y cluster, the barriers are lower than in the CL O-Y-Ti cluster, i.e. trapping and release of He is easier in the former than in the latter. The main reason for the high He trapping efficiency is the low electron density in the empty regions of the oxide-like structure of the clusters. Vacancy and SIA interaction with the clusters is also attractive. The binding energy of a vacancy strongly depends on the site where the vacancy is inserted while in all the studied cases the SIA is annihilated at the cluster-iron interface. Present results clearly demonstrate that the oxide-based nanoclusters are strong traps for irradiation-induced defects, which is in agreement with experimental findings.

Contents

1. Introduction

1.1 Introduction

Growing energy demands, reduction of CO_2 emission on energy production and possible alternative for fossil fuels increase interest on nuclear power plants including both fission and fusion reactors. The power generation from fossil fuel contributes to significant greenhouse gas emissions, which influences the climate change trend. Opting for nuclear power plant leads to advantage of pollution less power production. For many decades scientists are developing the nuclear power plants in many aspects *[1-4]*. The viability of nuclear power production depends on the performance of structural materials under the harsh conditions in nuclear plants *[5-7]*. The structural materials of nuclear plants face burdens such as combination of intense radiation fluxes, high temperature, high stresses, chemically aggressive coolant etc., *[6, 7]*. The major issues experienced by structural materials are varying according to the operating temperature and irradiation damage levels. These problems are characterized into radiation hardening and embrittlement ($<0.4T_M$, >0.1 dpa), phase instabilities due to irradiation-induced precipitation ($0.4\text{-}0.6T_M$, >10 dpa), irradiation creep ($<0.45T_M$, >10 dpa), void swelling ($0.3\text{-}0.6T_M$, >10 dpa), and high temperature embrittlement ($>0.50T_M$, >10 dpa) *[6-8]*. The terms in the parenthesis represent the operating condition characterized in units of melting temperature of the structural material T_M , and in units of displacements per atom (dpa) caused by irradiation. Irradiation effects are mainly caused by the formation of vacancies, self-interstitial atoms, and the incorporation of the transmutation product He *[9, 10]*.

1.2 Structural Materials

The choice of structural materials for nuclear plants (for reactor vessel and fuel cladding tubes) is highly important for reactor stability and efficiency. Essential demands for structural materials are mechanical strength, ductility, toughness, dimensional stability, fabricability, heat conductivity, radiation resistance including low susceptibility to induced radioactivity and optimum neutron absorption, etc. *[2]*. Generally, materials with high strength offer low ductility and vice versa. Fcc iron-based alloys are high ductile and bcc alloys provides high strength. In addition, bcc materials provide little work hardening compared with the fcc materials. The material selection varies according to the goals of nuclear plant generation. In a generation GEN IV fission reactor the maximum irradiation dose will be 30-100 dpa, the operation temperature will be between 600-1000 °C, and the He concentration is estimated to be ~3-10 appm *[11]*. In other advanced nuclear reactors for fission and fusion the challenges for properties of structural materials are similar or higher. Simple austenitic stainless steels of type-316 and type-304 (with fcc structure of the iron matrix) were utilized as core component alloys for prototypes and demonstration fast breeder reactors *[12]*, but exhibited significant void swelling. In Fig. 1.1, void swelling due to irradiation in different alloys is compared. On the other hand, austenitic stainless steels were still favored for fuel pin cladding due to their strength characteristics up to 650 °C *[13]*. For this application, the swelling resistance was improved using cold worked Ti, P, and Si modified austenitic stainless steel. This material contains fine-scale and disperse trapping centers for He and intrinsic point defects and has increased creep resistance due to dislocation pinning at these precipitates. However, even such an advanced austenitic stainless steel still shows significant swelling compared to ferritic or ferritic/martensitic (FM) steel. Also the induced radioactivity due to presence of Ni is an essential problem.

During irradiation FM steel exhibits a lower dislocation bias due to the prevailing bcc structure of the Fe matrix. In this manner the excess of vacancies is lower than in austenitic material which leads to slower formation of embryonic cavities with He and vacancies and slower subsequent void growth and, consequently, to less swelling. FM steels also possess higher thermal conductivity and lower thermal expansion than austenitic steels, which provide improved resistance to thermal stresses for a reactor operating in a pulsed mode *[14]*. The addition of Cr leads to corrosion-resistant FM steels. On the other hand, the ductile-brittle transition temperature (DBTT) of the material should be as low as possible. For 9 % Cr content this temperature is lowest. As compromise between high corrosion resistance and low DBTT

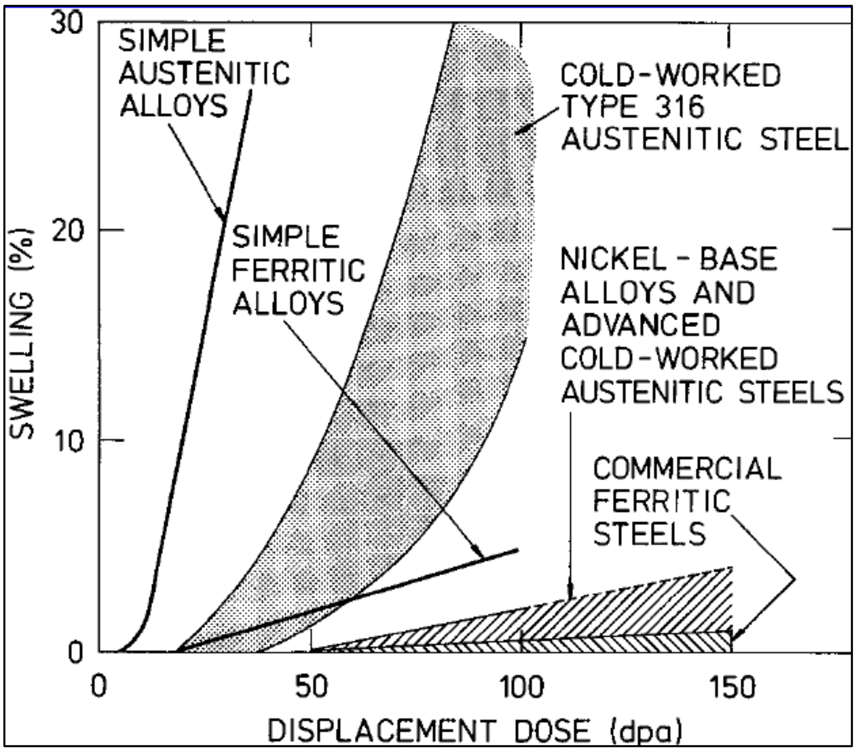

Fig. 1.1: Comparison of swelling in different alloys due to irradiation. The figure is from Ref. *[12]*

in practice the Cr content is chosen between 9 and 12 %. As already mentioned above the irradiation level in advanced reactors is significant so that some alloying elements in FM Fe-Cr steel become highly radioactive. In order to lower the induced radioactivity Reduced Activation FM steel was developed where alloying elements such as Mo and Nb were replaced by W and Ta, respectively (see e.g. *[15]*). However, the utilization of FM steels is limited to the temperature range of 550–650 °C due to the decrease of tensile and creep strength above 700 °C *[5]*. For high temperature application, further development of structural materials is required. This led to the concept of Oxide Dispersion Strengthened (ODS) steels, also called as Nanostructured Ferritic Alloys (NFA). Furthermore, a promising alternative concept, called Castable Nanostructured Alloys (CNA) is presently discussed, which is based on RAFM Fe-Cr steel with MX nanoclusters, with M=V, Ta, or Ti, and X=C, or N (see e.g. *[16]*). While ODS steels must be obtained using cost-intensive powder metallurgy, CNA may be produced using conventional casting technology.

1.3 Oxide Dispersion Strengthened (ODS) steels

For the first time Fisher [17] produced 13–25% Cr ODS ferritic steels via the mechanical alloying and subsequent hot extrusion powder processing route. These materials were marketed in the 1980s as MA956 and MA957. ODS steels contain a high density of uniformly distributed oxide-based nanoscale particles or nanocluster. ODS steels or ferritic/martensitic steels (FM) are promising candidates for structural materials of future nuclear fusion and fission reactors [18-22]. Compared to FM steel the NFA exhibit two remarkable properties: (i) High-temperature stability: Up to about 1200 °C the number and size of the oxide nanoparticles do not change considerably [18, 21-23]. This leads to significantly improved high-temperature yield and creep strength since mobile dislocations can be effectively blocked by the nanoclusters [18, 19, 21]. (ii) Radiation resistance: The nanoclusters can act as sinks for intrinsic point defects and helium. In this manner irradiation swelling can be retarded significantly [18, 21, 22]. Also, a reduction of radiation hardening is found in comparison with conventional Fe-Cr FM alloys [21]. Furthermore, the nanoclusters are relatively stable against very high-dose irradiation at elevated temperature as demonstrated by ion irradiation [22]. The nanoclusters contain Y and O which have a very low solubility in bcc Fe [24]. Thus, conventional casting techniques are not viable for introducing Y and O into the FeCr matrix.

NFA are produced by means of powder metallurgy which involves the following main technical steps: (i) high-speed milling of Y_2O_3 (yttria) particles and mechanical alloying with particles obtained by gas atomization of advanced Fe-Cr alloys that may contain small concentrations of other metals (Ti, Zr, etc.), (ii) hot consolidation (hot isostatic pressing, hot extrusion, or spark plasma sintering), and (iii) further thermal and mechanical treatment. An example is depicted in Fig. 1.2. It was demonstrated that the addition of Ti reduces the average size of the oxide nanoparticles which may improve the high-temperature strength as well as radiation resistance [18, 19, 21]. It is generally assumed that in the production of ODS steels Y_2O_3 is dissolved by the high-speed milling, and that during the subsequent thermal processing the O-Y-Ti or O-Y (if Ti is not present in the alloy) nanoclusters are formed [21]. Mechanical alloying creates a lot of open volume and corresponding vacancies, di-vacancies etc. were found near solute atoms such as O and Y *[25]*. This leads to the formation of metastable nuclei, which may be further transformed in the subsequent thermal treatment. The density and configuration of the nanoclusters observed after all production steps strongly depends on the processing route applied and corresponds to a certain metastable thermodynamic state. It must be also mentioned that the existence of vacancies is a precondition for the volume diffusion of Y and Ti in bcc Fe (cf. *[26, 27]*) which may occur during the annealing stage, but for Y dislocation pipe diffusion was also discussed *[21]*.

The formation of ODS material as well as the properties of the nanometer-size oxide clusters and the reasons for their high-temperature stability and radiation resistance are not yet fully understood *[18-22, 28]*, although continuous progress has been made by experimental investigations with advanced analytical tools such as high-resolution or scanning and element-specific Transmission Electron Microscopy (TEM), Atom Probe Tomography (APT), Small-Angle Neutron Scattering (SANS), Small-Angle X-ray Scattering (SAXS), Positron Lifetime Spectroscopy (PLS), and X-ray diffraction (XRD). There exists a plethora of papers concerning the nature of the O-Y-Ti or O-Y nanoclusters. In a recent review paper the properties of the most relevant clusters with a size below about 5 nm were discussed *[21]*. It was stated that several distinct atomic configurations were proposed by the different authors, in particular nonstoichiometric crystalline or amorphous structures, which may contain vacancies and Fe atoms (see also *[29]*), a rock salt structure, as well as near stoichiometric Y_2O_3, or $Y_2Ti_2O_7$ and Y_2TiO_5 oxides. In the review paper it was concluded that the near-stoichiometric oxide structures should be most probable, with different orientation relationships with regard to the bcc host crystal *[21, 30]*. An interesting example is the work of Sakasegawa et al. *[31]* who analyzed the chemical composition and size of Y-Ti-O nanoclusters in the ODS alloy MA957 using Field-Emission-Gun TEM and Energy Dispersive X-ray Spectrometry. One of their results is given in Fig.1.3. The data show that up to a size 15 nm the ratio Y/Ti is less than 1. For nanoclusters with sizes larger 20 nm the Y/Ti ratio saturates at a level between 1 and 1.5. This was interpreted by the existence of a large percentage of clusters with $Y_2Ti_2O_7$ and Y_2TiO_5 stoichiometry. The findings of Sakasegawa et al. *[31]* demonstrate that the composition and structure of nanoclusters may vary with size and the

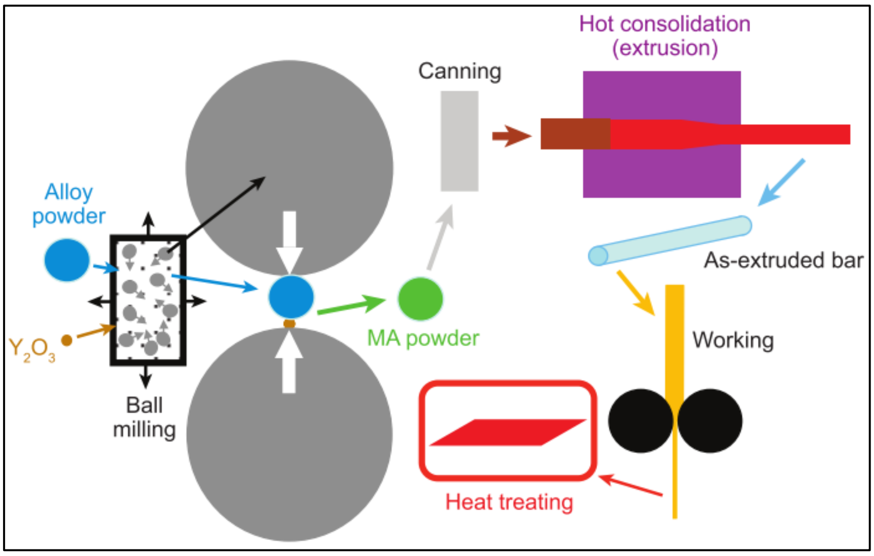

Fig. 1.2: Schematic of steps involved in ODS alloys production. i) ball milling of yttria, ii) mechanically alloying (MA) of Y and O with metal powders, iii) canning, vi) hot consolidation (extrusion), and post consolidation thermal and mechanical treatment. The sketch is taken from Ref. *[16]*

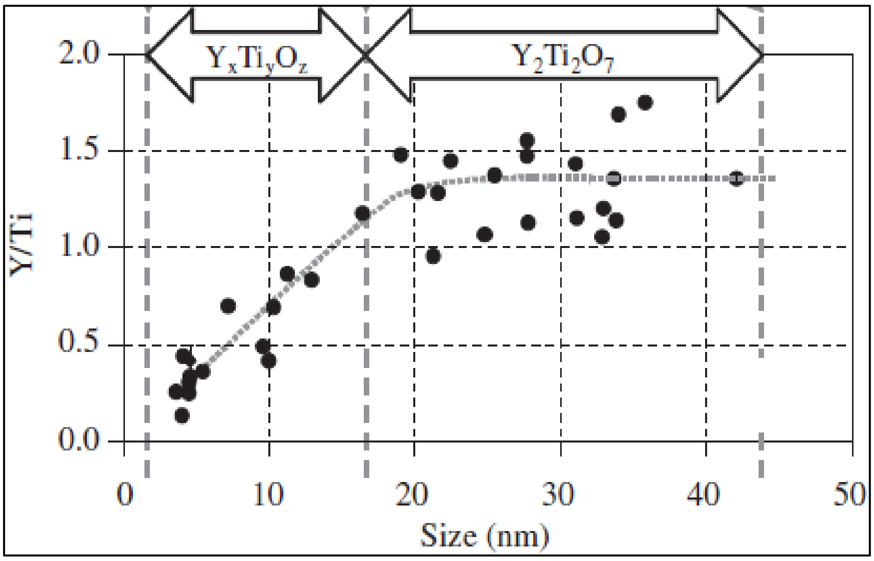

Fig. 1.3: Y/Ti ratio of nanocluster in the MA957 ODS alloy. The figures is from Ref**.** *[31]*.

most abundant and relevant small cluster may be non-stoichiometric oxides. On the other hand, London et al. *[32]* considered three different ODS steels Fe-0.3Y_2O_3 , Fe-0.2Ti-0.3Y_2O_3

and Fe-14Cr-0.2Ti-0.3Y_2O_3 to probe effect Ti and Cr on structure and chemistry of nanoclusters using TEM, APT and synchrotron-XRD. Their result reveals that Ti and Cr addition reduces nanocluster size. The energy-filtered TEM measured mean size of nanoclusters are 9.6 nm in Fe-0.3Y_2O_3, 7.7 nm in Fe-0.2Ti-0.3Y_2O_3, and and 3.7 nm in Fe-14Cr-0.2Ti-0.3Y_2O_3. APT results show that Cr segregates as shells around the nanoclusters. Combining TEM and XRD analysis predicts that nanoclusters are stoichiometric oxides, i.e. monoclinic and bcc-Y_2O_3 in Fe-0.3Y_2O_3, fcc- $Y_2Ti_2O_7$, as well as orthorhombic Y_2TiO_5 in Fe-0.2Ti-0.3Y_2O_3 and Fe-14Cr-0.2Ti-0.3Y_2O_3. Many experimental studies were performed in order to investigate the properties of the most abundant and relevant small clusters under irradiation. For example, Edmondson et al. *[33]* showed by combined APT and TEM analysis of He-ion implanted samples that about 50% of the He bubbles are located on nanoclusters, the rest on coarse precipitates, dislocations, grain boundaries, and on matrix sites. Nano-indentation based analysis on radiation induced hardening concludes that the nanoclusters are the most important sinks for point defects created by Fe-ion implantation *[34]*.

Besides experimental investigations with advanced analytical methods atomic-scale theoretical studies and computer simulations can significantly contribute to improve the knowledge on structure and properties of the Y-O and Y-Ti-O nanoclusters in NFA. In particular the structural and energetic properties of these nanoclusters were studied by many theoretical studies *[35-45]*. A detailed review on the literature will be given in chapter 3.

Atomic-scale theoretical investigations and computer simulations can also essentially contribute to the understanding of the interaction of the nanoclusters with He atoms, vacancies, and self-interstitial atoms. Several authors performed Density Functional Theory (DFT) calculations in order to investigate the He storage in the pure oxides (in Y_2O_3, $Y_2Ti_2O_7$, and Y_2TiO_5) *[46-53]*, at the interface between oxide and bcc Fe *[54-56]*, and in a system with the bcc Fe matrix containing O-Y and O-Y-Ti oxide clusters *[45, 57, 58]*. These studies revealed that in these oxides the He incorporation energy is significantly lower than in pure Fe. A detailed discussion of theoretical literature on storage capabilities of the nanoclusters for He, vacancies and self-interstitial atoms will be performed in chapter 4.

1.4 Objectives and overview of the thesis

Despite the theoretical work done by several authors there are still many open questions concerning the structure and stability of the nanoclusters and the their interaction with He and intrinsic point defects. Using density functional theory the following main issues are addressed in this thesis:

- For the given numbers of Y, Ti, O atoms and vacancies, what are possible structures of the nanoclusters within a bcc Fe matrix, and what is the stability or energetics of these configurations?
- How the nanoclusters influence and trap irradiation-induced defects such as He, vacancies and self-interstitial atoms?

The thesis consists of five chapters and two appendices:

Chapter 1: *Introduction*

Chapter 2: *Computational methods*

First, the basis of density functional theory (DFT) is presented. Then the choice of the suitable parameters for obtaining correct results, such as plane-wave energy cutoff and number of k-points for Brillouin zone integration is explained. In the second part, the Nudged Elastic Band (NEB) method to determine migration barriers is shortly elucidated.

Chapter 3: Investigation of different structural models for O-Y and O-Y-Ti clusters in bcc Fe

Six different cluster structures are considered and the particular ground-state configurations and energetics are determined by DFT calculations. The results are compared for given number of O, Y, and Ti and vacancies in these clusters. Changes of cluster structure and energetics caused by adding additional O atoms to a given structure are studied. Also selected barriers for O jumps in the region of the cluster are investigated.

Chapter 4: *Interaction of O-Y and O-Y-Ti clusters embedded in bcc Fe with He, vacancies and self-interstitial atoms*

Most stable ground-state cluster configurations obtained in chapter 3 are considered to investigate their influence on irradiation-induced defects, namely He, vacancies, and self-interstitial atoms. Using DFT the binding energy of the defects to the cluster is calculated and the relaxed atomic configurations are determined. Furthermore, some barriers for He jumps from the rim of the cluster to the cluster center are calculated.

Chapter 5: *Conclusions and outlook*

Appendices

Appendix-A: Construction schematics and optimized results for Chapter 3

Appendix-B: Construction schematics and optimized results for Chapter 4

X ------------------------------ X

2. Computational method

2.1 Fundamentals of Density Functional Theory

The Density Functional Theory (DFT) is based on the seminal work of Hohenberg, Kohn, and Sham [59, 60]. In textbooks, different formulations of the Hohenberg-Kohn theorem(s) can be found. The subject is the (nondegenerate) ground state of an interacting many-electron system under the influence of an external (e.g. lattice) potential. The most important statements are:

> *The ground-state energy of the system is a unique functional of the ground-state electron density. The electron density that minimizes the energy functional is the true ground-state electron density which corresponds to the full solution of the many-electron Schrödinger equation.*

In this manner, the problem of solving the many-electron Schrödinger equation, with the ground-state wavefunction depending on 3N coordinates is replaced by the search for the minimum of the energy functional with respect to the electron density which depends only on three spatial coordinates.

The energy functional may be written in the following manner

$$E[n(\vec{r})] = T[n(\vec{r})] + V[n(\vec{r})] + U[n(\vec{r})] \tag{1}$$

where n, T, V, and U are the electron density, and the functionals of the kinetic energy, of the potential energy due to the external potential, and of the potential energy of the electron-electron interaction, respectively. In the case of a solid the expression for V is

$$V[n(\vec{r})] = \int V_{en}(\vec{r})n(\vec{r})d^3r \tag{2}$$

The potential V_{en} describes the Coulomb interaction (attraction) between one electron and the nuclei in a lattice. The quantity U describes the electrostatic interaction (repulsion) between the electrons, as well as their interaction due to the quantum-mechanical exchange and correlation effects

$$U[n(\vec{r})] = \frac{e^2}{2} \int \frac{n(\vec{r}) n(\vec{r}\,')}{|\vec{r} - \vec{r}\,'|} d^3r\, d^3r' + E_x[n(\vec{r})] + E_c[n(\vec{r})] \tag{3}$$

Furthermore, it is assumed that the kinetic energy T can be written in the same manner as in the case of a non-interacting electron system

$$T = \sum_{i=1}^{N} \int \psi_i^*(\vec{r}) \left(-\frac{\hbar^2 \nabla^2}{2m} \right) \psi_i(\vec{r}) d^3r \tag{4}$$

This relation is obtained by assuming that the total wavefunction is given by the Slater determinant which consists of a well-defined arrangement of single-particle wavefunctions ψ_i. The corresponding electron density is

$$n(\vec{r}) = \sum_{i=1}^{N} \left| \psi_i(\vec{r}) \right|^2 \tag{5}$$

with

$$\int \left| \psi_i(\vec{r}) \right|^2 d^3r = 1$$

Note that $\nabla = \frac{\partial}{\partial \vec{r}}$, and $\hbar$ is the Planck constant divided by 2π, and m is the electron mass. Using Eq. (4) in the expression for $E[n(\vec{r})]$, one implicitly assumes that the (still unknown) ground-state electron density may be related to an unknown single-particle Hamiltonian. This is not an explicitly verified fact. However, Eq. (4) is generally used in DFT, since the consideration of single-particle wavefunctions simplifies the formalism. Moreover, approximations must be employed for the functionals $E_x[n(\vec{r})]$ and $E_c[n(\vec{r})]$ so that the ansatz (4) is not the only uncertainty. On the other hand, a proper choice of these functionals may compensate the error made using Eq. (4).

The clear relation between $n(\vec{r})$ and $\psi_i(\vec{r})$ enables to perform the minimization of $E[n(\vec{r})]$ with respect to $\psi_i(\vec{r})$

$$\delta_{\psi_i^*}\left[\int E[n(r)]-\sum_{i=1}^{N}\varepsilon_i\left(\int|\psi_i(\vec{r})|^2\,d^3r-1\right)\right]=0 \tag{6}$$

which leads to the Kohn-Sham (KS) equations

$$\left[-\frac{\hbar^2\nabla^2}{2m}+V_{en}(\vec{r})+e^2\int\frac{n(\vec{r}\,')}{|\vec{r}-\vec{r}\,'|}d^3r'+\frac{\delta E_x[n(\vec{r})]}{\delta n(\vec{r})}+\frac{\delta E_c[n(\vec{r})]}{\delta n(\vec{r})}\right]\psi_i(\vec{r})=\varepsilon_i\,\psi_i(\vec{r}) \tag{7}$$

that corresponds to a single-electron Schrödinger equation for ε_i and ψ_i with an effective potential. Strictly speaking, ε_i and ψ_i are auxiliary quantities to be used to determine the electronic density $n(\vec{r})$. On the other hand, in practice these quantities are employed to determine certain ground-state properties as momentum distribution of electrons etc.

The Kohn-Sham equations are solved iteratively: At first an initial or trial electron density is defined. Then, the single-electron wavefunctions ψ_i are determined by solving the Kohn–Sham equations using the initial electron density or that from the preceding iteration step. Afterwards, a new electron density is calculated by Eq. (8) using the solutions ψ_i of the Kohn–Sham equations. If the new electron density is nearly equal to that determined in a preceding iteration step, it can be used to compute the total energy E. Otherwise a further iteration must be performed. In the present work the Vienna Ab-initio Simulation Package (VASP) *[61]* is used to treat the KS equations. This program uses pseudopotential in order to describe the contribution of the core electrons of atoms in the lattice. That means that the effective potential in the KS equations is modified accordingly, and then $\psi_i(\vec{r})$ are the corresponding single-particle wavefunctions of the valence electrons. In VASP plane-wave-type functions are used for $\psi_i(\vec{r})$.

$$\psi_{\vec{k}}(\vec{r})=e^{i\vec{k}\vec{r}}u_{\vec{k}}(\vec{r})=e^{i\vec{k}\vec{r}}\sum_{\vec{G}}c_{\vec{k},\vec{G}}e^{i\vec{G}\vec{r}}=\sum_{\vec{G}}c_{\vec{k},\vec{G}}e^{i(\vec{k}+\vec{G})\vec{r}} \tag{8}$$

where $\vec{k}$ is the wave vector, and $\vec{G}$ is a reciprocal lattice vector. The function $\psi_{\vec{k}}(\vec{r})$ is chosen in such manner that the Bloch theorem (for periodic lattice structures) is valid

$$\psi_{\vec{k}}(\vec{r}+\vec{R})=e^{i\vec{k}\vec{R}}\psi_{\vec{k}}(\vec{r}) \tag{9}$$

with $\vec{R}$ as a lattice vector in the real space. Note that in the single-particle wave function the state is not only characterized by $\vec{k}$ but also by the spin variable which is not shown here explicitly

2.2 Pseudopotentials

Solving Eq. (7) involves all electrons in the system, which makes computational task tedious. The chemical bonding and other physical characteristics of materials depend on the valence electrons and not on core electrons. Therefore it can be a great advantage to describe core electrons approximately, which strongly reduces the number of plane waves necessary in a calculation. This is done using pseudopotentials (PP), where the density of core electrons is replaced by a smoothed density chosen to match various important physical and mathematical properties of the real core electrons. Hence, the PP concept is based on the idea of freezing core electrons and considering only the valence electrons are active. This is called as frozen core approximation. Each PP defines a maximum energy that should be used in calculations, called as cutoff energy (see following section). PPs that require higher and lower cutoff energy are called hard and soft pseudopotential, respectively. Vanderbilt *[62]* developed so-called ultrasoft pseudopotentials (USPPs) with rather low cutoff energies. However, the construction of USPPs requires a number of empirical parameters to be specified. An improved approach within frozen core concept that avoids some of the disadvantages of USPPs was developed by Blöchl *[63]* and is called projector augmented-wave (PAW) method. PAW PPs were later adopted for plane-wave calculations by Kresse and Joubert *[64].* They did extensive comparison of USPPs, and PAW PPs calculations for molecules and extended solids. Their results show that both USPPs and PAW PPs produce essentially identical results in many case. For magnetic materials and materials with atoms that have large differences in electronegativity, the PAW PPs give more reliable results than USPPs *[64]*. Detailed descriptions of these PPs are available elsewhere *[65, 66]*. Based on above facts we selected PAW PPs for all our work, which deals with atomic clusters in ferromagnetic bcc Fe with cluster atoms of very different electronegativity.

2.3 Exchange and Correlation Functionals

Correct expressions for

$$\frac{\delta E_{xc}[n(\vec{r})]}{\delta n(\vec{r})}=\frac{\delta E_{x}[n(\vec{r})]}{\delta n(\vec{r})}+\frac{\delta E_{c}[n(\vec{r})]}{\delta n(\vec{r})} \tag{10}$$

are not available. Therefore, approximations must be used. They are mainly based on results for the homogeneous electron gas with a positively charged homogenous background introduced for reason of charge compensation. This model system is also called jellium. That means that the functional dependence of $\delta E_{xc} / \delta n$ on the (constant) electron density of the jellium is also used for the nonhomogeneous case treated in DFT. Within so-called Local Density Approximation (LDA) *[67, 68]* $\delta E_{xc} / \delta n$ is only a function of the electron density at position $\vec{r}$

$$\frac{\delta E_{xc}[n(\vec{r})]}{\delta n(\vec{r})}=V_{xc}^{LDA}(n(\vec{r})) \tag{11}$$

The next level of approximation is to include the local gradient of the electron density in addition to the local density. This is called *Generalized Gradient Approximation (GGA) [65, 66, 69, 70].*

$$\frac{\delta E_{xc}[n(\vec{r})]}{\delta n(\vec{r})}=V_{xc}^{GGA}\left[n(\vec{r}),\nabla n(\vec{r})\right] \tag{12}$$

Commonly used functionals are the *Perdew–Wang functional (PW91) [71, 72]* and the *Perdew–Burke–Ernzerhof functional (PBE) [73]*. Since in real systems the electron density may not be homogenous, the inclusion of electron density variations by GGA may result in a more reliable theoretical treatment.

Other forms of the exchange-correlation functional are meta-GGA and Hyper-GGA functionals. Meta-GGA includes second derivative of electron density $\nabla^2 n(\vec{r})$ and in Hyper-

GGA a combination of different functional are used. Tao-Perdew-Staroverov-Scuseria (TPSS) functional is an example for meta-GGA and B3LYP functional is typical example for Hyper-GGA. In our work we use the PBE-GGA functional.

2.4 Parameters setting in this work

2.4.1 Plane wave cutoff energy

In practice the sum in Eq. (8) can be only considered up to a fixed energy cutoff E_{cut} and all expansion coefficients $c_{\vec{k},\vec{G}}$ related to a plane wave with a kinetic energy $\frac{\hbar^2(\vec{k}+\vec{G})^2}{2m} > E_{cut}$ are neglected. In general the contribution from higher Fourier components or large $\left|\vec{k}+\vec{G}\right|$ is small. In this work E_{cut} was set to 500 eV. Fig. 2.1 shows that this is a proper value for bcc Fe which is the host material for the atomic cluster investigate in this work. In the calculations of the data shown in Fig. 2.1 the iterative solution of the KS equations is terminated when the difference between the total energy values of two successive iteration steps fell below 10^{-6} eV. The calculation was performed for a bcc Fe unit cell containing two Fe atoms and an optimum k-point grid (see below) was used.

2.4.2 k-point sampling

DFT calculations are often performed considering supercells that contain a certain part of the solid of interest, and in many cases periodic boundary conditions are applied. In this manner, the translational invariance of the considered materials is exploited. The supercell can be also represented in the reciprocal space as the (first) Brillouin zone. On the other hand, electron density and other quantities are represented by integrals over the Brillouin zone, e.g.

$$n(\vec{r}) = \sum_{i}^{occ} \int_{BZ} \left|\psi_{i,\vec{k}}(\vec{r})\right|^2 d^3k \tag{13}$$

Using crystal symmetry the size of the BZ can be still reduced to the so-called *Irreducible Brillouin Zone (IBZ) [65, 66]*. Nowadays simulation packages employ special algorithms to generate a k-point grid for the IBZ. The Monkhorst-Pack method *[74]* is a widely adapted

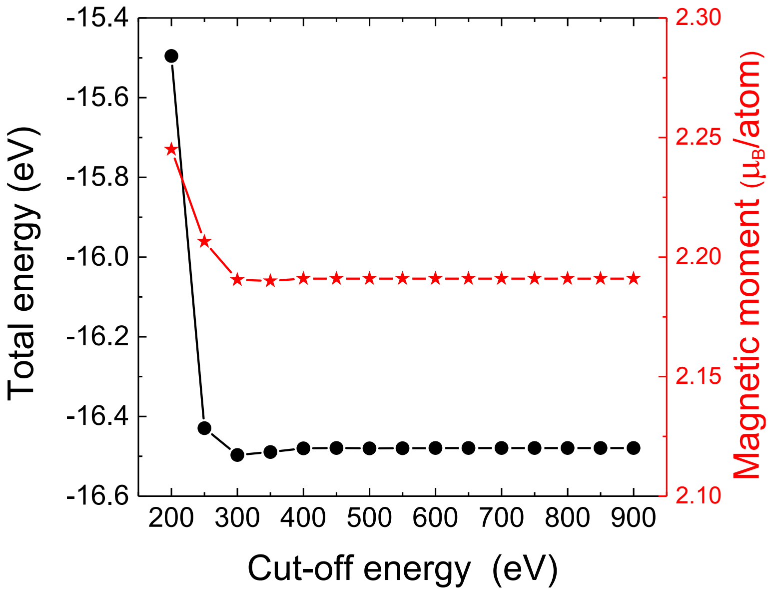

Fig. 2.1: Total energy of a bcc Fe unit cell and the magnetic moment per atom for different values of the plane wave cut-off energy.

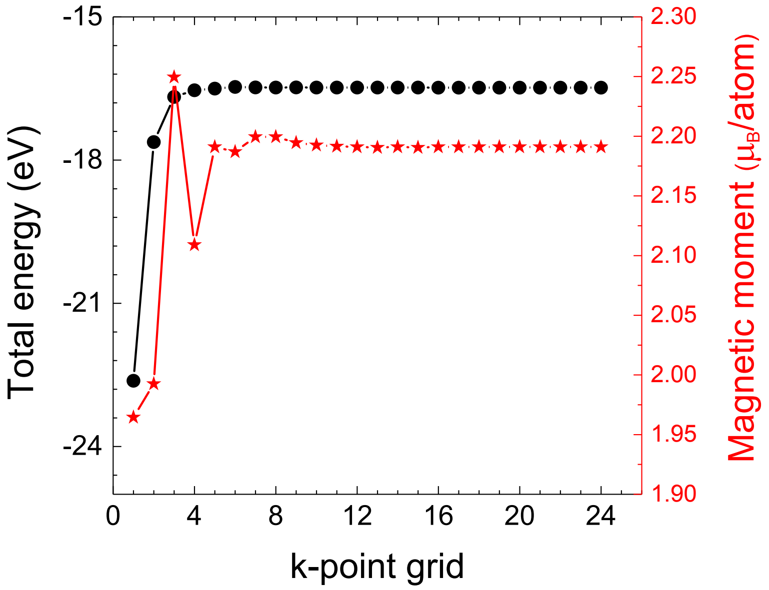

Fig. 2.2: Total energy of a bcc Fe unit cell and the magnetic moment per atom for integration over the IBZ using different k-point grids.

scheme used for integration over the IBZ and is also employed in this work. Likewise energy cutoff, the k-point grid should be optimized with respect to most relevant physical properties. Fig. 2.2 shows the convergence of total energy of bcc Fe unit cell and of the magnetic moment per atom with respect to the number of k-points. The Brillouin zone integration introduces complex problems when the system in metallic due to the partial filling of the band. This problem can be resolved by considering a very fine k-point grid, which ultimately requires lot of computational resource. A more sophisticated approximation to the occupation function can be done using Methfessel and Paxton method [75]. This method utilizes Hermite polynomials to replace the step-like occupation function.

The data depicted in Fig. 2.2 were obtained in the following manner. First an initial guess for a k-point grid is used and the energy cutoff is varied until convergence (precision of total energy: 10^{-6} eV). This procedure is repeated for finer k-point grids. Finally, convergence with respect to energy cutoff as well as k-point sampling is found. Figs. 2.1 and 2.2 demonstrate that a 9x9x9 k-point grid as well as the cutoff of 500 eV are enough to get optimum values of total energy and magnetic moment.

In the present work supercells consisting of several bcc Fe unit cells are considered in order to study the embedded clusters containing O, Y, and Ti atoms as well as vacancies. A larger cell in real space corresponds to a smaller BZ in the reciprocal space. Therefore, in this case a smaller number of k-points can be used in the integration over the IBZ. In this work a 3x3x3 k-point grid is used in calculations with supercells consisting of 4x4x4 unit cells, whereas a 3x3x3 or a 2x2x2 grid is employed for a supercell with 5x5x5 unit cells. In all these cases an energy cutoff of 500 eV is used.

2.5 Calculation of the migration energy or barrier

Atoms or defects can diffuse from one (meta) stable site to another (meta) stable site of the crystal lattice provided enough energy is supplied via temperature. On the diffusion path the atom or defect must overcome an energy barrier (see Fig. 2.3). The Nudged Elastic Band (NEB) method [76, 77] employed in the present work is one of the most precise procedures to determine the migration energy barrier. In the NEB procedure the minimum-energy states before and after a diffusive jump are connected by a number of images. Each image corresponds to a certain state of the whole supercell. The $3N$ dimensional vectors $\mathbf{R}_i$ and $\mathbf{F}_i$ characterize the positions of and the forces on N atoms of image i. For these images a restricted relaxation of both the electronic states and the atomic positions is performed using the DFT calculation procedure. The NEB force on image i is given by

$$\mathbf{F}_i^{NEB} = \mathbf{F}_i^{\perp} + \mathbf{F}_i^{sp} = \mathbf{F}_i^{\perp} + K\left(\left|\mathbf{R}_{i+1} - \mathbf{R}_i\right| - \left|\mathbf{R}_i - \mathbf{R}_{i-1}\right|\right)\boldsymbol{\tau}_i \qquad (14)$$

where $\boldsymbol{\tau}_i$ is the normalized local tangent at image i which may be determined using the

$$\boldsymbol{\tau}_i = \frac{\mathbf{R}_{i+1} - \mathbf{R}_{i-1}}{\left|\mathbf{R}_{i+1} - \mathbf{R}_{i-1}\right|} \qquad (15)$$

and

$$\mathbf{F}_i^{\perp} = \mathbf{F}_i - (\mathbf{F}_i \boldsymbol{\tau}_i)\boldsymbol{\tau}_i \qquad (16)$$

is the perpendicular part of the true force $\mathbf{F}_i$ on image i, and K is the spring constant. In Eq. (14) the spring force allows the band to maintain a spread distribution of images, while the perpendicular part of the true force pushes the band towards the minimum energy path (MEP). The real MEP with the migration barrier is obtained if the NEB force approaches zero, i.e. if the NEB force on all atoms in the supercells of the different images becomes lower than a given threshold. Therefore, NEB calculations consist of a number of iteration steps.

The standard NEB method does not guarantee that one of the images is located exactly at the saddle point or maximum of the MEP, which corresponds to the migration barrier. This value can be determined accurately using the climbing-image NEB *[78]* using the configurations of the images obtained by the standard NEB. In this algorithm the image with the highest energy is identified, and the total force acting on this image is no longer defined by Eq. (14), but is replaced by a modified total true force, where the component along the tangent is reversed:

$$\mathbf{F}_{i,\max}^{NEB} = \mathbf{F}_{i,\max} \mathbf{-2F}_{i,\max} \boldsymbol{\tau}_{i,\max} \qquad (17)$$

The negative parallel component of the true force pushes the image upwards towards the saddle point or maximum, whereas the perpendicular component prevents the image to climb sideways.

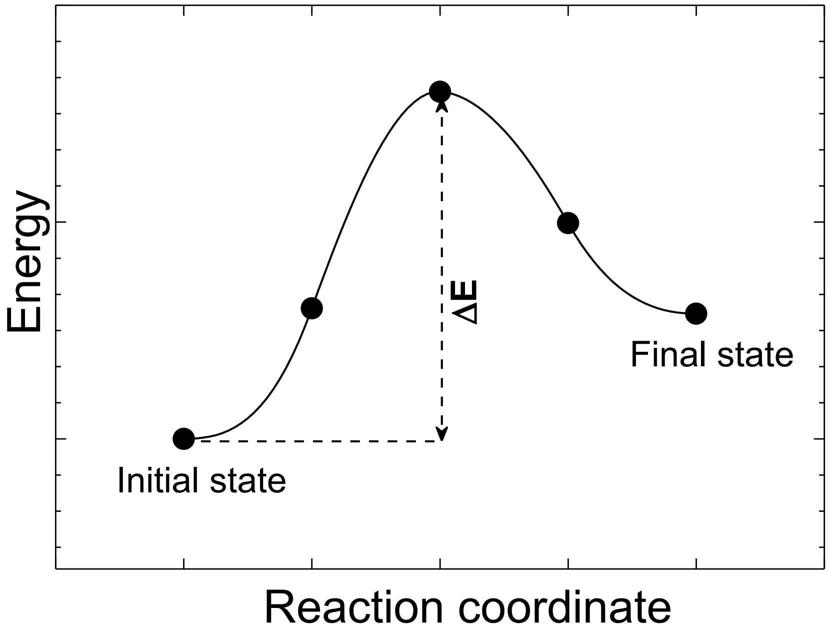

Fig. 2.3: Scheme of a diffusive jump

The accuracy of NEB calculations depends on the number of images considered. More evenly spaced images give more accuracy. But this leads to long computing times. In this work we always use three images. Test calculations with more images clearly show that this choice is sufficient.

X ------------------------------ X

3. Investigation of structural models for O-Y and O-Y-Ti clusters in bcc Fe

---

3.1 Introduction

The technique of ODS production is given in chapter 1. Due to the complexity of the procedure employed in the formation of NFA and the different production routes that may be used, the various experimental ex-situ methods analyze a certain state at the end of the thermal processing. It cannot be expected that this state correspond to a full thermodynamic equilibrium. Therefore, the clusters observed should be related to different stages of their evolution. Indeed, structural and compositional analyses reported different results. This is also caused by the different analysis methods applied. There exists a plethora of papers concerning the nature of the O-Y-Ti or O-Y nanoclusters. In a recent review paper the properties of the most relevant clusters with a size below about 5 nm were discussed *[21]*. It was stated that several distinct atomic configurations were proposed by the different authors, in particular nonstoichiometric crystalline or amorphous structures, which may contain vacancies and Fe atoms (cf. e.g. also *[29]*), a rock salt structure, as well as near stoichiometric Y_2O_3, or $Y_2Ti_2O_7$ and Y_2TiO_5 oxides. In the review paper it was concluded that the near-stoichiometric oxide structures should be most probable, with different orientation relationships with regard to the bcc host crystal *[21]*.

Besides experimental investigations with advanced analytical methods atomic-scale theoretical studies and computer simulations can significantly contribute to improve the knowledge on structure and properties of the nanoclusters in NFA. Finding a thermodynamically or energetically favored structure of a small cluster (or precipitate) of foreign atoms in a given host matrix is a very general task to be solved in various fields of computational materials science. In this chapter, detailed search for most stable ground state configurations of small O-Y and O-Y-Ti clusters in bcc Fe is focused. Due to the requirements for computational resources in DFT calculations, the cluster size does not exceed 1 nm. These clusters may be considered as nuclei for further structural evolution and growth. At elevated temperature vibrational, configurational, and other contributions to the free energy (cf. [79, 80] and references therein) may influence the thermodynamic stability of the clusters. Consideration of these effects are out of scope of this chapter.

This chapter is organized as follows. At first the distinct structural models for the O-Y and O-Y-Ti clusters are introduced. The following section explains the DFT method which is employed in relaxation calculations in order to determine the most stable state of the particular cluster. In the main part results on structure and energetics of the relaxed configurations are presented and discussed in detail. In particular the data obtained for different models are compared and conclusions are drawn from present findings. Finally, the results are shortly summarized.

3.2 Structural models for O-Y and O-Y-Ti clusters

Different basic assumptions may be used in modeling of O-Y and O-Y-Ti clusters in bcc Fe. On the one hand, one may look for a matching between structures of known oxides with the bcc host lattice. In this work this is done by inserting a part of the Y_2O_3 bixbyite structure or a part of the $Y_2Ti_2TiO_7$ pyrochlore structure into bcc Fe (Structure Matching model – SM). Due to the limitation of the size of the supercell in DFT calculations, the maximum extension of the oxide cluster is less than one eighth of the bixbyite and pyrochlore unit cells. Figs. 3.1 and 3.2 depict the incorporation of these octahedron-like clusters into bcc Fe. The {100} planes of the oxides match with that of bcc Fe, and the maximum dimensions of the clusters along the <100> directions are rather similar to four times the lattice constant of iron. The details of the incorporation are illustrated in the Appendix-A [App-A]. The SM model studied in this work corresponds to that used by Barnard et al. [35] On the other hand, cluster structures may be also built considering the most stable point defect configurations in bcc Fe, i.e. O on octahedral interstitial sites as well as Y and Ti on substitutional sites and vacancies on bcc sites (Point Defect model-PD) [37, 38, 42, 81]. Using the PD model atomic structures similar to those shown in Figs. 3.1 (a) and 3.2 (a) were constructed. Fig. 3.1 (c) shows the PD model in the case where O and Y atoms as well as vacancies belong to the cluster. If the cluster consists of O, Y, and Ti atoms and vacancies two configurations PD-1 and PD-2 are possible [Figs. 3.2 (c) and 3.2 (e)]. A proper comparison between the atomic configurations and the energetics is only possible if the same number of Fe, O, Y, and Ti atoms is used in the different structural models. In the SM model shown in Fig. 3.1 (a) [3.2 (a)] the composition of the supercell consists of 6 O, 6 Y [3 Y, 3 Ti] and 113 Fe atoms. In this work all bcc sites not occupied by metal atoms (Fe, Y, Ti) are counted as vacancies (v). That means that all O atoms are assigned to vacancies. The reason for such a definition becomes clear by considering the corresponding clusters in the PD model [Figs. 3.1 (c), 3.2 (c), and 3.2 (e)]. Here each O atom on an octahedral interstitial site is related to a nearby vacancy. Furthermore, there are still three additional vacant sites and the supercell consists of the same number of Fe, O, Y (or Y and Ti) atoms as in the case of the SM and AS (see below) models. In the following the clusters depicted in the figures are denoted by 6O9v6Y (Fig. 3.1) and 7O9v3Y3Ti (Fig. 3.2). It should be noticed that compared to pure Y_2O_3 and pure $Y_2Ti_2TiO_7$ these clusters are depleted in oxygen. As illustrated above the SM and PD models may be considered as certain limiting cases. Other models are also possible, e.g. Y, Ti, but also O, can be placed on Fe sites [All Substitutional model – AS, Figs. 3.1 (e) and 3.2 (g)] using a cluster geometry similar to that shown in Figs. 3.1 (a) and 3.2 (a).

SM, PD, and AS are cage-like models since there is a vacant bcc site in the center of the cluster. Alternative models may be built by placing an atom in the cage. For a comparison with the original SM, PD, and AS models the composition of the clusters must be kept. This may be achieved by shifting one oxygen, Y, or Ti atom of the original SM, PD, or AS cluster model to the center site. In this work alternative models built by the shift of an O atom are studied. Several distinct choices for shifting an O atom towards the center of 6O9v6Y must be considered: (i) SM: 2 choices (SM-OC1 and SM-OC2 models), (ii) AS: 2 choices (AS-OC1 and 2). The O atom to be shifted in the models SM-OC1, SM-OC2, etc. are marked in Figs. 3.1 (a) and 3.1 (e). To be consistent with the point defect picture, within the framework of the PD model one oxygen atom is shifted to an octahedral interstitial site close to the vacancy in the center. For 6O9v6Y there exist 8 choices for such shifts, cf. arrows and numbers in Fig. 3.1 (c). Still more choices for shifts of an O atom towards the center vacant site are possible in the case of the 7O9v3Y3Ti clusters. Here only the SM and AS models are considered and the choices are the following: (i) 7 choices SM-OC1-7, and (ii) 7 choices AS-OC1-7, cf. arrows and numbers in Figs. 3.2 (a) and 3.2 (g).

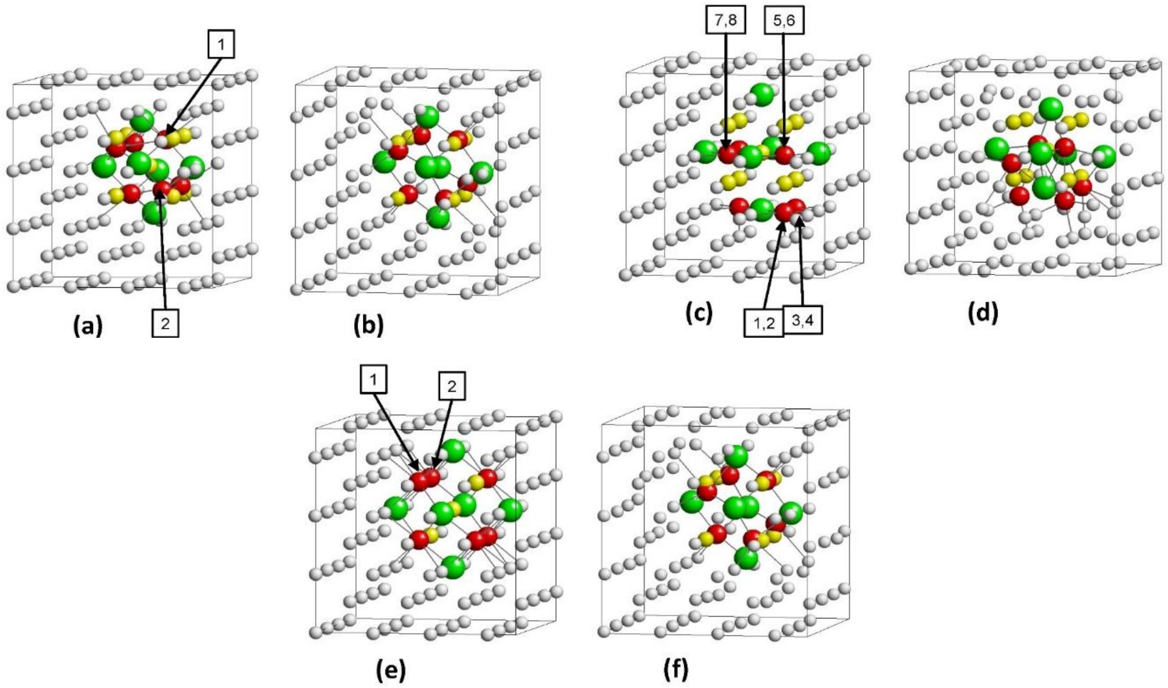

Fig. 3.1: Structure Matching (SM) (a,b), Point Defect (PD) (c.d), and All Substitutional (AS) (e,f) models for 6O9v6Y clusters. The left (a,c,e) and right (b,d,f) figures depict the supercell with the cluster before and after relaxation by DFT calculations, respectively. Red, green, gray, and yellow spheres show O, Y, Fe atoms, and vacancies, respectively. The numbers denote the O atoms which are shifted to the center in order to form the OC clusters (see Fig. 3.4)

For the supercells with the same composition but structures according to the different models DFT calculations were carried out in order to find the relaxed atomic configurations corresponding to a minimum energy state. The specific cluster compositions 6O9v6Y and 7O9v3Y3Ti were chosen to illustrate differences and similarities between the results obtained after relaxation calculations within the framework of the given structure model. Another motivation for this choice is the comparison with the results of Barnard et al. [35] who investigated SM clusters with these compositions. Using the structures of the 6O9v6Y or

7O9v3Y3Ti in the SM, PD, and AS models as templates, many characteristic clusters of smaller size were also investigated in this manner. Details on the construction of these clusters are illustrated in the Appendix-A *[App-A]*.

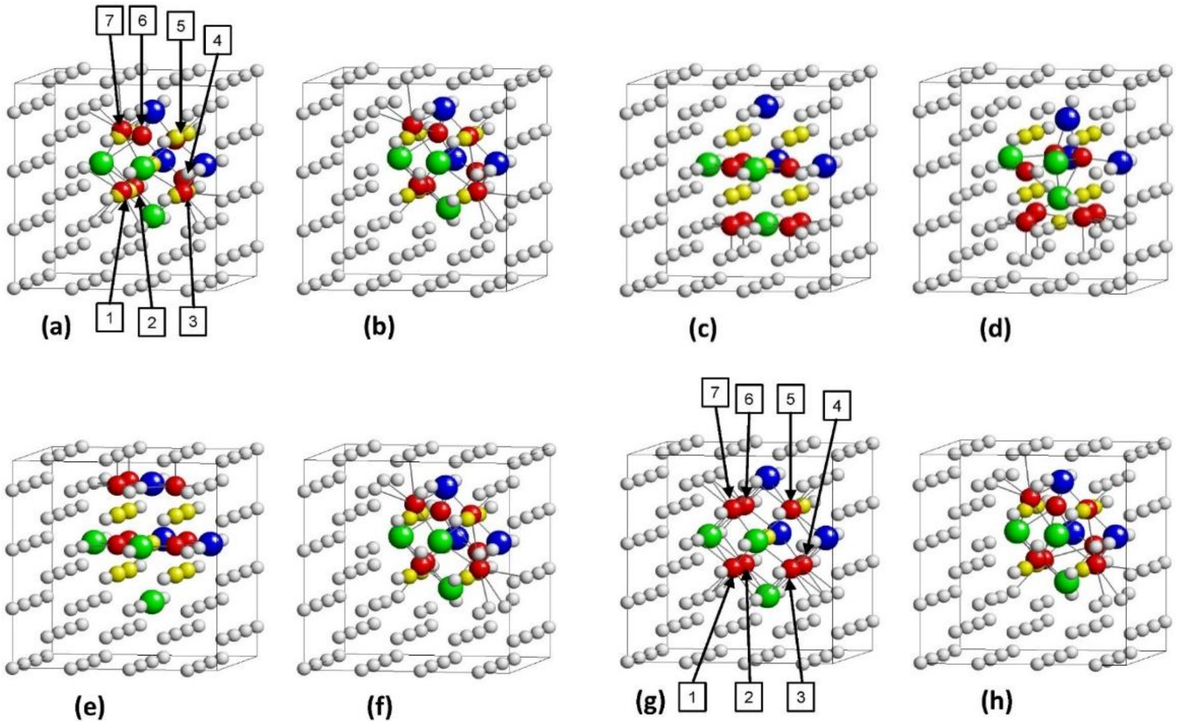

Fig. 3.2: Structure Matching (SM) (a,b), Point Defect (PD) (c-f), and All Substitutional (AS) (g,h) models for 7O9v3Y3Ti clusters. The left (a,c,e,g) and right (b,d,f,h) figures show the supercell with the cluster before and after relaxation by DFT calculations, respectively. Blue spheres are Ti atoms, the meaning of the other colors and of the numbers is explained in the caption of Fig. 3.1.

3.3 Calculation procedure

DFT calculations were performed using the Vienna ab-initio simulation package VASP *[61, 64, 82]*. Projected- Augmented-Wave(PAW) *[63, 83]* type pseudopotentials with the Perdew-Burke-Ernzerhof (PBE) *[73]* parameterization for treatment of exchange and correlation effects were applied to mimic positive cores and valence electrons. The spin polarized formalism and a plane wave cutoff of 500 eV were used. A uniform Monkhorst-Pack scheme *[74]* centered at the gamma point was considered for Brillouin zone integration. Most calculations were carried out for cubic bcc-Fe supercells with 128 bcc lattice sites (4x4x4 bcc unit cells) and a mesh with 3x3x3 k points. In order to check the influence of the supercell size on the results, in selected cases a supercell with 250 lattice sites (5x5x5 bcc unit cells) and 3x3x3 k points was considered. For the integration in the k-space the Methfessel-Paxton smearing method [75] was applied with a width of 0.2 eV. After construction of a cluster according to one of the structural models described above the positions of atoms as well as the volume and shape of the supercell were relaxed so that the total stress/pressure on the supercell became zero. The accuracy of such kind of relaxation calculations is determined by: (i) the residual force acting on any atom at a given atomic relaxation step. (ii) The change of the total energy between steps of energy minimization of the electronic system within each atomic relaxation step. In the present work calculations were performed until the residual force and the energy change fall below 10^{-2} eV/Å and 10^{-5} eV, respectively.

3.4 Binding energy calculation

The total binding energy of a cluster consisting of n different monomers, i.e. O, Y, Ti atoms and vacancies, is defined by

$$E_{bind} = E(X_1 + X_2 + ... + X_n) + (n-1)E^0 - \sum_{i=1}^{n} E(X_i) \tag{18}$$

$E(X_1 + X_2 + ... + X_n)$ and $E(X_i)$ denote the total energy of supercells with the cluster $X_1 + X_2 + ... + X_n$ and the monomers X_i, respectively, while E^0 is the total energy of a supercell containing perfect bcc Fe. By definition the value of E_{bind} is negative if attraction between the atomic species dominates. The data for $E(X_i)$ are determined assuming O on octahedral interstitial sites, and Y, Ti as well as the vacancy on bcc lattice sites. As already mentioned in the previous section, all bcc sites not occupied by metal atoms (Fe, Y, Ti) are counted as vacancies. At this point it is worth mentioning that the so-called cluster formation energy $E_f^{Barnard}$ defined by Barnard et al. [35] can be easily obtained from E_{bind}

$$E_f^{Barnard} = E_{bind} + n_{\mathrm{v}} E_f^{\mathrm{v}} \tag{19}$$

where n_v and E_f^v are the number of vacancies in the cluster and the vacancy formation energy, respectively. The latter quantity is defined by

$$E_f^\mathrm{v} = E(\mathrm{v}) - \frac{N-1}{N} E^0 \tag{20}$$

with N as the total number of atoms in the related supercell with perfect bcc Fe. In this work the value of 2.169 eV was used for E_f^v. This is in agreement with data in previous publications cf., e.g., *[39]* and references therein. It must be noted that the quantity $E_f^{Barnard}$ can be also considered as a kind of total binding energy of the cluster because it can be transformed to E_{bind} by Eq. (19). As already mentioned in section 3.2, the number of Fe, O, Y, and Ti atoms as well as vacancies is the same in the SM, PD and AS models considered in the comparative studies of this work. Due to these facts, results which are presented in terms of E_{bind} could be also presented in terms of $E_f^{Barnard}$, and the respective conclusions would be equivalent.

3.5 Results for SM, PD, and AS cluster models

The relaxation of the SM configuration leads to modifications of the positions of O, Y, and Ti atoms and of the related bond lengths [Figs. 3.1 (b) and 3.2 (b)]. The O atoms are rearranged in the environment of the nearby vacant bcc lattice sites. In the case of 7O9v3Y3Ti the smallest position change is found for Ti while Y atoms move slightly towards the center of the cluster. The latter is also observed for the 6O9v6Y cluster. A considerable change of atomic positions and bond lengths is observed after relaxation of the PD configurations. In Figs. 3.1 (d) and 3.2 (d) the upper and lower Y (or Y and Ti) atoms are shifted towards the center of the cluster. In the case of 6O9v6Y the lower and some upper oxygen atoms move towards the lower vacant sites. In Fig. 3.2 (d) this effect is somewhat smaller. On the other hand the relaxation of the structure shown in Fig. 3.2 (e) leads to an atomic configuration which is similar to that shown in Fig. 3.2 (b) and (h) for the SM and AS cases [cf. Fig. 3.2 (f)]. Modifications of the atomic positions are also found after relaxation of the AS structures. As in the SM case, Ti atoms change their positions only slightly while Y is shifted into direction of the center of the cluster and O atoms leave the substitutional sites. For 6O9v6Y and 7O9v3Y3Ti clusters the total binding energies of the relaxed SM and AS configurations are nearly identical (Table 3.1). This is remarkable since the initial states are rather different. It may be assumed that in the case of 7O9v3Y3Ti this equality is caused by the fact that the positions of the Ti atoms are more or less fixed during relaxation. For 6O9v6Y the volume increase ΔV of the supercell due to the presence of the relaxed cluster as well as the cell dimensions are somewhat different for SM and AS, whereas these quantities are more or less equal in the case of 7O9v3Y3Ti. In order to understand the difference of the ΔV values of 6O9v6Y-SM and 6O9v6Y-AS (cf. Table 3.1), additional calculations were performed with a higher precision (force criterion: 10^{-4} eV/Å, energy criterion: 10^{-7} eV). The results show nearly equal values of 60.415 and 60.420 Å^3. Therefore, the relaxed 6O9v6Y-SM and 6O9v6Y-AS clusters are indeed nearly identical as it was already found for the relaxed 7O9v3Y3Ti-SM and 7O9v3Y3T-AS configurations. The relaxed 6O9v6Y PD structure is only slightly less stable than those obtained from the SM and AS models, i.e. the absolute value of E_{bind} is only lower by about 2% (Table 3.1). On the other hand, the total binding energy of the relaxed 7O9v3Y3Ti PD-2 configuration [Fig. 3.2 (f)] is similar to that obtained for the SM and AS models, whereas the relaxed PD-1 structure [Fig. 3.2 (d)] is by 6% less stable. The presence of the relaxed PD cluster causes tetragonal (6O9v6Y: PD and 7O9v3Y3Ti: PD-2) and orthorhombic (7O9v3Y3Ti: PD-1) distortions of the supercell. In the SM case the values for the total binding energy show a reasonable agreement with the data of Barnard et al. *[35]* who also used a supercell with 128 bcc sites in their DFT study. The small differences may be due to the fact that in the present work a newer version of VASP pseudopotentials (version 5.4), more k points (3x3x3 instead of 2x2x2), and a higher plane wave cutoff (500 instead of 400 eV) were used.

6O9v6Y and 7O9v3Y3Ti clusters were also studied in a supercell with 250 bcc lattice sites and 3x3x3 k points. The atomic configurations can be found in Appendix-A [*App-A]*. The total binding energy of the relaxed SM and AS 7O9v3Y3Ti configurations is nearly equal and very similar to the results obtained in the case of the smaller supercell (Table 3.1).

Table 3.1: Total binding energy E_{bind} of 6O9v6Y and 7O9v3Y3Ti clusters obtained from the structural models SM, PD, and AS, by considering the relaxed configurations and supercells containing 128 and 230 bcc lattice sites. Data from literature *[35]* are also shown. The volume change $\Delta V = V - V_0$ with respect to the supercell with pure bcc Fe and the dimensions of the supercell are also given. In the case of an isotropic expansion/contraction only one supercell dimension is given while for tetragonal distortions the first line is related to the two equivalent directions (a) whereas the second line is related the third direction (b). In the case of an orthorhombic distortion, three lines (a), (b), and (c) are given.

	128 bcc sites			**250 bcc sites**		
	E_{bind} (eV)	**V_0 (Å^3)**	**d (Å)**	**E_{bind} (eV)**	**V_0 (Å^3)**	**d (Å)**
Pure Fe	-	1454.1	11.329	-	2838.3	14.159
			6O9v6Y			
		ΔV_0 (Å^3)			**ΔV_0 (Å^3)**	
SM	-42.76 *-43.90 [35]*	64.407	11.496	-41.97	40.346	14.226 (a) 14.225 (b) 14.223 (c)
PD	-41.90	42.258	11.586 (a) 11.147 (b)	-41.76	54.524	14.282 (a) 14.182 (b)
AS	-42.76	56.896	11.477	-42.31	58.779	14.256
			7O9v3Y3Ti			
SM	-40.34 *-41.70 [35]*	26.373	11.397	-40.12	28.920	14.206
PD-1	-37.74	35.771	11.467 (a) 11.331 (b) 11.467 (c)			
PD-2	-40.40	27.152	11.391 (a) 11.416 (b)	-40.87	21.755	14.189 (a) 14.204 (b)
AS	-40.34	26.398	11.397	-40.18	21.832	14.194

Also the atomic configurations are nearly identical in these four cases and the values for the volume increase are not very different. On the other hand, the relaxed SM and AS 6O9v6Y configurations, as well as the corresponding data for E_{bind} and ΔV differ somewhat more than in the supercell with 128 bcc sites. The relaxed SM structure is also not equal to that in the smaller supercell. On the other hand the values of E_{bind} for the SM and AS clusters in the larger and smaller supercells do not differ by more than 2%. The atomic configuration of the PD 6O9v6Y cluster in the larger supercell agrees with that in the smaller one, and also the total binding energy are nearly equal. The comparison between the results for supercells with 128 and 250 bcc sites shows that a possible size effect depends on the cluster model considered. However, the qualitative conclusions obtained from the consideration of the clusters in the smaller supercell are also valid in the case of the larger one.

Fig. 3.3 summarizes values for the total binding energy per cluster constituent E^{C}_{bind} (E_{bind} divided by the number of atoms and vacancies in the cluster) obtained for a number of smaller clusters in the supercell with 128 bcc sites (cf. [*App-A*]), together with the corresponding data for 6O9v6Y and 7O9v3Y3Ti. The figure demonstrates that in general the relaxed cluster configurations determined for the SM, PD, and AS models have very similar energetics. In some cases the values of E^{C}_{bind} and the atomic configurations are also equal. These results clearly show that the SM configuration is not generally favored as suggested by Barnard et al. *[35]*. It must be noticed that besides the SM case in Ref. *[35]* the so-called On-Lattice Model was investigated. This model considers O on octahedral interstitial sites as well as Y and Ti on substitutional sites. This is quite similar to the PD model in the present work, but the On-Lattice Model does not contain vacancies. Therefore, the number of Fe atoms is higher than in the SM model, i.e. the composition of the supercell is not equal to that in the SM model. Due to these differences Barnard et al. *[35]* obtained relaxed cluster configurations for their On-Lattice Model which are much less stable than those for the SM model. In contrast present

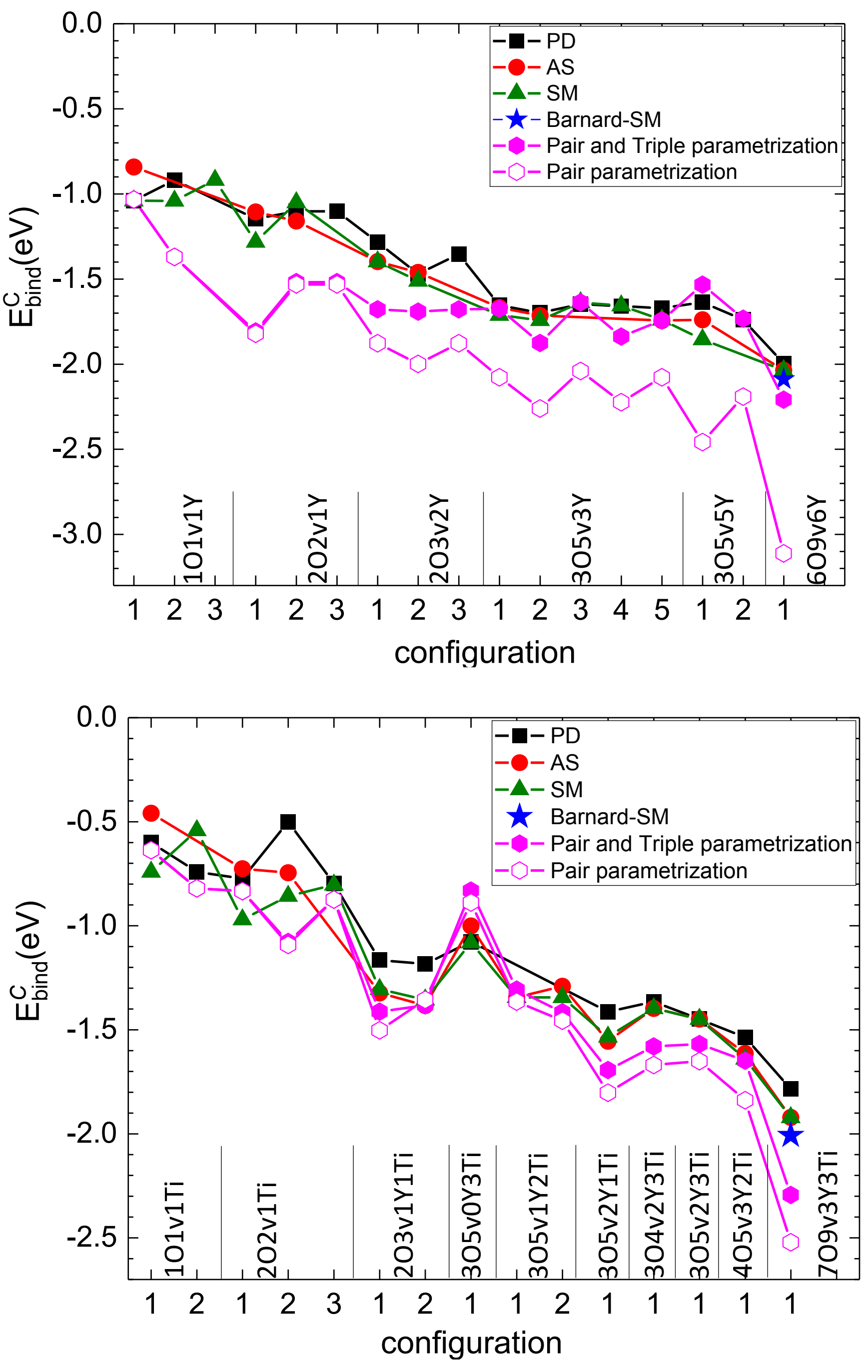

Fig. 3.3: Total binding energy per cluster constituent E^C_{bind} (E_{bind} divided by the number of atoms and vacancies in the cluster) obtained for a number of smaller clusters containing O, Y and vacancies (a) or O, Y, Ti, and vacancies (b), together with the results for 6O9v6Y and 7O9v3Y3Ti. The smaller clusters were constructed using the atomic configurations of 6O9v6Y or 7O9v3Y3Ti in the SM, PD, and AS models as templates (cf. Appendix-A *[App-A]*). Data from literature *[35]* are also given. The lines are only drawn to guide the eye. Results obtained using pair as well as pair and triple parametrization within the rigid lattice model are also shown.

results on the energetics of the PD model show only very small differences to those for the SM model.

In a previous work [40] the energetics of O-Y and O-Y-Ti clusters was investigated using a rigid lattice model (RLM) with O on octahedral sites as well as Y and Ti on bcc sites, and with DFT-based parameters for pair and triple interactions between the constituents of the clusters (O, vacancies, Y, or Ti). The atomic arrangements in the PD model before relaxation (see Figs. 3.1 and 3.2) correspond to those within the RLM. Therefore, these configurations were investigated using pair interaction parameters as well as pair and triple interaction parameters from Ref. [40]. The results are also shown in Fig. 3.3. In general, the description by pair and triple parameters yields a better agreement with present DFT results than using only pair parametrization. For small sizes the agreement is better for clusters that contain Ti.

3.6 Results for SM-OC, PD-OC, and AS-OC cluster models

All configurations obtained after relaxation of the OC-type structures with oxygen in the center can be found in Appendix-A [App-A]. The data for their total binding energy, for the volume change due to the presence of the cluster as well as the dimensions of the supercell are given in Table 3.2. In the case of 6O9v6Y after relaxation the O atom always stays in the center of the cluster. The relaxed SM-OC1 and SM-OC2 configurations and the related data for the total binding energy, volume change and supercell dimensions are very similar. The supercell shows a slight orthorhombic distortion. The results for the relaxed AS-OC1 and AS-OC2 6Y9v6Y structures are nearly identical and a tetragonal distortion is found. For the various PD-OC configurations values between about -44 eV, and -42 eV were found for E_{bind} although the data of E_{bind} vary within a relatively narrow range, the relaxed PD-OC clusters show very different structures. Only PD-OC3 and PD-OC7 are almost identical. Figs. 3.4 (a-d) show exemplary cases of SM-OC, AS-OC, and PD-OC 6O9v6Y clusters. The central oxygen atom has nearly the same distance to the six Y neighbors which is similar to the coordination of the anion in a rock-salt structure. Most remarkable is the fact that the relaxed 6O9v6Y OC-type clusters are always slightly more stable than those obtained by relaxation of the corresponding cage-like SM, PD and AS types (Table 3.1). In particular the absolute value of the total binding energy of a SM-OC / AS-OC / PD-OC cluster is by about 4% / 3% / 3-5% higher than that determined for the original SM / AS / PD cage-like clusters. This result and the findings of the preceding section clearly show that there exists a variety of rather different cluster configurations with a very similar energetics. Comparison between Table 3.2 and Table 3.1 shows that the volume increase due the presence of the cluster is smaller for the SM-OC and AS-OC clusters than for the corresponding cage-like clusters.

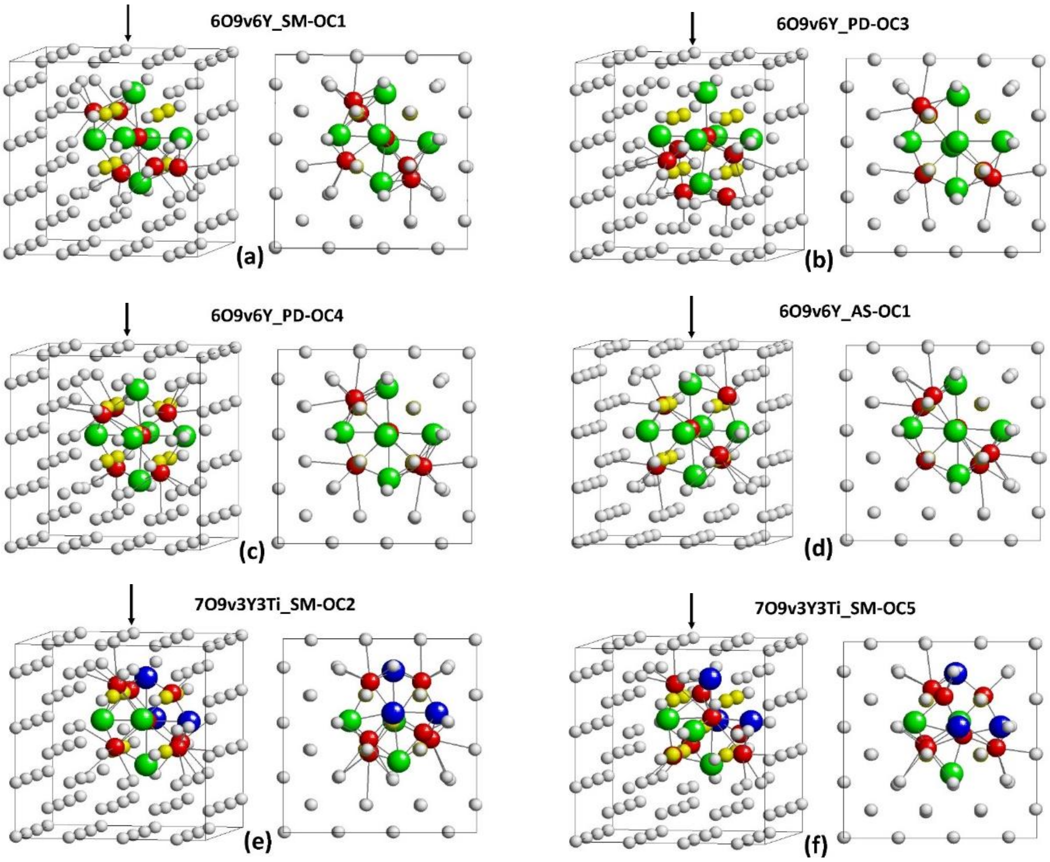

Fig. 3.4: Selected examples of relaxed 6O9v6Y (a-d) and 7O9v3Y3Ti (e, f) clusters with oxygen in the center. If the viewing direction is along the arrow on the left figures, pictures as shown on the right figures appear. The numbering of these SM-OC, PD-OC, and AS-OC configurations is according to Fig.3.1. A compilation of all the OC-type cluster can be found in the Appendix-A *[App-A]*.

Table 3.2: Total binding energy E_{bind} , volume change ΔV and supercell dimensions determined for the relaxed 6O9v6Y and 7O9v3Y3Ti clusters within the framework of the structural models SM-OC, PD-OC, and AS-OC. The meaning of the shown quantities is the same as in Table 3.1.

	E_{bind} (eV)	ΔV (Å^3)	d (Å)
6O9v6Y (128 bcc sites)			
SM-OC1	-44.49	35.527	11.418 (a) 11.427 (b) 11.416 (c)
SM-OC2	-44.49	34.772	11.423 (a) 11.416 (b) 11.417 (c)
PD-OC1	-44.09	42.712	11.414 (a) 11.435 (b) 11.467 (c)
PD-OC2	-44.49	34.949	11.416 (a) 11.419 (b) 11.422 (c)
PD-OC3	-42.23	56.216	11.419 (a) 11.583 (b)
PD-OC4	-43.85	36.430	11.419 (a) 11.429 (b)
PD-OC5	-44.48	39.358	11.432 (a) 11.438 (b) 11.420 (c)
PD-OC6	-44.24	38.188	11.416 (a) 11.407 (b) 11.459 (c)
PD-OC7	-42.23	56.327	11.419 (a) 11.584 (b)
PD-OC8	-44.00	38.002	11.436 (a) 11.407 (b)

	E_{bind} (eV)	**ΔV (Å^3)**	**d (Å)**
AS-OC1	-44.04	38.696	11.434 (a) 11.419 (b)
AS-OC2	-44.04	38.805	11.434 (a) 11.419 (b)
6O9v6Y (250 bcc sites)			
SM-OC1	-44.25	34.129	14.215 (a) 14.214 (b)
SM-OC2	-44.25	34.036	14.215 (a) 14.214 (b)
AS-OC1	-44.04	39.052	14.224 (a) 14.221 (b)
AS-OC2	-44.04	38.079	14.222 (a) 14.220 (b)
7O9v3Y3Ti (128 bcc sites)			
SM-OC1 (stays not in center)	-40.34	26.781	11.398 (a)
SM-OC2	-39.56	18.147	11.366 (a) 11.396 (b)
SM-OC3	-39.55	18.224	11.367 (a) 11.395 (b)
SM-OC4	-40.02	22.630	11.365 (a) 11.432 (b)
SM-OC5	-40.02	22.562	11.431 (a) 11.365 (b) 11.365 (c)
SM-OC6	-40.02	22.603	11.365 (a) 11.365 (b) 11.431 (c)
SM-OC7	-39.56	18.104	11.365 (a) 11.397 (b)
AS-OC1 (stays not in center)	-40.34	26.827	11.398

	E_{bind} (eV)	**ΔV (Å^3)**	**d (Å)**
AS-OC2	-39.56	17.930	11.366 (a) 11.394 (b)
AS-OC3	-39.56	17.714	11.365 (a) 11.394 (b)
AS-OC4	-40.017	22.582	11.365 (a) 11.432 (b)
AS-OC5	-39.96	23.027	11.366 (a) 11.433 (b)
AS-OC6	-40.017	22.681	11.366 (a) 11.431 (b)
AS-OC7	-39.56	17.917	11.365 (a) 11.396 (b)
7O9v3Y3Ti (250 bcc sites)			
SM-OC1 (stays not in center)	-40.81	25.212	14.200

On the other hand, the presence of the different PD-OC clusters leads to values for the volume increase which are higher or lower than that of the PD clusters [cf. also Fig. 3.5 (a)]. For the various PD-OC configurations a correlation between volume change and total binding energy can be found. In Fig. 3.5 (a) the relative increase δE_{bind} of the absolute value of total binding energy as well as the relative increase of the supercell volume δV are depicted. The value of E_{bind} for the cage-like PD configuration was taken as reference to determine δE_{bind}, whereas δV is calculated by dividing the values ΔV from Table 3.2 by the volume of the supercell for pure bcc Fe (cf. Table 3.1). Fig. 3.5 (a) clearly shows that higher values of δE_{bind} are correlated to lower values of δV, i.e. more compact clusters, with an average distance of 2.33 Å between the central O atom and the six Y atoms, are energetically preferred.

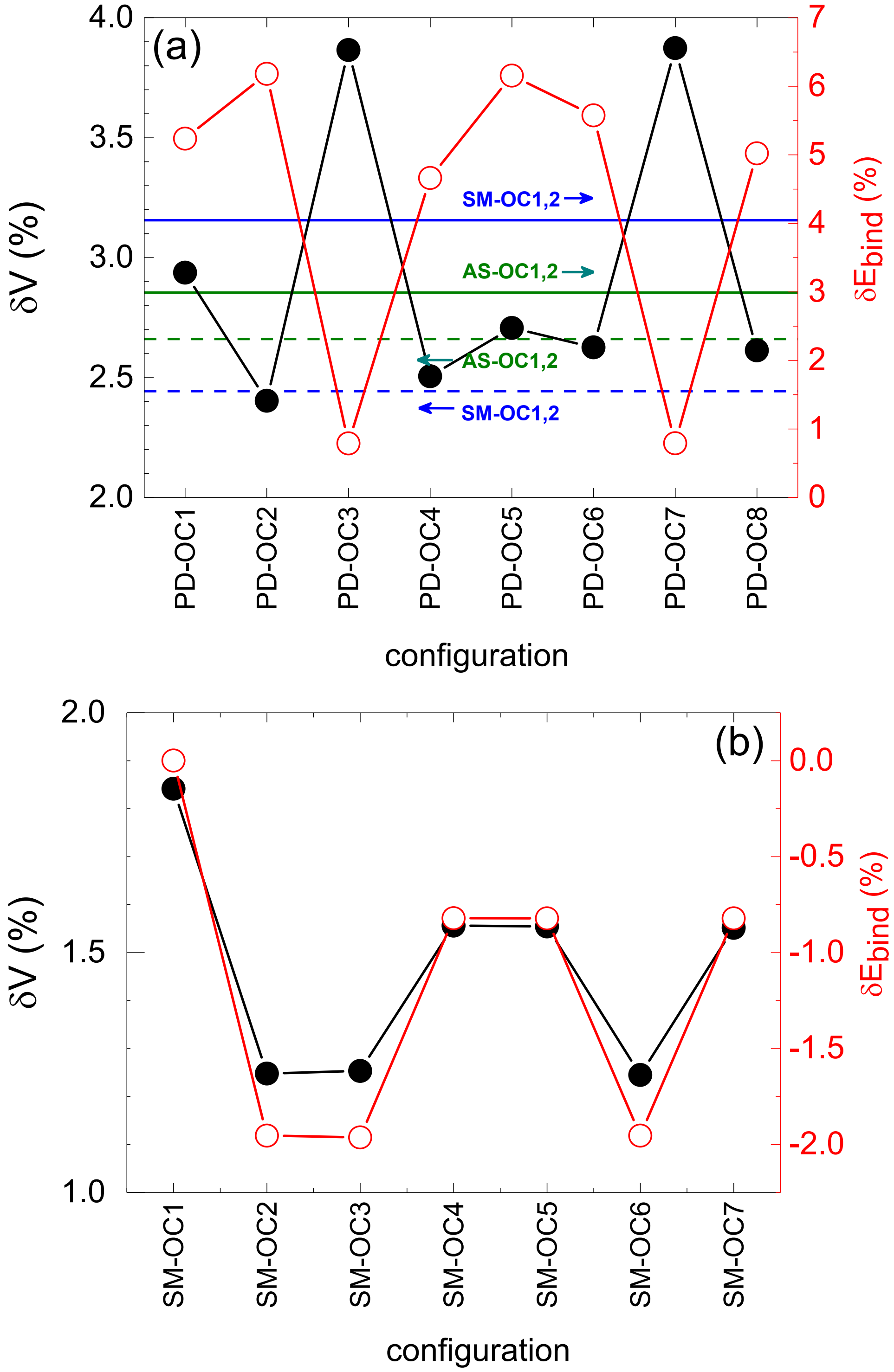

Fig. 3.5: Relative increase of the supercell volume δV (black symbols, left axis) and relative increase δE_{bind} of the *absolute* value of total binding energy (red symbols, right axis) for PD-OC 6O9v6Y clusters (a) and SM-OC 7O9v3Y3Ti clusters (b). The horizontal lines in (a) show results for SM-OC and AS-OC 6O9v6Y clusters.

Some SM-OC and AS-OC 6O9v6Y models were also relaxed in the larger supercell with 250 bcc sites. The corresponding data on energetics, volume increase and supercell dimensions are also given in Table 3.2 while the atomic configurations can be found in the Appendix-A *[App-A]*. In the Table 3.2 the data for SM-OC1 and SM-OC2 as well as for AS-OC1 and AS-OC2 are nearly equal. The values for the clusters in the larger supercell and the related atomic configurations only slightly differ from those obtained for the supercell with 128 bcc sites. However, both the results for SM-OC and AS-OC clusters confirm the findings already discussed for the smaller supercell.

Also in the case of 7O9v3Y3Ti clusters oxygen stays mostly in or near the center during relaxation. Exceptions are the SM-OC1 and AS-OC1 configurations where the cage-like structures SM and AS are found after relaxation [cf. Figs. 3.2 (b) and 3.2 (h)]. Here the configurations before relaxation were constructed in such a manner that an oxygen atom from the environment of three Y atoms was set into the center [cf. Figs. 3.2(a) and 3.2 (g)]. Obviously the binding to these Y atoms is very strong so that relaxation moves the oxygen back to their vicinity. In the other cases the O atom that is set into the center is from an environment consisting of Y and Ti atoms. For the SM-OC and AS-OC 7O9v3Y3Ti clusters the data for E_{bind} etc. are given in Table 3.2. The atomic configurations of the particular AS-OC structures are almost equal to those of the corresponding SM-OC case. This should be mainly caused by the fact that the positions of the Ti atoms are more or less fixed during the relaxation, as already found in the case of the cage-like clusters. Examples of atomic structures of relaxed clusters are depicted in Figs. 3.4 (e) and 3.4 (f). Interestingly, the relaxed 7O9v3Y3Ti SM-OC and AS-OC clusters with oxygen in or near the center are by about 0.8 to 2% less stable than those of the relaxed cage-like SM and AS configurations. This is in contrast to the results for the OC-type 6O9v6Y clusters. The presence of OC-type 7O9v3Y3Ti clusters leads to a smaller volume increase (Table 3.2) than that obtained for the SM and AS clusters (Table 3.1). Fig. 3.5 (b) depicts the relation between δE_{bind} and δV for the SM-OC configurations. The results for AS-OC are almost equal because the atomic configurations are nearly identical, cf. discussion above. Unlike the 6O9v6Y clusters the increase/decrease of δE_{bind} is correlated with the increase/decrease of δV. As already mentioned above the relaxed SM-OC1 cluster is identical to the cage-like cluster which is taken as reference. Therefore the corresponding value of δE_{bind} is zero. Fig. 3.6 shows the comparison of the present DFT results with those obtained using the rigid lattice model (RLM) for the case of PD-OC 6O9v6Y clusters. The figure clearly shows that the use of RLM with pair and triple interaction parameters leads to a much better agreement than using only pair parameters.

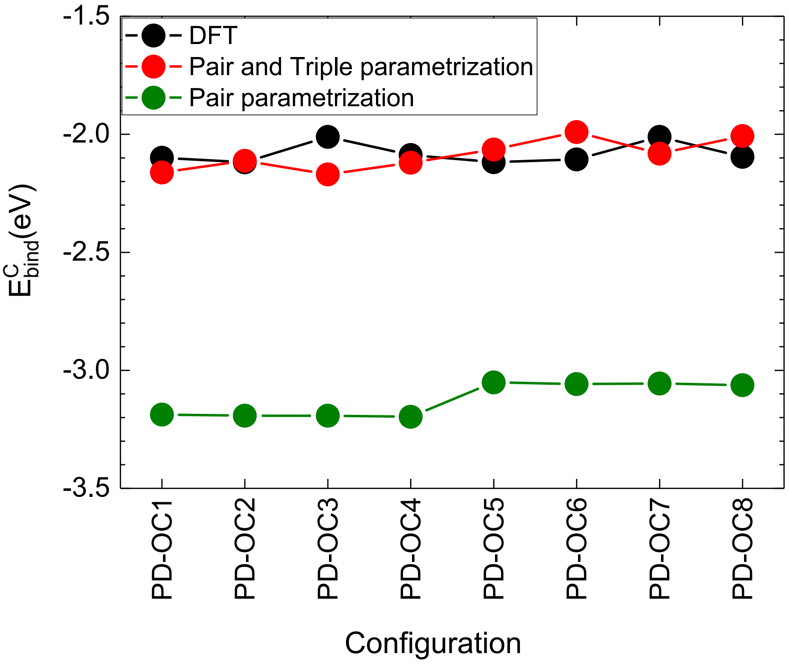

Fig. 3.6: Total binding energy per cluster constituent E^{C}_{bind} for PD-OC 6O9v6Y clusters. Comparison of DFT results with those obtained by the rigid lattice model (see also Fig. 3.3).

3.7 Adding oxygen atoms to relaxed cage-like clusters

Finally it is investigated how the energetics of the O-Y clusters is modified if O atoms are added at octahedral interstitial sites close to the clusters, while the numbers of Fe, Y, Ti atoms, and vacancies remain unchanged. At first one oxygen atom is added to the relaxed cage-like SM 6O9v6Y clusters. The octahedral site is more position of oxygen in Fe matrix. After analyzing the relaxed configuration, first oxygen substituted in octahedral position near by the cluster. In the next steps a further O atom is added to the respective most stable cluster until the stoichiometry of pure Y_2O_3 is reached. In this context 7O9v6Y, 8O9v6Y, and 9O9v6Y clusters are considered and their total binding energy is determined. The most stable cluster configurations 7O9v6Y, 8O9v6Y, and 9O9v6Y obtained after relaxation are characterized by an oxygen atom in the center similar to the OC structures described above. It is interesting that OC-like structures are already formed if one oxygen atom is added to a cage-like configuration. The data for the total binding energy of the 7O9v6Y, 8O9v6Y, and 9O9v6Y clusters and for the corresponding changes of supercell volume and dimensions can be found in Table 3.3. Comparison with Table 3.1 shows that adding one, two, or three O atoms to the cage-like SM 6O9v6Y clusters leads to reduction of the supercell volume, i.e. to more compact cluster structures. At this point the affinity of oxygen to these clusters is discussed in more detail. The binding energy of one oxygen atom to an existing cluster is defined by

$$\begin{aligned} &E_b^O(\text{cluster with } n \text{ O atoms}) = \\ &\qquad E_{bind}(\text{cluster with } n \text{ O atoms}) - E_{bind}(\text{cluster with } n\text{-1 O atoms}) \end{aligned} \tag{21}$$

where negative/positive values mean attraction/repulsion. In the calculation of $E_b^O(\text{7O9v6Y})$ the second term on the right-hand side is $E_{bind}(\text{6O9v6Y})$ of the cage-like 6Y9v6Y cluster given in Table 3.1. The binding energy of a single O atom to the cage-like 6Y9v6Y SM cluster is -4.62 eV which clearly shows a very strong affinity. The clusters 7O9v6Y and 8O9v6Y have a binding energy E_b^O of about -2.92 and -3.09 eV, respectively, i.e. they are still rather attractive to an O atom. Furthermore it was found that the atomic configurations of 7O9v6Y and 8O9v6Y, 9O9v6Y [Figs. 3.7 (a-c)] as well as their characteristics like E_{bind}, etc. are rather independent of whether the SM, PD, or the AS cage-like 6O9v6Y cluster was the initial structure in the process of adding O atoms.

Oxygen atoms were also added step by step to the cage-like SM 7O9v3Y3Ti cluster until the stoichiometry is close to that in pure $Y_2Ti_2O_7$. The values of the total binding energy of 8O9v3Y3Ti, 9O9v3Y3Ti, and 10O9v3Y3Ti clusters are given in Table 3.3. There are also data on the change of supercell volume and on the supercell dimensions. In contrast to the cases

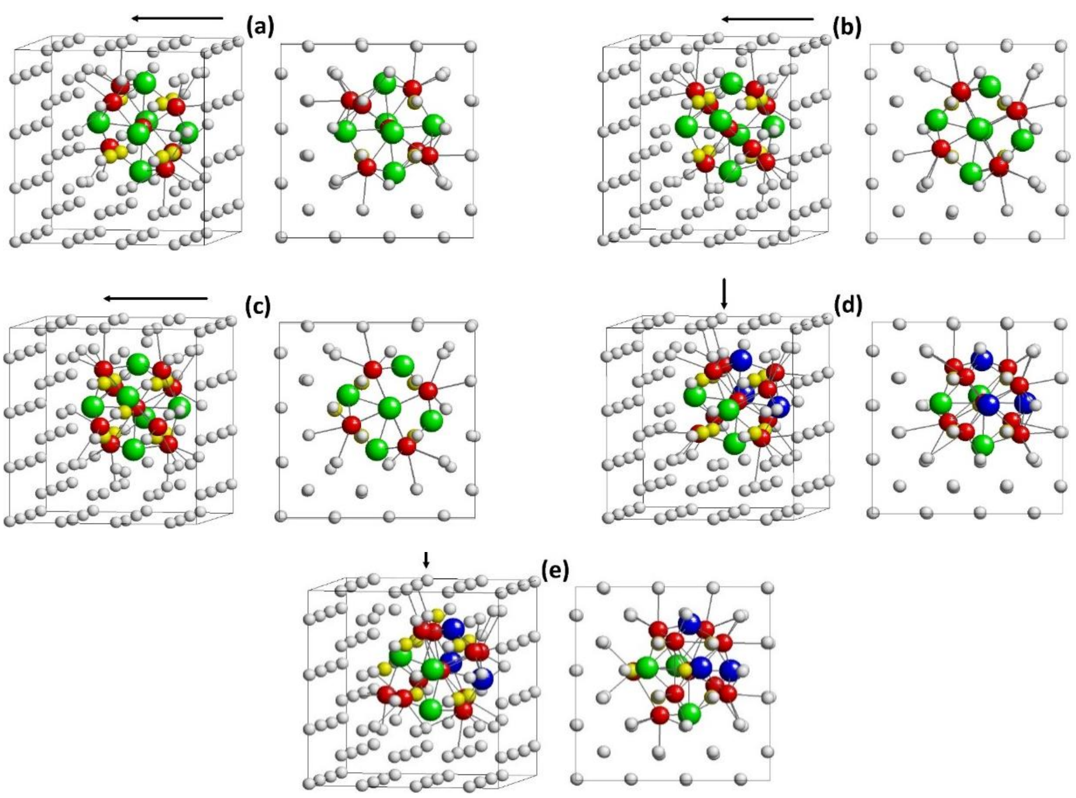

Fig. 3.7: Relaxed cluster configurations formed after stepwise addition of one O atom to the cage-like SM 6O9v6Y cluster [cf. Fig. 3.1 (b)] and to the clusters obtained after addition: 7O9v6Y (a), 8O9v6Y (b), and 9O9v6Y (c). The figure shows also clusters formed by adding two O atoms to the cage-like SM 7O9v3Y3Ti cluster [cf. Fig. 3.2 (b)]: 9O9v3Y3Ti (d), and by adding one O atom to the 9O9v3Y3Ti cluster: 10O9v3Y3Ti (e). If the viewing direction is along the arrow on the left figures in (a-e), pictures as shown on the right figures in (a-e) appear.

described above, adding of one O atom to 7O9v3Y3Ti does not lead to a cluster with oxygen in the center, whereas the 9O9v3Y3Ti, and 10O9v3Y3Ti clusters show such a structure [Figs. 3.7 (d) and (e)]. The O binding energy to the 8O9v3Y3Ti, 9O9v3Y3Ti, and 10O9v3Y3Ti clusters are about -2.26, -2.19, and -2.61 eV, respectively, where the value for $E_{bind}(\mathrm{7O9v3Y3Ti})$ given in Table 3.1 was taken as reference if one O atom is added to 7O9v3Y3Ti. This result demonstrates that also the 7O9v3Y3Ti, 8O9v3Y3Ti, and 9O9v3Y3Ti clusters are rather attractive to a single O atom. In contrast to the clusters without Ti, this attraction is somewhat lower and the presence of the 8O9v3Y3Ti, 9O9v3Y3Ti, and 10O9v3Y3Ti clusters leads to a higher increase of the supercell volume than that in the case of the cage-like SM 8O9v3Y3Ti (cf. Table 3.1).

Table 3.3: Total binding energy E_{bind}, volume change ΔV, and supercell dimensions determined for clusters formed after stepwise addition of one O atom to the cage-like SM 6O9v6Y cluster [cf. Fig. 3.1 (b)] and to the clusters obtained after such an addition. The table shows also data for clusters obtained by stepwise addition of one O atom to the cage-like SM 7O9v3Y3Ti cluster [cf. Fig. 3.2 (b)] and to the clusters obtained after such an addition. With the exception of the case 7O9v3Y3Ti+1O the cluster configurations are depicted in Fig. 3.7.

	128 atom cell		
	E_{bind} (eV)	**ΔV (Å^3)**	**d (Å)**
6O9v6Y+1O	-47.38	38.472	11.429 (a) 11.427 (b) 11.428 (c)
7O9v6Y+1O	-50.29	51.760	11.485 (a) 11.464 (b) 11.436 (c)
8O9v6Y+1O	-53.38	60.048	11.502 (a) 11.501 (b) 11.445 (c)
7O9v3Y3Ti+1O	-42.60	39.198	11.446 (a) 11.442 (b) 11.402 (c)
8O9v3Y3Ti+1O	-44.79	32.868	11.394 (a) 11.422 (b) 11.424 (c)
9O9v3Y3Ti+1O	-47.40	40.927	11.377 (a) 11.487 (b) 11.438 (c)

3.8 Oxygen migration barrier

A possible transition from a cage-like cluster to a cluster with oxygen in the center (OC) may occur via O jump from rim to center. NEB method as implemented in the "vtsttools" *[84]* is used to obtain the migration barriers. Here SM model for 6O9v6Y and 7O9v3Y3Ti clusters are considered for barrier study. The rim sites are mark as 1 and 2 for 6O9v6Y in Fig. 3.1. In Fig. 3.2, all possible rim sites are marked from 1 to 7 for 7O9v3Y3Ti and more feasible case is presented in Fig. 3.8. The result is shown in Fig. 3.8 along with barrier height. In 6O9v6Y cluster the migration barrier from rim to center site is 0.04 eV, which corresponds to a temperature of about 812 K. The barrier for the reverse jump O is much higher (1.70 eV) so that it hardly probable that O can escape from the center after a rim-to-center jump. In the case of the 7O9v3Y3Ti cluster the rim-to-center jump has a barrier of 0.38 eV, while that for the reverse jump is 0.05 eV. Hence O rather stays at rim than center site.

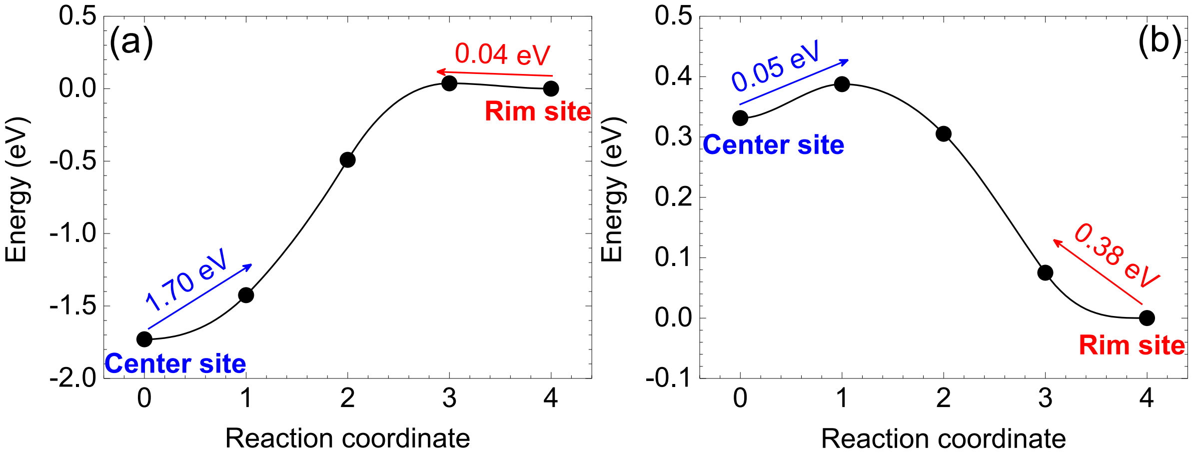

Fig. 3.8: NEB calculated trajectory of O jump in a) 6O9v6Y and b) 7O9v3Y3Ti cluster. Red and blue color arrow show rim-center and center-rim site jumps respectively

3.9 Discussion

The dimensions of the clusters studied in this work are less than 1 nm. This is still below or close to the limit of the resolution of experimental methods allowing for a simultaneous determination of atomic structure and composition of the clusters. The size limitation in this work is mainly due to the requirements for computational resources in DFT calculations.

Present DFT results show that for these small clusters many different atomic configurations with similar stability or energetics are possible at a given composition. Such clusters may be considered as nuclei for further structural evolution and growth. Within the evolution process there may be a selection of favored structures, and if they reach a size of some nm they can be unambiguously identified by advanced experimental methods. As mentioned in the introduction many experimental investigations indicate that it is most probable that the clusters are near stoichiometric oxide structures very similar to Y_2O_3, $Y_2Ti_2O_7$, or Y_2TiO_5.

The search for mechanisms for the transformation between the cluster nuclei studied in this work and the oxide structures observed in these experiments should be a subject of further research. Investigations on the transformation of Cu clusters in bcc Fe, which revealed an evolution from small clusters coherent with the bcc lattice, via 9R and 3R structures towards large fcc Cu clusters may serve as example *[85, 86]*. One could also argue that the general assumption of a complete dissolution of yttria (Y_2O_3) during high-speed milling may be not correct so that nuclei with a cage-like structure may already exist at the beginning of the NFA synthesis by thermal processing. In this manner, one of the possible cluster structures might be favored from the very beginning of the process of NFA formation. In future this issue should be investigated in more detail. On the other hand, it must be mentioned that nanoclusters with the Y_2O_3 structure, and sub-stoichiometric in O, were also formed using YFe_3 and Fe_2O_3 instead of yttria in the process of mechanical alloying *[87, 88]*. This may be considered as an argument in favor of the complete dissolution of yttria in the conventional NFA formation procedure.

In this study it was found that the relaxed O-Y and O-Y-Ti clusters (with vacancies as described above) with oxygen atoms in or near the center (OC) exhibit a stability close to that of the cage-like structure. In these OC clusters the central oxygen atom has 6 Y (or 3Y and 3Ti) neighbor atoms at equal or similar distances like in the rock-salt structure. The relaxed OC clusters containing only O and Y are somewhat more stable than the corresponding cage-like configuration, whereas the opposite result was found for clusters with O, Y, and Ti. Furthermore, adding oxygen atoms to the 6O9v6Y and 7O9v3Y3Ti cage-like clusters also led to such structures with oxygen in the center. At this point it must be mentioned that Hirata et al. [44, 89] proposed a rock-salt structure with a high density of lattice defects for the nm size O-Y-Ti clusters in 14YWT ODS steel. In their investigations scanning transmission electron microscopy in combination with calculations using classical interatomic potentials were employed. On the other hand an yttrium monoxide (YO) with rock-salt structure was recently synthesized by Kaminaga et al. [90] using pulsed laser deposition. These findings and the results of the present work leads to the conclusion that O-Y and O-Y-Ti nm-size clusters with a rock-salt-like structure may be really formed under certain conditions.

The data of the total binding energy per cluster constituent (atoms and vacancies in the cluster) shown in Fig. 3.3 indicate that in O-Y clusters the constituents are stronger bound than in comparable O-Y-Ti clusters, i.e. where Y is partially replaced by Ti.. This may be explained by the fact that the O-Y and the v-Y interactions are more attractive than the O-Ti and v-Ti interactions, whereby the Y-Ti interaction is repulsive (cf. e.g. [40]). Due to this difference in the total binding energy per cluster constituent one may conclude that the driving force for the growth of O-Y clusters is higher than that of O-Y-Ti clusters. This correlates with the experimental observation that the presence of Ti leads to a reduction of the size of the oxide nanoclusters in NFA and to a higher dispersion [18, 19, 21]. The analysis of the clusters showed that the O-Y and O-Ti bond len*gths are close to the second-neighbor distance in bcc Fe* This is in agreement with results on separate O-Y and O-Ti pairs in bcc Fe [37, 38, 42], that exhibit the strongest attraction at this distance.

The results depicted in Figs. 3.3 and 3.6 demonstrate that the description of the clusters within the rigid lattice model and using pair and triple interaction parameters may yield to rather reasonable data for the total binding energy per cluster constituent. Therefore, such a parametrization may be used in future rigid lattice kinetic Monte Carlo simulations with a large number of atoms.

The results of the present work have consequences for the interpretation of the role of the oxide nanoclusters regarding He storage and studies on the interaction of defects such as vacancies and SIA with the clusters. Previous investigations [45, 58] on He management considered only cage-like SM clusters as discussed in the work of Barnard et al. [35]. Therefore, in chapter 4, cage-like and OC clusters 6O9v6Y and 7O9v3Y3Ti are investigated regarding He storage capacity and irradiation induced defect management.

3.10 Summary

In summary, our DFT investigations on possible atomic configurations of O-v-Y and O-v-Y-Ti clusters embedded in bcc Fe revealed a variety of possible cluster structures with similar energetics: Different cage configurations obtained by SM, AS, and PD models as well as configurations with oxygen in the center found after relaxation of SM-OC, AS-OC, and PD-OC models. This contradicts the opinion in recent theoretical literature that favors the SM model *[35, 45, 58]*. Furthermore, the role of Ti was investigated by comparing results for O-v-Y and O-v-Y-Ti clusters, and the binding of oxygen monomers to the clusters was studied. Due to the limitations of computational resources, in the present work only small clusters with dimensions below 1 nm could be treated. This size is still too low for a simultaneous determination of atomic structure and composition by advanced experimental methods. These small clusters may be considered as nuclei for further structural evolution and growth. In all cases studied the absolute value of the total binding energy per cluster constituent becomes lower if Y is partially replaced by Ti, i.e. the driving force for the growth of O-Y clusters may be higher than that of O-Y-Ti clusters. This may be correlated with the experimental observation that the presence of Ti leads to a reduction of the size of the oxide clusters in nanostructured ferritic alloys and to a higher dispersion. If Ti is not present, clusters with oxygen in the center are slightly more stable than the corresponding cage-like clusters. The opposite result was obtained for clusters with Ti. In the present work it was also shown that adding O atoms to cage-like clusters at nearby octahedral interstitial sites leads to structures with O in the center. Clusters with oxygen in the center can be considered as nuclei for nm-size clusters with rock-salt structure. Such a structure was also derived from the analysis of experimental data on yttria-based NFA alloys, cf. Hirata et al. *[44, 89]*. However, the presently prevailing opinion is that most of those nanoclusters are near-stoichiometric cage-like oxide structures *[21]*

X ------------------------------ X

4. Interaction of O-Y and O-Y-Ti clusters embedded in bcc Fe with He, vacancies and self-interstitial atoms

---

4.1 Introduction

In this chapter, the most stable atomic configurations obtained in chapter 3 for two O-Y and two O-Y-Ti cluster models are considered and their interaction with He, a vacancy and a self-interstitial atom (SIA) is studied by DFT calculations. In this manner the influence of cluster composition as well as morphology can be revealed. The binding and incorporation energy of the defect species are determined for the different cluster models. For this purpose the He atom, the vacancy, or the SIA are initially set on selected sites inside or near the cluster, and after relaxation the final structure and energetics is analyzed. Also, the interaction of two or three He atoms with O-Y and O-Y-Ti clusters is investigated and selected barriers for He migration are calculated. Besides the energetics, i.e. binding and incorporation energy, these barriers are important quantities in order to understand the evolution of the He storage by the clusters at finite temperatures.

4.2 Cluster models and possible sites for He, vacancies and self-interstitial atoms

In chapter 3, different structural models for O-Y and O-Y-Ti clusters in bcc Fe were considered and for a given composition, the most stable atomic configuration was obtained by DFT calculations. Due to limitations of computational resources, the largest clusters investigated in chapter 3 mainly consist of (i) 6 O atoms, 9 vacancies (v) and 6 Y atoms, and (ii) 7 O, 9 v, 3 Y, and 3 Ti. In this context all sites of the underlying perfect bcc lattice which are not occupied by metal atoms (Fe, Y, Ti) are counted as vacancies. That means that all O atoms are assigned to vacancies. The above definition of vacancies is not strictly necessary. However, such a definition may be helpful to better understand the properties of the clusters. The equivalence of investigations the cluster energetics using or not using v was shown in chapter

3. Two kinds of clusters were studied: (i) cage-like clusters with a vacancy in the center surrounded by an octahedron of Y and Ti atoms, and (ii) clusters with oxygen at this central site. The first model is directly derived from the atomic structure of the oxides Y_2O_3 and $Y_2Ti_2O_7$, whereas the second was obtained in chapter 3 and has a core similar to the rock-salt structure. Compared to the pure oxides the two models are depleted in oxygen. The energetic properties of both types of clusters are very similar: If Ti is not present clusters with oxygen in the center are slightly more stable than the corresponding cage-like structures. The opposite holds for clusters with Ti. Fig. 4.1 illustrates the relevant atomic configurations obtained by the DFT calculations in chapter 3. In the present work the interaction of He with these clusters is investigated. Possible He sites are classified in the following manner.

a) He on a vacancy site in the center of cage-like (CL) clusters: This position corresponds to an octahedral interstitial site in bulk Y_2O_3 or $Y_2Ti_2O_7$.

b) He on a vacancy site at the cluster-iron interface: Both in CL clusters and in clusters with oxygen in the center (OC) vacant bcc sites which are not assigned to oxygen atoms are available there.

c) He on interstitial sites: In the interface region He might occupy tetrahedral and octahedral interstitial sites in the underlying bcc lattice. It is known from literature that He is an interstitial foreign atom in bcc Fe, whereby the tetrahedral site is most stable followed by the octahedral site *[45, 48, 53, 91-93]*. Present investigations are limited to such interstitial sites with a distance of less or equal than $1.5\,a$ to the center of the cluster, where a is the lattice constant of bcc Fe.

The possible positions of He atoms are also shown in Fig. 4.1. After He is placed on a given position the system is relaxed by DFT calculations. In some cases the assumed He site may be really stable in others it may be unstable. Based on results on the interaction of a single He

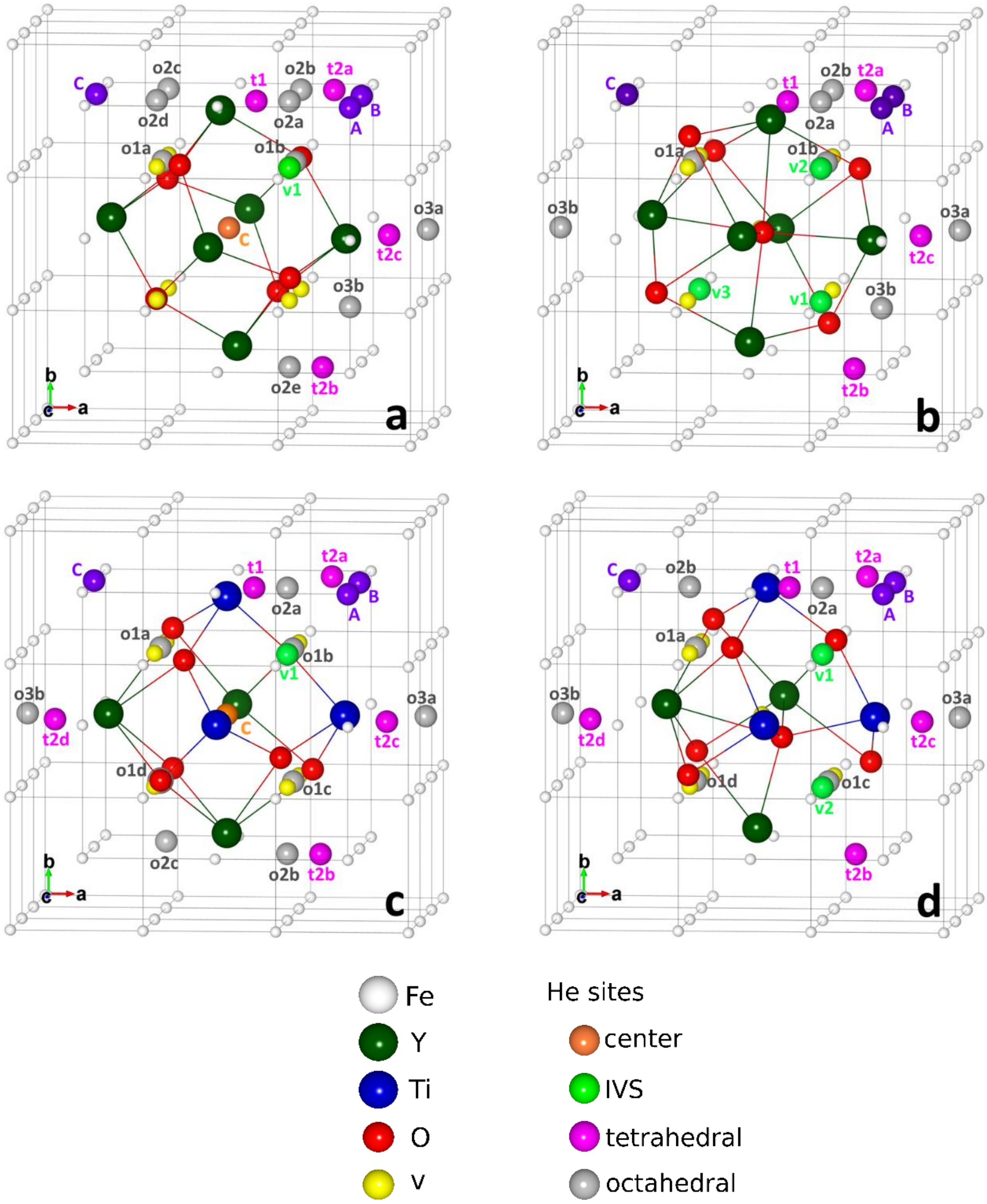

Fig. 4.1: The initial He sites considered for the calculation in the case of the cage-like (CL) O-Y cluster model (a) the O-Y cluster with oxygen in the center (OC) (b), as well as the CL O-Y-Ti cluster (c) the OC O-Y-Ti cluster (d). White, green, blue and red balls represent Fe, Y, Ti and O. Vacancies (v) which belong to the clusters (see section 2) are represented by yellow balls. Gray and magenta balls denote octahedral and tetrahedral interstitial sites in the underlying bcc lattice. Gold and light green balls are vacant sites at the cluster center and the cluster-iron interface. Purple balls show sites for an additional vacancy or an additional self-interstitial atom (SIA). Only a part of the supercell is shown in the figures.

atom with the cluster, in a further step two or three He atoms are placed on selected sites and the energy of the supercell is minimized using DFT. Besides the sites found to be stable after adding a single He to the cluster, some additional configurations are studied in which two or three He atoms are placed into the environment of these sites. The relaxed atomic configurations of the clusters with one, two or three He atoms are shown in the Appendix-B [*App-B*]. Three possible sites (A, B, C) for an additional vacancy (v) or an additional self-interstitial atom (SIA) are shown in Fig. 4.1 as well. The relaxed cluster configurations with v or SIA are also provided in the Appendix-B [*App-B*].

4.3 Calculation procedure

We carried out spin-polarized calculations in the framework of density functional theory (DFT) as implemented in Vienna ab-initio simulation package (VASP) *[61, 64, 82]*. For details we refer to chapter 3. The only difference is the fact that for test calculations with the larger supercell with 250 bcc sites a 2x2x2 k point sampling is used for integration over the Brillouin zone. After placing He into the supercell according to one of the above mentioned models the position of atoms as well as the volume and shape of the supercell are relaxed, so that the force on atoms and the total stress/pressure on the supercell are minimized. In the present calculation the accuracy level of residual force on any atom and of the total energy change between successive ionic iterations are set to 10^{-2} eV/Å and 10^{-5} eV, respectively.

The interaction between He and a cluster containing O, v, Y, and Ti can be characterized using the binding energy of He to the cluster. The binding energy of m He atoms is given by

$$E_b^{mHe} = E_{bind}\left(O,\mathrm{v},Y,Ti;mHe\right) - E_{bind}\left(O,\mathrm{v},Y,Ti\right) \tag{22}$$

where $E_{bind}\left(O,\mathrm{v},Y,Ti;mHe\right)$ and $E_{bind}\left(O,\mathrm{v},Y,Ti\right)$ are the total binding energies of the cluster with and without m He. In the present work the cases $m=1,2,3$ are considered. For the cluster configurations shown in Fig. 4.1 the quantity $E_{bind}\left(O,\mathrm{v},Y,Ti\right)$ was determined in chapter 3. The general relation for the total binding energy of an embedded cluster that consists of n monomers, e.g. a certain amount of O, Y, Ti, He atoms and vacancies, is defined by

$$E_{bind}(X_1+X_2+...+X_n)=E(X_1+X_2+...+X_n)+(n-1)E^0-\sum_{i=1}^{n}E(X_i) \tag{23}$$

$E(X_1+X_2+...+X_n)$ and $E(X_i)$ denote the total energy of supercell with the $X_1+X_2+...+X_n$ cluster and the total energies of supercells with the monomers X_i, respectively, while E^0 is the total energy of a supercell containing perfect bcc Fe. By definition E_b and E_{bind} are negative if attraction dominates. The data for $E(X_i)$ are determined assuming O on an octahedral interstitial site in bcc Fe, and Y, Ti as well as the vacancy on a bcc lattice site. In a similar manner the binding energy of an additional vacancy (V) or an additional self-interstitial atom (SIA) to the cluster is given by

$$E_b^V=E_{bind}\left(O,\text{v},Y,Ti;V\right)-E_{bind}\left(O,\text{v},Y,Ti\right) \tag{24}$$

and

$$E_b^{SIA}=E_{bind}\left(O,\text{v},Y,Ti;SIA\right)-E_{bind}\left(O,\text{v},Y,Ti\right) \tag{25}$$

Another characterization of the interaction of m He with the cluster is possible via the incorporation, solution or formation energy *[58]*

$$E_{incorp}^{mHe}=E\left(O,\text{v},Y,Ti;mHe\right)-E\left(O,\text{v},Y,Ti\right)-mE^A\left(He\right) \tag{26}$$

where $E\left(O,\text{v},Y,Ti;mHe\right)$ and $E\left(O,\text{v},Y,Ti\right)$ are the total energy of the supercell containing the embedded cluster with and without m He, respectively, and $E^A\left(He\right)$ is the total energy of a single He atom (0.00705 eV). The corresponding incorporation or formation energies for V and SIA are

$$E_{incorp}^{V}=E\left(O,\text{v},Y,Ti;V\right)-E\left(O,\text{v},Y,Ti\right)+E^A\left(Fe\right) \tag{27}$$

and

$$E_{incorp}^{SIA} = E\left(O, \mathrm{v}, Y, Ti; SIA\right) - E\left(O, \mathrm{v}, Y, Ti\right) - E^{A}\left(Fe\right) \tag{28}$$

Here $E^{A}\left(Fe\right)$ is the energy per atom (or its chemical potential) in perfect bcc Fe.

Following the energetic calculation, we consider CL clusters and determine the migration barrier for He jumps from the center to sites at the cluster-Fe interface. The Nudged Elastic Band(NEB) *[76-78]* method as implemented in the "vtsttools" *[84]* is used to obtain the barriers.

4.4 Energetics and structure of relaxed cluster configurations containing one He atom

The center of the CL cluster shown in Fig. 4.1 (a) is found to be the most stable He site, with a binding energy E_b^{He} of -3.31 eV and an incorporation energy E_{incorp}^{He} of 1.25 eV. As already mentioned in section 4.2 this center position corresponds to an octahedral interstitial site in Y_2O_3. For a larger CL cluster composed of the same kind of atoms Sun et al. *[45]* found an incorporation energy of 0.92 eV for such a He site. The deviation from our result may be due to the different sizes of the clusters as well as the different cell sizes and k-point grids used in the corresponding DFT calculations. Danielson et al. *[48]* and Sun et al. *[45]* obtained 0.62 and 0.92 eV, respectively, for the same He site in bulk Y_2O_3. It is worth mentioning that in bulk Y_2O_3 the tetrahedral interstitial site with four Y atoms in the environment is the most stable He site, followed by the octahedral site surrounded by six Y. A further stable site is obtained by placing He on one of the two equivalent vacancy sites (v1) of the CL cluster shown in Fig. 4.1 (a). The relaxed configuration (see Appendix-B [*App-B*]) is called interfacial vacant site (IVS) and is slightly different from v1. The corresponding binding energy E_b^{He} is -3.18 eV and the incorporation energy E_{incorp}^{He} is 1.37 eV. In the following the term IVS is generally used for relaxed positions of He initially placed on a vacant site. The various tetrahedral and octahedral interstitial sites with a distance less or equal than $1.5a$ from the center of the cluster are not stable. Instead relaxation strongly changes the atomic configurations and the

He atom is shifted towards the cluster. In three cases (o1b, o2a, t1) the final CL structure and the corresponding energetics is very similar to that obtained in the IVS case. In further nine cases a transformation to OC configurations occurs, with He close to an IVS (see below) Such a drastic structural change is certainly due to the small size of the cluster. Finally (o1a), an atomic configuration with He on an interfacial interstitial site (IIS) in the vicinity of the octahedron edge with two Y, and close to two O atoms, is found with E_b^{He} (E_{incorp}^{He}) of -2.01 (2.54) eV(see Appendix-B [*App-B*]). It should be noticed that in the following the term interfacial interstitial site (IIS) is generally used for relaxed He sites which are neither a center site nor an interfacial vacant site (IVS).

In the case of the OC cluster depicted in Fig. 4.1 (b) the center is already occupied by an oxygen atom so that He cannot be placed there. He is stable on the three possible vacancy sites: The IVS near v1 has a binding energy of -2.56 eV (incorporation energy: 2.02 eV) while for the IVS near v2 and v3 -2.71 (1.84) eV and -2.81 (1.74) eV are obtained, respectively. Again, the tetrahedral and octahedral interstitial sites are not stable upto the distance of $1.5a$ distance. Placing He on such positions leads to strong atomic rearrangements and often to a shift of He towards the cluster. The corresponding atomic arrangements are very similar to those obtained when CL clusters are transformed to an OC structure after adding He to those sites, as mentioned above. In nine cases He relaxes to an IVS. In two cases (o3a, t2b) the He binding energy is about -2.65 eV (incorporation energy of 1.91 eV) and the structures correspond to that of the IVS near v1. After relaxation of o1b, o2a, o3b, t1, t2a, and t2c He binds with -2.75 eV to the OC cluster and the atomic configurations are similar to the IVS near v2. He placed on o3c relaxes to a IVS close to v3 with -2.81 (1.74) eV. In other two cases (o1a, o2b) He occupies interfacial interstitial sites (IIS) in the environment of an octahedron edge formed by two Y atoms, with and without two O atoms in the vicinity. The energetics of these configurations is similar, with E_b^{He} (E_{incorp}^{He}) of -2.10 (2.46) eV and -2.07 (2.48) eV.

In CL cluster containing O, v, Y, and Ti [Fig. 4.1 (c)] the center site is the most stable position for He with a binding (incorporation) energy of -2.78 (1.78) eV. This finding matches well with the result of Danielson et al. [*58*] who reported a value of 1.85 eV for the incorporation energy for He at the center of the same type of cluster. The result may be also compared with the incorporation energy of He on an octahedral interstitial site of bulk $Y_2Ti_2O_7$. Yang et al. [53] and Danielson et al. [46] obtained 0.94 and 0.86 eV, respectively whereas Sun et al. [52] reported a value of 1.24 eV. As in the case without Ti, the incorporation of He into the center of the small cluster embedded in iron requires more energy than placing He on a similar site in the bulk oxide. In contrast to Y_2O_3 in bulk $Y_2Ti_2O_7$ the octahedral interstitial site surrounded by six Y atoms is the most stable He site, followed by the tetrahedral site with 4 Y atoms in the environment. He is also stable on the IVS near v1 [Fig. 4.1 (c)], with binding (incorporation) energy of about -2.38 (2.18) eV. This configuration was also found by Danielson et. al. [58] who reported a value of 2.26 eV for E_{incorp}^{He}. Ten tetrahedral and octahedral interstitial sites with a distance less than $1.5a$ from the center of the cluster are not stable. In two cases (o1b, o2a) after relaxation He occupies the IVS near v1 (see above). Three cases (o1d, o2b, o2c) yield relaxed structures that were also investigated by Danielson et. al. [58] . In the following their data for E_{incorp}^{He} are given in brackets: (i) He on an IIS close to the octahedron edge with 2Y at corners with E_b of -2.42 eV and E_{incorp}^{He} of 2.14 (2.19) eV, (ii) He on an IIS close to the face with 1 Y and 2 Ti at corners with E_b^{He} of -2.31 eV and E_{incorp}^{He} of 2.25 (2.31) eV, and (iii) He on an IIS near the octahedron face with 3 Y at corners with E_b^{He} of -2.26 eV and E_{incorp}^{He} of 2.30 (2.34) eV. Hence, the results of present work agree well with literature data. From the five remaining configurations (o1a, t2d, t2b, o3b, o1c) two are similar to that of (i), one is similar to that of (ii), one is similar to that of (iii), and in the last case He is asymmetrically placed on an IIS close to the octahedron face with 2Y and 1 Ti with E_b^{He} (E_{incorp}^{He}) of -2.26 (2.30) eV. In contrast to results for the CL cluster of Fig. 4.1 (a) the relaxed IIS structure (i) is more stable than He on the IVS. Interestingly, the tetrahedral and octahedral interstitial sites (t2a, t2c o3a) with distances 3.714, 3.111, and 4.173 Å from the center of the cluster and closer to Ti atoms than to Y atoms remain stable after relaxation. He on the two tetrahedral interstitial sites (t2a, t2c) have a binding (incorporation) energy of -1.55 (3.01) and

-0.30 (4.26) eV and He on the octahedral site (o3a) has E_b^{He} (E_{incorp}^{He}) of -0.24 (4.32) eV. Obviously, the presence of Ti reduces the attraction of He by the cluster since such stable sites are not observed in the case of the CL clusters without Ti [Fig. 4.1 (a)].

In the OC cluster shown in Fig. 4.1 (d) the IVS near v1 is stable with E_b^{He} (E_{incorp}^{He}) of -2.39 (2.17) eV. The IVS near v2 is also stable with E_b^{He} (E_{incorp}^{He}) of -2.18 (2.87) eV. He on o2a, t1, and t2c relaxes towards the first IVS with very similar structure and energetics. He on o1c and t2b relaxes to an IIS near the octahedron face with 2 Ti and one Y on the corners, with E_b^{He} (E_{incorp}^{He}) of -2.34 (2.21) eV. The remaining seven tetrahedral and octahedral interstitial sites are also not stable and have different energetics (E_b^{He} varies from -2.68 to -1.80 eV) and final atomic configurations is given in (see Appendix-B *[App-B])*. In all cases, He is shifted towards the cluster during the relaxation.

4.5 Relaxed cluster structures with two He atoms

Adding two He atoms to the CL cluster of Fig. 4.1 (a), at the center and at an IVS, results in a binding energy of -6.51 eV. The comparison with the relaxed configurations after separate addition of a single He to respective sites (E_b^{He}: -3.31 and -3.18 eV, see above) shows that each He binds more or less separately. A similar result is obtained for two He on the two equivalent IVS: Both He bind with -6.33 eV while E_b^{He} for single He on IVS is -3.18 eV. Inserting one He into the center, the other as an IIS near a octahedron edge with two Y on the corner and two O and two v in the environment leads to E_b^{2He} = -5.32 eV which corresponds to the sum of E_b^{He} for separate addition of He to the two sites. Placing two He atoms symmetrically close to v1, with orientation along the <100> direction, yields a binding energy of -5.43 eV which is less than the sum of the values of E_b^{He} obtained by adding one He to a vacancy site. The final He arrangement is rather asymmetric with respect to v1. If the He dimer is oriented along <110> a less stable relaxed configuration (-5.11 eV) is obtained, whereby both He atoms are located symmetrically to v1, the orientation is along <110> and parallel to the closest octahedron face.

If two He atoms are inserted into the supercell with the OC cluster shown in Fig. 4.1 (b), on the IVS near v2 and v3, a binding energy of -5.51 eV is obtained. Adding two He to the IVS near v1 and v3 gives -5.39 eV. The comparison with results of section 4.4 (IVS near v2: -2.71, IVS near v3: -.2.81, and IVS near v1: -2.53, v3: – 2.81) shows that the two He atoms bind separately. One He on the IVS near v2 and one He on an IIS close to two Y on an octahedron edge gives a binding energy of -4.92 eV which is slightly more stable state than one would expect from the sum of the respective values of E_b^{He} (-2.71 and - 2.10 eV) for two single He on these sites. On the other hand, if two He atoms are placed symmetrically close to v1, with orientation along the <100> directions, a more stable state with a binding energy of -5.27 eV is obtained. More details can be found in the Appendix-B *[App-B]*.

In the case of the CL-cluster of Fig. 4.1 (c) adding He at the center and on the IVS near v1 leads to a binding energy of -5.18 eV. This corresponds to the sum of the values of E_b^{He} (-2.78 and -2.38 eV) for a single He on the respective sites. Placing the first He at the center and the second on the site t2d leads to a relaxed state, with one He in the center and the other on an IIS close to the two Y at the edge of the octahedron, and to a binding energy E_b^{2He} = -5.42 eV. This corresponds to a slightly more stable configuration than one would expect from the sum of E_b^{He} values for single He atoms at one of the two sites (-2.78 and -2.42 eV). Placing two He atoms symmetrically close to v1 and with an orientation along the <100> direction yields a binding energy of -3.87 eV. The final arrangement of the two He atoms is asymmetric with respect to the v1 and is located near the 3Ti face of the octahedron. Orienting the He dimer along <110> yields a similar binding energy (-3.84 eV). In the final configuration both He atoms are situated symmetrically to the v1 and the orientation remains along <110> parallel to the 3Ti octahedron face.

After inserting two He on the two IVS of the OC cluster depicted in Fig. 4.1 (d) a binding energy of -4.69 eV is obtained. This is somewhat more stable than expected from the sum of the values of E_b^{He} for the IVS near v1 (-2.39 eV) and v2: (-2.18 eV). The addition of a He dimer close to v2 near the 2Ti-1Y face of the (distorted) octahedron, with an orientation along the <110> direction, yields a binding energy of -4.78 eV. Interestingly, this configuration is more stable than that with two He on the available IVS near v1 and v2. The relaxed configuration is symmetric with respect to v2, oriented along <110>, and is parallel to the 2Ti-1Y face. Putting a He dimer close to v1 near the 3Ti face with orientation along <100> yields even a more attractive state with a binding energy of -5.31 eV. In the relaxed configuration one He atom is close to v1, whereas the other is close to the octahedron edge with two Ti on the corners.

4.6 Relaxed cluster structures with three He atoms

Placing one He atom at the center and two He on the IVS of the CL cluster of Fig. 4.1 (a) yields a binding energy for the three He atoms of E_b^{3He}=-9.68 eV which corresponds to the sum of the values of E_b^{He} for single He atoms at each of these sites. If one He is at the center, the other on IVS, and the third on an IIS close to the two Y atoms at the corner of an octahedron edge (with two O atoms in the environment) a binding energy of -8.50 eV is obtained. Again, this is nearly equal to the sum of the respective E_b^{He} data for a single He atom. The addition of three He atoms symmetrical to v1 and relaxation yields a binding energy of -8.41 eV which is exactly the sum of the binding energy for the relaxed dimer near v1 (-5.10 eV) plus the value of E_b^{He} (-3.31 eV) for a single He in the center.

Three He on the three available IVS of the OC cluster of Fig. 4.1 (b) results in a binding energy of -8.11 eV which is nearly equal to the sum of the respective E_b^{He} data for single He addition (IVS near v1: -2.53, IVS near v2: -2.71, IVS near v3: -2.81 eV). One He on IVS near v2 and one on an IVS near v3, and a third on an IIS close to the two Y atoms at the corner of an octahedron edge (with two O atoms in the environment) yields -7.61 eV which is the sum of the respective E_b^{He} data (-2.71, -2.81, -2.10) obtained by adding single He on the corresponding sites. Placing three He atoms in the environment of v1 leads to a symmetrical trimer around this site with an arrangement parallel to the octahedron face(see Appendix-B [App-B]). This is a surprisingly stable state with a trimer binding energy of E_b^{3He} =-7.97 eV.

Adding the first He atom to the center of the CL cluster of Fig. 4.1 (c), the second to the IVS and the third to an octahedral interstitial site (o2b) causes the rearrangement of the oxygen atom close to the third He atom. The second and the third He atoms are arranged in a symmetric manner, leading to a binding energy of -7.82 eV for the three He atoms. This is by about 0.3 eV more stable than the sum of the values of E_b^{He} obtained for a single He at the center and on the IVS (-2.78 eV, two times -2.38 eV). On the other hand, placing 3 He atoms close to v1 near the 3Ti face of the octahedron yields a configuration with a slightly asymmetric trimer and a binding energy of -5.23 eV.

He on the two available IVS plus one He on the octahedral site o2b yields a relaxed configuration with a binding energy E_b^{3He} of -6.89 eV and the He atoms are slightly rearranged. The absolute value of E_b^{3He} is higher than one would expect from data of E_b^{He} for one He at the corresponding sites (-2.39, -2.18, -1.80). After relaxation of three He atoms that were introduced into the OC cluster of Fig. 4.1 (d) close to v1 near the (distorted) octahedron with 3 Ti atoms, a slightly modified trimer is found with a binding energy of -6.16 eV which is more stable than the corresponding trimer in the CL cluster (see above).

4.7 Discussion of the energetics of He-cluster interaction

Up to a distance of $1.5\,a$ from the cluster center, He is strongly attracted by each of the four different cluster structures considered in this work. Within this region, He cannot be stabilized on most of the tetrahedral and octahedral interstitial sites of the underlying bcc lattice but relaxes to positions that are closer to the cluster than the initial sites. The main reason for the He trapping capability of the clusters is the existence of enough open or empty volume inside the CL clusters and at cluster-Fe interfaces. He as an inert gas atom prefers to reside in such regions. The incorporation energy of He on sites near the interface to the iron matrix is lower than in bulk bcc Fe (4.56 eV) but higher than in bulk Y_2O_3 (0.62 *[48]* or 0.92 eV

[45]) or $Y_2Ti_2O_7$ (0.94 [53], or 0.86 [46], or 1.24 eV [52]). This was also pointed out by Sun et al. [45] and Yang et al. [56]. Such a trend can be explained qualitatively by the electronic structure of the respective solids: In bulk bcc Fe the valence electrons are highly non-localized so that a completely empty volume does not exist, whereas in the bulk oxides the electrons are much more localized due to the predominantly ionic character of the bonds.

In this work, the open or empty volume is also pictured by vacancies in the underlying bcc lattice that are not assigned to an oxygen atom. He at the vacant site in the center of a CL cluster is more stable than on an IVS at the cluster-Fe interface. Due to the small cluster size, the incorporation energy at the center site is somewhat higher than at the comparable site in bulk Y_2O_3 or $Y_2Ti_2O_7$. On other stable sites in the interstice between the cluster and the iron matrix (IIS), the absolute value of the He binding energy E_b is often smaller than that on IVS. However, there are also IIS in clusters with Ti, where He is more stable than on an IVS. Comparing He on IVS of CL and OC clusters without Ti, He is found to be more stable in CL clusters, whereas no significant difference exists for the clusters with Ti. In clusters without Ti, He is more stable in the center and on IVS than in those with Ti. In the case of clusters with Ti more different IIS configurations are found than for those without Ti.

Separate DFT calculations on the binding energy between He on a tetrahedral interstitial site in bcc Fe and substitutional Y or Ti as well as O on an octahedral interstitial site were performed. It was found that the Y-He pair shows the strongest attraction (-0.46 eV) followed by the O-He pair (-0.34 eV) and the Ti-He pair (-0.14 eV). These findings help to explain qualitatively why clusters without Ti attract He stronger than those with Ti. However, one should also keep in mind that the clusters with Ti contain one more oxygen atom and one less vacant site than those without Ti. As already mentioned above, these vacant sites are most important for the attraction of He. In bulk bcc Fe the v-He pair has a binding energy of -2.34 eV. On IVS in clusters with Ti a similar value is obtained (-2.38 eV in CL, -2.18 and -2.39 eV in OC clusters), whereas higher absolute values are found in clusters without Ti (-3.18 eV in CL and -2-53, -2.71, -2.81 eV in OC clusters).

In many cases the binding energy of two He atoms to the cluster is about equal to the sum of the E_b^{He} values for a single He on the respective site. He dimers close to a vacant site are mostly less stable than two He on separate IVS. However, in the OC cluster with Ti opposite results are found. A sum rule also holds for the binding energy of three He if these are on the center site, on an IVS, and on a certain IIS. He trimers close to a vacant site have different energetics so that it is not possible to derive a general rule from the large but limited number of examples considered here. The finding that the addition of two or three He atoms to the environment of a single vacant site is still energetically favorable shows that the cluster structures exhibit a very high He storage capability. Although comprehensive investigations on different sites of one, two, or three He atoms in the region of the clusters were performed in this work, it is obvious that there are still other possible configurations since the potential energy landscape is very complex, in particular in and near clusters with Ti.

The findings obtained with the supercell consisting of 128 bcc lattice sites have been checked by investigating selected cases in a cell with 250 lattice sites. In such a manner the influence of the periodic images can be estimated. The results are provided in the Appendix-B *[App-B]*. In the larger cell very similar relaxed atomic configurations are found and also the values for binding and incorporation energy are nearly equal. In agreement with results for the smaller supercell very weak or repulsive interaction between the cluster and He is observed if He is apart at more than the distance of $1.5a$ from the cluster center. At these sites, the incorporation energy of He is nearly equal to that in pure Fe.

4.8 He migration barriers near the clusters

At given temperature the He storage capability of an oxide nanocluster in iron is not only determined by the energetics of the particular stable He site inside the cluster or at the cluster-Fe interface but also by the migration barriers a He atom has to overcome in order to reach these sites. In the following, the focus is on barriers between stable He sites at the interface and the center site in CL clusters.

For clusters without Ti only two stable sites were found at the interface (see section 4.4). Figs. 4.2 (a) and (b) show barriers for the He jump between an IVS and the center and between an IIS (close to an octahedron edge) and the center, respectively. The second migration path is not relevant because of the high barriers. The first one is important since the barrier for He jump to the center is very low (0.07 eV), i.e. only slightly higher than the migration barrier of He in bulk bcc Fe (0.06 eV *[91]*). Therefore, He can be easily trapped on the center site at temperatures relevant for practical applications. On the other hand, leaving the center site is more difficult since the barrier is by about a factor of three higher. Several barriers between stable He sites at the cluster-iron interface and the center site were determined for the CL cluster with Ti. Figs. 4.2 (c-e) depict barriers for jumps from the center to stable interfacial sites. These sites were also found by Danielson et. al. *[58]* (cf. section 4.4). Surprisingly the barrier between the IVS and the center site is very high. The most relevant jump is that from the IIS near the octahedron face with 2 Ti and one Y on the corner to the center site, with a barrier of 0.14 eV (IIS relaxed from o2b). The barriers for jumps to the center site from: (i) a He site close to an octahedron edge with 2Y at corners (IIS relaxed from o1a), (ii) a He site in the region of the 2Y-1Ti octahedron face (IIS relaxed from o1c), and (iii) another He site close to the octahedron edge with 2Y at corners (IIS relaxed from o1d) are similar [Figs. 4.2 (e-g)]. These jumps are less probable than that shown in Fig. 4.2 (d) because of the higher barrier of about 0.35 eV. In cases (i)-(iii) the barriers for a jump from the center to a site at the interface are comparable with that in Fig. 4.2 (d) so that in all these cases He is effectively trapped.

The results on the barriers for jumps between a stable He site at the interface and the center of CL clusters clearly show preferred minimum energy paths with high importance for He storage. Interestingly, the barrier for a jump to the center of the CL cluster without Ti is lower than for the CL cluster with Ti. Present findings also indicate possible migration paths for He incorporation into larger clusters. However, it must be also noticed that not only the octahedral sites with 6 Y or 3 Y and 3 Ti atoms in the environment can store He (which corresponds to the center site of the CL clusters), but also other sites existing in the interstice of the oxide (Y_2O_3, $Y_2Ti_2O_7$) structures, such as tetrahedral and octahedral sites with different atomic environments *[45, 46, 48, 52]*.

4.9 Relaxed cluster configurations with one additional vacancy

The calculation of the formation or incorporation energy of single vacancy in bcc Fe yields a value of 2.17 eV which is in agreement with literature data *[94, 95]*. To investigate the interaction between the vacancy (v) and the clusters shown in Fig. 4.1 we have selected three particular bcc sites close to the clusters. The corresponding binding (incorporation) energies of v are given in Table 4.1 and the atomic configurations before and after relaxation are provided in the Appendix-B *[App-B]*.

First a vacancy (v) at the bcc site A, at first neighbor distance to an IVS, is considered. The v is weakly attracted by all the four cluster structure. Interestingly, the attraction is somewhat stronger by the clusters with Ti where the v is near the face with 3 Ti atoms on the corner. In the second case, with the v on the site B, and nearly at first neighbor distance to an oxygen atom, or exactly at first neighbor distance to the vacant site assigned to the O atom, the attraction of v is stronger than on site A. The absolute value of the binding energy is higher for the clusters without Ti. In contrast to v on site A, the attraction by OC clusters is stronger than that by CL clusters. Placing the v on site C, nearly at first neighbor distance to two O atoms leads to relatively strong deformations of the CL clusters, whereas the form of the OC clusters is only slightly modified. In these four cases the absolute value of the binding energy is much higher than in the two examples discussed before. Clusters with Ti are slightly less attractive than those without Ti.

Depending on the selected V site a weaker or stronger attraction by the clusters is found. Our results agree qualitatively with those of Brodrick et al. *[54]* who found that an interface between Y_2O_3 and bcc Fe can act as trap for v. If v is placed at first neighbor distance (site A) to an IVS the absolute value of the binding energy is relatively small. The attraction of v on site A close to the octahedron face with 3 Ti atoms on corners [see Figs. 4.1 (c) and (d)] is comparable with the binding energy between two vacancies in pure Fe at the first neighbor distance (-0.16 eV, see e.g. *[80]*). This is not surprising since the v on site A has this distance

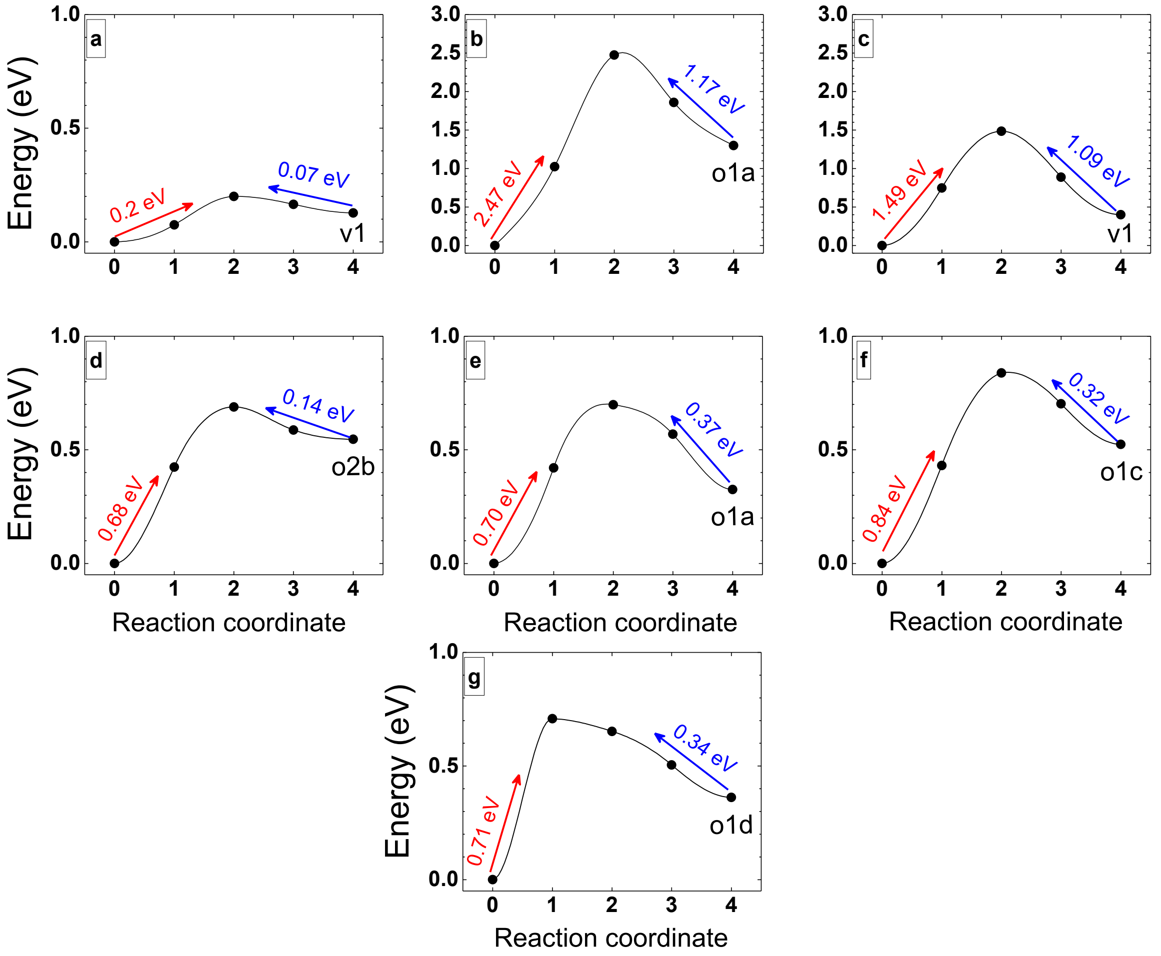

Fig. 4.2: Migration barriers for a He jump from the cluster center to a site at the cluster-iron interface to an interfacial vacant site (IVS) (a), to an interfacial interstitial site (IIS) of the CL O-Y cluster (b) and to an IVS (c) as well as to different IIS (d-g) of the CL O-Y-Ti cluster. The lines are drawn to guide the eye. In the calculations of the barriers the relaxed He positions at the center, on IVS, and on IIS are used. The denotations in the right part of the figures concern the He positions before relaxation (see Fig. 4.1). The corresponding relaxed configurations are discussed and shown in section 4.4 and in the Appendix-B *[App-B]*, respectively.

from a vacancy that belongs to the cluster and is situated on the face with 3 Ti atoms on corners (see also Appendix-B *[App-B]*). In clusters without Ti the interaction with the corresponding v in the cluster is weaker. On site B where the v is bound stronger. From literature it known that in pure Fe a vacancy attracts oxygen strongly (see e.g. [79]) This may be also the reason why on site C the attraction of v is higher than on site B since there are two oxygen atoms in the environment of v. However, not only the O-v interaction is responsible for the value of binding energy but also the other constituents as well as the particular atomic structure of the clusters. Finally, it should be noticed that there are also other non-equivalent sites for v in the vicinity of the cluster which were not studied in this work.

Table 4.1: Binding (incorporation) energy of a vacancy inserted on sites A, B, and C near the cluster models depicted in Fig. 4.1.

v site	**CL-OY** **Fig. 4.1 (a)**	**OC-OY** **Fig. 4.1 (b)**	**CL-OYTi** **Fig. 4.1 (c)**	**OC-OYTi** **Fig. 4.1 (d)**
A	-0.076 (2.09)	-0.012 (2.16)	-0.24 (1.93)	-0.16 (2.00)
B	-0.79 (1.38)	-1.06 (1.11)	-0.40 (1.77)	-0.98 (1.19)
C	-1.99 (0.18)	-1.97 (0.20)	-1.85 (0.32)	-1.73 (0.43)

4.10 Relaxed cluster configurations with one additional self-interstitial atom

It is well known from literature that in bcc Fe the most stable self-interstitial atom (SIA) configuration is the <110> dumbbell *[94, 95]*. In this work the value of 3.91 eV was obtained for the SIA formation or incorporation energy with a distance of 1.93 Å between both atoms of the dumbbell. This agrees well with results of other authors *[94]*. In order to assess the interaction of the clusters with a SIA the dumbbell was put, with a certain orientation, on three selected bcc sites in the iron matrix near the cluster. The atomic configurations before and after relaxation are shown in the Appendix-B *[App-B]*. The data on energetics are given in Table 4.2.

In the first case a dumbbell with [110] orientation is placed on the iron site A with a first neighbor distance to an IVS of the cluster, and with about equal distance to the 3 Y atoms on the corners of the corresponding octahedron face. For each of the cluster structures depicted in Fig. 4.1 minimization of total energy of the supercell (relaxation) leads to recombination of the SIA with the vacancy on the IVS. That means that one Fe atom of the dumbbell moves to the IVS, the other to the bcc site of the original SIA. The basic atomic configuration of the cluster does not change during the recombination process. The corresponding binding (incorporation) energies of the SIA are given in Table 4.2. Furthermore, a SIA is inserted with [101] orientation on the iron site B having about a first neighbor distance to one oxygen atom, and equal distance to the 2 Y atoms on the corners of the corresponding octahedron edge. Relaxation alters the structure of the clusters significantly so that the original CL or OC pattern is more or less lost, with exception of the OC cluster without Ti. This strong structural change is presumably due to the small size of the clusters. The oxygen atom initially situated closest to the SIA is pushed away and one atom of the dumbbell is shifted towards the vacant site of the underlying bcc lattice that had initially assigned to the pushed oxygen. The other Fe atom occupies the original bcc site of the dumbbell. In dependence on the final position of the pushed O atom the binding (incorporation) energy of the SIA varies. A particularly high absolute value of the SIA binding energy is found for the significantly altered structures. In these cases the SIA incorporation energy is negative or close to zero, which is further evidence that initial cluster configuration becomes unstable during interaction with the SIA (cf. Brodrick et al. *[54]*). The OC cluster of Fig. 4.1 (b) is only slightly altered by the addition of the SIA, and here attraction is much lower than in the case where the SIA is placed on site A. In the third case a dumbbell with [10-1] orientation is put on the iron site C with about a first neighbor distance to two adjacent O atoms, and equal distance to the 2 Y atoms on the corners of the corresponding octahedron edge. Again, except for OC cluster without Ti [Fig. 4.1 (b)] the relaxation of the supercell leads to changed cluster configurations and almost to a loss of the original CL or OC structure. One of the O atoms is shifted towards the cluster center and also the positions of the other atoms change. One Fe atom of the dumbbell is displaced to the vacant site of the underlying bcc lattice that had initially assigned to the pushed oxygen. The other is shifted to the initial site of the dumbbell. In the case of Fig. 4.1 (b) the binding energy of the SIA is in the same order of magnitude as that obtained for placing the SIA on site B.

Table 4.2: Binding (incorporation) energy of a SIA inserted (with a certain orientation of the dumbbell) on sites A, B, and C near the cluster models depicted in Fig. 4.1.

SIA site and orientation	CL-OY Fig. 4.1 (a)	OC-OY Fig. 4.1 (b)	CL-OYTi Fig. 4.1 (c)	OC-OYTi Fig. 4.1 (d)
A [110]	-3.50 (0.42)	-3.70 (0.22)	-3.41 (0.51)	-3.55 (0.36)
B [101]	-4.19 (-0.27)	-2.08 (1.84)	-3.89 (0.029)	-4.21 (-0.30)
C [10-1]	-2.98 (0.94)	-1.91 (2.00)	-3.58 (0.33)	-3.98 (-0.061)

The above results show that there is a strong attraction between a SIA and the cluster structures under consideration. This is mainly due to the availability of open volume or vacant sites. Due to recombination the initial SIA disappears, together with a part of the open volume. However, the relaxed cluster structures are still relatively open, so that they can certainly trap a few additional SIA until saturation is reached. Since the studied cluster configurations are small strong modifications of their structure are often observed. This will be certainly not happen for larger clusters. Nevertheless the present study unambiguously demonstrates that SIA can be trapped and annihilated by O-Y and O-Y-Ti clusters in bcc Fe. This is also in qualitative agreement with results of Brodrick et al. *[54]* who found that an interface between Y_2O_3 and bcc Fe can act as trap for SIA.

4.11 Summary

DFT calculations were performed in order to study the interaction of O-Y and O-Y-Ti clusters embedded in bcc Fe with He atoms, vacancies (v) and self-interstitial atoms (SIA). He in the center of a cage-like (CL) cluster is more stable than on an interfacial vacant site (IVS) at the cluster-Fe interface. Due to the small size of the investigated clusters the incorporation energy at the center site is higher than at the corresponding site in the bulk oxides Y_2O_3 or

$Y_2Ti_2O_7$. In CL O-Y clusters He on an IVS is more stable than in the configuration with oxygen in the center (OC), whereas there is no significant difference between the two kinds for clusters with Ti. Within a distance of $1.5\,a$ from the cluster center, He is not stable on most of the possible octahedral and tetrahedral interstitial sites of the underlying bcc Fe near the cluster-Fe interface. Instead, He is strongly attracted by each of the four different cluster structures and is shifted towards positions closer to the cluster. Relaxation to the known IVS as well as to previously unknown interfacial interstitial sites (IIS) is observed. He on such IIS is often less stable than on IVS but in few cases the opposite was found. Adding two or three He atoms to the environment of a cluster yields binding and incorporation energies that are nearly equal to the sum of the values obtained for the interaction with a single He atom. On the other hand, placing He dimers or trimers in the environment of a vacancy may also lead to relatively high (low) absolute values of the binding (incorporation) energy. All these results clearly show the high He storage/trapping capability of the clusters. Despite the comprehensive investigations performed in this work it is obvious that there are still other possible configurations, since the potential energy landscape is very complex, in particular in and near the clusters with Ti. Moreover, jumping barriers of He between the cluster-iron interface and the center of the CL clusters were determined. Due to the low incorporation energy on the center site the barrier for the jump to this position is lower than that for the backward jump. In the CL O-Y cluster the values of both barriers are lower than in the CL O-Y-Ti cluster, i.e. trapping and release of He is easier in the former than in the latter.

The interaction of an additional vacancy (v) with the different cluster structures is attractive but depends strongly on the site of v. The environment of oxygen atoms leads to strongest attraction which is consistent with the high absolute value of the binding energy of an oxygen-vacancy pair in pure bcc Fe. The recombination of SIA with nearby vacancy shows that the cluster is not only a trap for the v but also for the SIA

The results of the present work confirm findings of few previous theoretical investigations that O-Y and O-Y-Ti clusters embedded in bcc Fe are efficient traps for radiation defects. This is in agreement with experimental observation. New aspects concern results of our detailed studies on the influence of different cluster structures (CL and OC) and the calculation of He jump barriers. The role of open volume regions for He storage was highlighted and combined with a qualitative discussion on the basis of the electron structure of bcc Fe and the oxides Y_2O_3 or $Y_2Ti_2O_7$.

X ------------------------------- X

5. Conclusions and outlook

The focus of this thesis work has been on two main topics:

- Investigation of different structural models for atomic clusters in bcc Fe with the constituents O, vacancies, Y, and Ti
- Investigation of the interaction of the above mentioned clusters with He, vacancies (v) and self-interstitial atoms (SIA)

Density Functional Theory (DFT) calculations have been performed in order to obtain results regarding ground-state energetics and atomic configurations for the various supercells considered. Due to limitations of computational resources only small clusters with dimensions below 1 nm could be treated. This size is still too low for a simultaneous determination of atomic structure and composition by advanced experimental methods. These small clusters may be considered as nuclei for further structural evolution and growth. Within the further evolution process there may be a selection of favored structures, and if the clusters reach a size of some nm they can be unambiguously identified by experimental analysis. Nevertheless the present work yields a number of important contributions concerning structure and energetics of the small clusters and regarding their He storage capacity and their affinity to v and SIA.

The following structural models for the clusters have been considered:

- Structure Matching (SM) model: The cluster consists of a part of the unit cell of the native oxides Y_2O_3 or $Y_2Ti_2O_7$ and the corresponding <100> planes are parallel to the <100> planes of bcc Fe.
- Point Defect (PD) model: v, Y, and Ti are placed on bcc lattice sites and O is put on the octahedral interstitial sites of bcc Fe. The geometrical arrangement of the atoms is set as similar as possible to the SM model.
- All Substitutional (AS) model: O, v, Y, and Ti are placed on bcc sites, and the geometrical form is as similar as possible to the SM model.

- Due to the structure of the native oxides Y_2O_3 and $Y_2Ti_2O_7$, clusters within the SM, PD, and AS models have a form like an octahedron with an empty site in the center. They are therefore called cage-like (CL) clusters. Three other structural models can be derived by placing one of the O atoms into the center. These models are called O-in-center (OC) models.

The six cluster models have been investigated by DFT for identical compositions of O, v, Y, and Ti and the following results have been obtained:

- The most important finding consists in the statement that the data on the stability or energetics of the relaxed clusters are comparable although their atomic configurations are often different. This contradicts the prevailing opinion in the related theoretical literature that favors the SM-CL model.
- In all studied cases the absolute value of the total binding energy per cluster constituent becomes lower if Y is partially replaced by Ti, i.e. the driving force for the growth of O-Y clusters is higher than that of O-Y-Ti clusters. This may be correlated with the experimental observation that the presence of Ti leads to a reduction of the size of the oxide clusters in nanostructured ferritic alloys and to a higher dispersion.
- A further major result is the finding that CL clusters and OC-clusters have a similar total binding energy. If Ti is not present such clusters are slightly more stable than the corresponding CL clusters. The opposite holds for clusters with Ti. It is also shown that adding O atoms to CL cluster leads to structures with O in the center.
- OC-type clusters can be considered as nuclei for nanoclusters with rock-salt structure. Such a structure was also discussed in the literature, based on the analysis of experimental data. However, the presently prevailing opinion is that most of the observed several nanometer-sized clusters are near-stoichiometric CL structures.
- The transformation between CL- and OC-type cluster occurs by a jump of an oxygen atom to or from the cluster center. For SM clusters without Y the barrier for the jump to the center is rather low while that for the reverse jump is high. The opposite is the case for clusters with Ti.

- The application of the rigid lattice model (RLM), with bcc lattice sites for v, Y, and Ti, and octahedral interstitial sites for O and with DFT-based pair and triple interaction parameters, to the PD and PD-OC cluster model yields data for cluster energetics that agree well with the DFT results of this work.
- Vacancies are an important factor in stabilizing the cluster due to the very strong binding with O. We infer that the Ov pair may be the origin for cluster nucleation growth.

The interaction of clusters with He, v, and SIA has been studied using relaxed SM-CL and SM-OC clusters with two compositions. In the first case the cluster contains 6O, 9v, and 6Y, in the second 7O, 9v, 3Y, and 3Ti.

He is placed on following positions:

- One He on a vacancy site in the center of a CL cluster. This position corresponds to an octahedral interstitial site in bulk Y_2O_3 or $Y_2Ti_2O_7$.
- One He on a vacancy site at the cluster-iron interface: Both in CL and OC clusters vacant bcc sites, which are not assigned to oxygen atoms are available there.
- One He on interstitial sites: In the interface region He might occupy tetrahedral and octahedral interstitial sites of the underlying bcc lattice. The investigations were limited to such interstitial sites with a distance of less or equal than 1.5 times the lattice constant of bcc Fe.
- Furthermore, two or three He atoms are placed on some of the above-mentioned sites, and on some other positions.

Three bcc lattice sites are chosen for adding v or SIA.

The following results of DFT calculations clearly show the high He storage/trapping capability of the clusters. The main reason is the low electron density in the empty regions of the oxide-like structure of the cluster. Such regions are not available in iron due to its non-localized valence electrons.

- He in the center of a CL cluster is more stable than on an interfacial vacant site (IVS) at the cluster-Fe interface.
- In CL clusters without Ti, He on an IVS is more stable than in the cluster configuration with oxygen in the center (OC), whereas there is no significant difference between the two kinds for clusters with Ti.
- Within a distance of 1.5 times the lattice constant of bcc Fe from the cluster center, He is not stable on most of the possible octahedral and tetrahedral interstitial sites of the underlying bcc Fe. Instead, He is strongly attracted by the cluster structures and is shifted towards positions closer to the cluster. Relaxation to the known IVS as well as to previously unknown interfacial interstitial sites (IIS) is observed. He on such IIS is often less stable than on IVS. Away from cluster, the He behavior is similar as in bulk bcc Fe.
- If two or three He atoms are inserted the corresponding binding and incorporation energies are nearly equal to the sum of the values obtained for the interaction with a single He atom. Placing He dimers or trimers in the environment of a vacancy may even lead to relatively high (low) absolute values of the binding (incorporation) energy.
- The jump barriers for He between certain sites at the rim and the center of CL clusters are lower for clusters without Ti than in those with Ti. That means that trapping and release of He is easier in the former than in the latter.

Furthermore, DFT studies revealed that the interaction of a v with a cluster strongly depends on the v site. The environment of oxygen atoms leads to strongest attraction, which is consistent with the high absolute value of the binding energy of an Ov pair in bulk bcc Fe. The recombination of SIA with nearby vacancy shows the cluster acts not only as trap for the v but also for the SIA.

In order to increase our knowledge on the properties of O-Y and O-Y-Ti nanoclusters in iron alloys further research should be performed on the following topics:

- More DFT results on clusters with other interface orientation and stoichiometry would be desirable.
- Future work is required to investigate the evolution and growth of the different, but equivalent cluster structures that were discussed in this work. In particular this concerns the search for selection rules that enable the formation of the larger, nanometer-size clusters found in experiment. For this purpose the availability of a sufficiently precise interatomic potential for the Fe-O–Y–Ti –He system would be highly desirable. The DFT data presented in this work can be used in the development of potentials. The use of such potentials would allow for the treatment of larger simulation cells than it is possible for DFT investigations and the application of methods like molecular dynamics and Monte Carlo simulations. As shown in this work, the use of a rigid lattice model with DFT-based interaction parameters can be helpful for an approximate description of the clusters. Therefore, this method may be further improved and employed in future lattice Monte Carlo simulations.
- Also the consideration of the free binding energy of the clusters instead of the ground-state binding energy would lead to more insight in the issue of cluster evolution. For this purpose, mainly the phonon contributions to free energy must be considered.
- Experimentally, it is very important to clarify unambiguously whether after mechanical alloying O, Y, and Ti are really completely dissolved in the iron-based matrix. If there were still remaining nuclei of yttria, the CL cluster structures might be favored from the very beginning of the process of NFA formation.
- Theoretical work is required to investigate the trapping capabilities of more different kinds of oxide clusters, e.g. those with higher oxygen content, and to determine more migration barriers for He, v, or SIA in the environment of the clusters.

X ------------------------------ X

Reference

[1] Locatelli G, Mancini M and Todeschini N, Generation IV nuclear reactors: Current status and future prospects *Energy Policy* **61** (2013) 1503. *doi:https://doi.org/10.1016/j.enpol.2013.06.101*

[2] Murty L K and Charit I, An Introduction to Nuclear Materials - Fundamentals and Applications *Wiley-VCH Verlag GmbH & Co. KGaA*

[3] Olander D R, Fundamental aspects of nuclear reactor fuel elements. OSTI ID: 7343826, TID-26711-P1 (1976) *doi:https://doi.org/10.2172/7343826*

[4] Was G S, Fundamentals of Radiation Materials Science *New York: Springer-Verlag* (2007) *doi:https://doi.org/10.1007/978-3-540-49472-0*

[5] Odette G R, Alinger M J and Wirth B D, Recent Developments in Irradiation-Resistant Steels *Annu. Rev. Mater. Res.* **38** (2008) 471. *doi:https://doi.org/10.1146/annurev.matsci.38.060407.130315*

[6] ZinkleJeremy S J and Busby T, Structural materials for fission & fusion energy *Mater. Today* **12** (2009) 12. *doi:https://doi.org/10.1016/S1369-7021(09)70294-9*

[7] Zinkle S J and Was G S, Materials challenges in nuclear energy *Acta Mater.* **61** (2013) 735. *doi:https://doi.org/10.1016/j.actamat.2012.11.004*

[8] Zinkle S J, Fusion materials science: Overview of challenges and recent progress *Phys. Plasmas* **12** (2005) 058101. *doi:https://doi.org/10.1063/1.1880013*

[9] Samara M, Multiscale Modelling: the role of helium in iron *Mater. Today* **12** (2009) 46. *doi:https://doi.org/10.1016/S1369-7021(09)70298-6*

[10] Dai Y, Odette G R and Yamamoto T, The Effects of Helium in Irradiated Structural Alloys *In Comprehensive Nuclear Materials; Elsevier Science: Amsterdam, The Netherlands, 2012; pp. 141–193* (2012) *doi:https://doi.org/10.1016/b978-0-08-056033-5.00006-9*

[11] Bloom E E, Zinkle S J and Wiffen F W, Materials to deliver the promise of fusion power – progress and challenges *J. Nucl. Mater.* **329-333** (2004) 12. *doi:https://doi.org/10.1016/j.jnucmat.2004.04.141*

[12] Little E A, Development of radiation resistant materials for advanced nuclear power plant *Mater. Sci. Technol.* **22** (2013) 491. *doi:https://doi.org/10.1179/174328406x90998*

[13] Mansur L K, Rowcliffe A F, Nanstad R K, Zinkle S J, Corwin W R and Stoller R E, Materials needs for fusion, Generation IV fission reactors and spallation neutron sources – similarities and differences *J. Nucl. Mater.* **329-333** (2004) 166. *doi:https://doi.org/10.1016/j.jnucmat.2004.04.016*

[14] Klueh R L, Ehrlich K and Abe F, Ferritic/Martensitic steels:promises and problems *J. Nucl. Mater.* **191-194** (1992) 116. *doi:https://doi.org/10.1016/S0022-3115(09)80018-4*

[15] Raj B and Jayakumar T, Development of Reduced Activation Ferritic–Martensitic Steels and fabrication technologies for Indian test blanket module *Journal of Nuclear Materials* **417** (2011) 72. *doi:https://doi.org/10.1016/j.jnucmat.2011.02.032*

[16] Tan L, Snead L L and Katoh Y, Development of new generation reduced activation ferritic-martensitic steels for advanced fusion reactors *J. Nucl. Mater.* **478** (2016) 42. *doi:https://doi.org/10.1016/j.jnucmat.2016.05.037*

[17] Fischer J, Dispersion strengthened ferritic alloy for use in liquid-metal fast breeder reactors (LMFBRS). Patent File Date: Filed date 5 Feb 1976, 1978. p.Medium: X; Size: Pages: 10 *doi:http://inis.iaea.org/search/search.aspx?orig_q=RN:09394580*

[18] Charit I and Murty K L, Strucutral Materials issues for the next generation Fission Reactor *JOM* **62** (2010) 67. *doi:https://doi.org/10.1007/s11837-010-0142-3*

[19] Klueh R L, Shingledecker J P, Swindeman R W and Hoelzer D T, Oxide dispersion-strengthened steels: A comparison of some commercial and experimental alloys *J. Nucl. Mater.* **341** (2005) 103. *doi:https://doi.org/10.1016/j.jnucmat.2005.01.017*

[20] Odette G R and Hoelzer D T, Irradiation-tolerant nanostrucutred ferritic alloys:Transforming Helium from a Liability to an asset *JOM* **62** (2010) 84. *doi:https://doi.org/10.1007/s11837-010-0144-1*

[21] Odette G R, Recent Progress in Developing and Qualifying Nanostructured Ferritic Alloys for Advanced Fission and Fusion Applications *JOM* **66** (2014) 2427. *doi:https://doi.org/10.1007/s11837-014-1207-5*

[22] Zinkle S J, Boutard J L, Hoelzer D T, Kimura A, Lindau R, Odette G R, Rieth M, Tan L and Tanigawa H, Development of next generation tempered and ODS reduced activation ferritic/martensitic steels for fusion energy applications *Nucl. Fusion* **57** (2017) 092005. *doi:https://doi.org/10.1088/1741-4326/57/9/092005*

[23] Cunningham N, Wu Y, Klingensmith D and Odette G R, On the remarkable thermal stability of nanostructured ferritic alloys *Mater. Sci. & Engin. A* **613** (2014) 296. *doi:https://doi.org/10.1016/j.msea.2014.06.097*

[24] Alinger M J, Odette G R and Hoelzer D T, On the role of alloy composition and processing parameters in nanocluster formation and dispersion strengthening in nanostuctured ferritic alloys *Acta Mater.* **57** (2009) 392. *doi:https://doi.org/10.1016/j.actamat.2008.09.025*

[25] Ressel G, Parz P, Primig S, Leitner H, Clemens H and Puff W, New findings on the atomistic mechanisms active during mechanical milling of a Fe-Y2O3 model alloy *J. Appl. Phys.* **115** (2014) 124313. *doi:https://doi.org/10.1063/1.4869787*

[26] Messina L, Nastar M, Sandberg N and P.Olsson, Systematic electronic-structure investigation of substitutional impurity diffusion and flux coupling in bcc iron *Phys. Rev. B* **93** (2016) 184302. *doi:https://doi.org/10.1103/PhysRevB.93.184302*

[27] Mock M and K.Albe, Diffusion of yttrium in bcc-iron studied by kinetic Monte Carlo simulations *J. Nucl. Mater.* **494** (2017) 157. *doi:https://doi.org/10.1016/j.jnucmat.2017.07.021*

[28] Wharry J P, Swenson M J and Yano K H, A review of the irradiation evolution of dispersed oxide nanoparticles in the b.c.c. Fe-Cr system: Current understanding and future directions *J Nuc. Mater.* **486** (2017) 11. *doi:http://doi.org/10.1016/j.jnucmat.2017.01.009*

[29] Zhang Z W, Yao L, Wan X-L and Miller M K, Vacancy-controlled ultrastable nanoclusters in nanostructured ferritic alloys *Sci Rep.* **5** (2015) 10600.

doi:https://doi.org/10.1038/srep10600

[30] Odette G R, On the status and prospects for nanostructured ferritic alloys for nuclear fission and fusion application with emphasis on the underlying science *J. Nucl. Mater.* **143** (2018) 142. *doi:https://doi.org/10.1016/j.scriptamat.2017.06.021*

[31] Sakasegawa H, Legendre F, Boulanger L, Brocq M, Chaffron L, Cozzika T, Malaplate J, Henry J and de Carlan Y, Stability of non-stoichiometric clusters in the MA957 ODS ferrtic alloy *J. Nucl. Mater.* **417** (2011) 229. *doi:https://doi.org/10.1016/j.jnucmat.2010.12.056*

[32] London A J, Santra S, Amirthapandian S, Panigrahi B K, Sarguna R M, Balaji S, Vijay R, Sundar C S, Lozano-Perez S and Grovenor C R M, Effect of Ti and Cr on dispersion, structure and composition of oxide nano-particles in model ODS alloys *Acta Mater.* **97** (2015) 223. *doi:https://doi.org/10.1016/j.actamat.2015.06.032*

[33] Edmondson P D, Parish C M, Zhang Y, Hallén A and Miller M K, Helium bubble distributions in a nanostructured ferritic alloy *J. Nucl. Mater.* **434** (2013) 210. *doi:https://doi.org/10.1016/j.jnucmat.2012.11.049*

[34] Duan B, Heintze C, Bergner F, Ulbricht A, Akhmadaliev S, Oñorbe E, de Carlan Y and Wang T, The effect of the initial microstructure in terms of sink strength on the ion-irradiation-induced hardening of ODS alloys studied by nanoindentation *J. Nucl. Mater.* **495** (2017) 118. *doi:https://doi.org/10.1016/j.jnucmat.2017.08.014*

[35] Barnard L, Odette G R, Szlufarska I and Morgan D, An ab initio study of Ti–Y–O nanocluster energetics in nanostructured ferritic alloys *Acta Mater.* **60** (2012) 935. *doi:https://doi.org/10.1016/j.actamat.2011.11.011*

[36] Barnard L, Cunningham N, Odette G R, Szlufarska I and Morgan D, Thermodynamic and kinetic modeling of oxide precipitation in nanostructured ferritic alloys *Acta Mater.* **91** (2015) 340. *doi:https://doi.org/10.1016/j.actamat.2015.03.014*

[37] Jiang Y, Smith J R and Odette G R, Formation of Y-Ti-O nanoclusters in nanostructured ferritic alloys: A first-principles study *Phys. Rev. B* **79** (2009) 064103. *doi:https://doi.org/10.1103/PhysRevB.79.064103*

[38] Murali D, Panigrahi B K, Valsakumar M C, Chandra S, Sundar C S and Raj B, The role of minor alloying elements on the stability and dispersion of yttria nanoclusters in nanostructured ferritic alloys: An ab initio study *J. Nucl. Mater.* **403** (2010) 113. *doi:https://doi.org/10.1016/j.jnucmat.2010.06.008*

[39] Murali D, Posselt M and Schiwarth M, First-principles calculation of defect free energies: General aspects illustrated in the case of bcc Fe *Phys. Rev. B* **92** (2015) 064103. *doi:https://doi.org/10.1103/PhysRevB.92.064103*

[40] Posselt M, Murali D and Panigrahi B K, Energetics, structure and composition of nanoclusters in oxide dispersion strengthened Fe–Cr alloys *Modell. Simul. Mater. Sci. Eng.* **22** (2014) 085003. *doi:https://doi.org/10.1088/0965-0393/22/8/085003*

[41] Qian Q, Wang Y, Jiang Y, He C and Hu T, Nucleation of Y-X-O (X=Al, Ti, or Zr) NCs in nano-structured ferritic alloys: A first principles comparative study *J. Nucl. Mater.* **518** (2019) 140. *doi:10.1016/j.jnucmat.2019.02.051*

[42] Claisse A and Olsson P, First-principles calculations of (Y, Ti, O) cluster formation in body centred cubic iron-chromium *Nucl. Instrum. Methods Phys. Res., Sect. B* **303**

(2013) 18. *doi:https://doi.org/10.1016/j.nimb.2013.01.016*

[43] Higgins M P, Liu C Y, Lu Z, Shao L, Wang L M and Gao F, Crossover from disordered to core-shell structures of nano-oxide Y2O3 dispersed particles in Fe *Appl. Phys. Lett.* **109** (2016) 031911. *doi:https://doi.org/10.1063/1.4959776*

[44] Hirata A, Fujita T, Wen Y R, Schneibel J H, Liu C T and Chen M W, Atomic structure of nanoclusters in oxide-dispersion-strengthened steels *Nat. Mater.* **10** (2011) 922. *doi:https://doi.org/10.1038/nmat3150*

[45] Sun D, Li R, Ding J, Huang S, Zhang P, Lu Z and Zhao J, Helium behavior in oxide dispersion strengthened (ODS) steel: Insights from ab initio modeling *J. Nucl. Mater.* **499** (2018) 71. *doi:https://doi.org/10.1016/j.jnucmat.2017.10.073*

[46] Danielson T and Hin C, Structural and electronic effects of helium interstitials in Y2Ti2O7: A first-principles study *J. Nucl. Mater.* **452** (2014) 189. *doi:https://doi.org/10.1016/j.jnucmat.2014.05.016*

[47] Danielson T, Tea E and Hin C, Ab initio investigation of helium in Y2Ti2O7 : Mobility and effects on mechanical properties *J. Nucl. Mater.* **477** (2016) 7. *doi:https://doi.org/10.1016/j.jnucmat.2016.05.024*

[48] Danielson T, Tea E and Hin C, First-principles investigation of helium in Y2O3 *J. Phys. D: Appl. Phys.* **49** (2016) 065301. *doi:https://doi.org/10.1088/0022-3727/49/6/065301*

[49] Erhart P, A first-principles study of helium storage in oxides and at oxide–iron interfaces *J. Appl. Phys.* **111** (2012) 113502. *doi:https://doi.org/10.1063/1.4707944*

[50] Jin Y, Jiang Y, Yang L, Lan G, Robert Odette G, Yamamoto T, Shang J and Dang Y, First principles assessment of helium trapping in Y2TiO5 in nano-featured ferritic alloys *J. Appl. Phys.* **116** (2014) 143501. *doi:https://doi.org/10.1063/1.4897503*

[51] Lai W, Ou Y, Lou X and Wang F, Ab initio study of He trapping, diffusion and clustering in Y2O3 *Nucl. Instrum. Methods Phys. Res. B* **393** (2017) 6. *doi:https://doi.org/10.1016/j.nimb.2016.11.026*

[52] Sun D, Zhang P, Ding J and Zhao J, He behavior in different oxide ODS steels: A comparative ab initio study *J. Nucl. Mater.* **507** (2018) 101. *doi:https://doi.org/10.1016/j.jnucmat.2018.04.048*

[53] Yang L, Jiang Y, Robert Odette G, Yamamoto T, Liu Z and Liu Y, Trapping helium in Y2Ti2O7 compared to in matrix iron: A first principles study *J. Appl. Phys.* **115** (2014) 143508. *doi:https://doi.org/10.1063/1.4871282*

[54] Brodrick J, Hepburn D J and Ackland G J, Mechanism for radiation damage resistance in yttrium oxide dispersion strengthened steels *J. Nucl. Mater.* **445** (2014) 291. *doi:https://doi.org/10.1016/j.jnucmat.2013.10.045*

[55] Peng M-M and Lai W-S, Interaction between vacancies and the α-Fe/Y2O3 interface: A first-principles study *Nucl. Instrum. Methods Phys. Res. B* **352** (2015) 67. *doi:https://doi.org/10.1016/j.nimb.2014.12.056*

[56] Yang L, Jiang Y, Wu Y, Odette G R, Zhou Z and Lu Z, The ferrite/oxide interface and helium management in nano-structured ferritic alloys from the first principles *Acta Mater.* **103** (2016) 474. *doi:https://doi.org/10.1016/j.actamat.2015.10.031*

[57] Gan Y, Zhao H, Hoelzer D T and Yun D, Energetic Study of Helium Cluster Nucleation and Growth in 14YWT through First Principles *Materials* **9** (2016) 1.

doi:https://doi.org/10.3390/ma9010017

[58] Danielson T, Tea E and Hin C, Investigation of helium at a Y2Ti2O7 nanocluster embedded in a BCC Fe matrix *Phys. Chem. Chem. Phys.* **18** (2016) 30128. *doi:https://doi.org/10.1039/c6cp05233a*

[59] Hohenberg P and Kohn W, Inhomogeneous Electron Gas *Phys. Rev. B* **136** (1964) B864. *doi:https://doi.org/10.1103/PhysRev.136.B864*

[60] Kohn W and Sham L J, Self-Consistent Equations Including Exchange and Correlation Effects *Phys. Rev.* **140** (1965) A1133. *doi:https://doi.org/10.1103/PhysRev.140.A1133*

[61] Kresse G and Hafner J, Ab initio molecular dynamics for liquid metals *Phys. Rev. B* **47** (1993) 558. *doi:https://doi.org/10.1103/PhysRevB.47.558*

[62] Vanderbilt D, Soft self-consistent pseudopotentials in a generalized eigenvalue formalism *Phys. Rev. B* **41** (1990) 7892. *doi:http://doi.org/10.1103/physrevb.41.7892*

[63] Blochl P E, Projector augmented-wave method *Phys. Rev. B* **50** (1994) 17953. *doi:https://doi.org/10.1103/physrevb.50.17953*

[64] Kresse G and Furthmüller J, Efficiency of ab-initio total energy calculations for metals and semiconductors using a plane-wave basis set *Comput. Mater. Sci.* **6** (1996) 15. *doi:https://doi.org/10.1016/0927-0256(96)00008-0*

[65] Martin M R, Electronic structure - Basic theory and practical methods *Cambridge University press* *doi:https://doi.org/10.1017/CBO9780511805769*

[66] Sholl D S and Steckel J A, Densty Functional Theory-A Practical Introduction *Wiley* *doi:https://doi.org/10.1002/9780470447710*

[67] Ceperley D M and Alder B J, Ground State of the Electron Gas by a Stochastic Method *Phys. Rev. Lett.* **45** (1980) 566. *doi:https://doi.org/10.1103/PhysRevLett.45.566*

[68] Perdew J P, Density-functional approximation for the correlation energy of the inhomogeneous electron gas *Phys. Rev. B* **33** (1986) 8822. *doi:https://doi.org/10.1103/physrevb.33.8822*

[69] Burke K, The ABC of DFT -(unpublished notes) (2007)

[70] Burke K and Wagner L O, DFT in a nutshell *Int. J Quantum Chem.* **113** (2013) 96. *doi:https://doi.org/10.1002/qua.24259*

[71] Perdew J P and Wang Y, Accurate and simple analytic representation of the electron-gas correlation energy *Phys. Rev. B* **45** (1992) 13244. *doi:https://doi.org/10.1103/physrevb.45.13244*

[72] Perdew J P, Chevary J A, Vosko S H, Jackson K A, Pederson M R, Singh D J and Fiolhais C, Atoms, molecules, solids, and surfaces: Applications of the generalized gradient approximation for exchange and correlation *Phys. Rev. B* **46** (1992) 6671. *doi:https://doi.org/10.1103/physrevb.46.6671*

[73] Perdew J P, Burke K and Ernzerhof M, Generalized Gradient Approximation Made Simple *Phys. Rev. Lett.* **77** (1996) 3865. *doi:https://doi.org/10.1103/PhysRevLett.77.3865*

[74] Monkhorst H J and Pack J D, Special points for Brillouin-zone integrations *Phys. Rev. B* **13** (1976) 5188. *doi:https://doi.org/10.1103/PhysRevB.13.5188*

[75] Methfessel M and Paxton A T, High-precision sampling for Brillouin-zone integration in metals *Phys. Rev. B* **40** (1989) 3616. *doi:https://doi.org/10.1103/PhysRevB.40.3616*

[76] Henkelman G and Jo´nsson H, Improved tangent estimate in the nudged elastic band method for finding minimum energy paths and saddle points *J. Chem. Phys.* **113** (2000) 9978. *doi:https://doi.org/10.1063/1.1323224*

[77] Jonsson H, Mills G and Jacobsen K W, Classical and Quantum Dynamics In Condensed Phase Simulations *(World Scientific, Singapore, 1998), pp. 389–404* (1998) *doi:https://doi.org/10.1142/3816*

[78] Henkelman G, Uberuaga P B and Jónsson H, A climbing image nudged elastic band method for finding saddle points and minimum energy paths *J. Chem. Phys.* **113** (2000) 9901. *doi:https://doi.org/10.1063/1.1329672*

[79] Posselt M, Importance of configurational contributions to the free energy of nanoclusters *AIP Adv* **3** (2013) 072137. *doi:https://doi.org/10.1063/1.4817590*

[80] Posselt M, Murali D and Schiwarth M, Influence of phonon and electron excitations on the free energy of defect clusters in solids: A first-principles study *Comput. Mater. Sci.* **127** (2017) 284. *doi:https://doi.org/10.1016/j.commatsci.2016.10.039*

[81] Fu C L, Krcmar M, Painter G S and Chen X-Q, Vacancy mechanism of high oxygen solubility and nucleation of stable oxygen-enriched clusters in Fe *Phys. Rev. Lett.* **99** (2007) 225502. *doi:https://doi.org/10.1103/PhysRevLett.99.225502*

[82] Kresse G and Furthmüller J, Efficient iterative schemes for ab initio total-energy calculations using a plane-wave basis set *Phys. Rev. B* **54** (1996) 11169. *doi:https://doi.org/10.1103/PhysRevB.54.11169*

[83] Kresse G and Joubert D, From ultrasoft pseudopotentials to the projector augmented-wave method *Phys. Rev. B* **59** (1999) 1758. *doi:https://doi.org/10.1103/PhysRevB.59.1758*

[84] See the SM for info (2020)

[85] Othen P J, Jenkins M L and Smith G D W, High-resolution electron microscopy studies of the structure of Cu precipitates in α-Fe *Philos. Mag. A* **70** (1994) 1. *doi:https://doi.org/10.1080/01418619408242533*

[86] Pizzini S, Roberts K J, Phythian W J, English C A and Greaves G N, A fluorescence EXAFS study of the structure of copper-rich precipitates in Fe–Cu and Fe–Cu–Ni alloys *Philos. Mag. Lett.* **61** (1990) 223. *doi:https://doi.org/10.1080/09500839008202362*

[87] Brocq M, Radiguet B, Breton J-M L, Cuvilly F, Pareige P and Legendre F, Nanoscale characterisation and clustering mechanism in an Fe–Y2O3 model ODS alloy processed by reactive ball milling and annealing *Acta Mater.* **58** (2010) 1806. *doi:https://doi.org/10.1016/j.actamat.2009.11.022*

[88] Brocq M, Radiguet B, Poissonnet S, Cuvilly F, Pareige P and Legendre F, Nanoscale characterization and formation mechanism of nanoclusters in an ODS steel elaborated by reactive-inspired ball-milling and annealing *J. Nucl. Mater.* **409** (2011) 80. *doi:https://doi.org/10.1016/j.jnucmat.2010.09.011*

[89] Hirata A, Fujita T, Liu C T and Chen M W, Characterization of oxide nanoprecipitates in an oxide dispersion strengthened 14YWT steel using aberration-corrected STEM *Acta Mater.* **60** (2012) 5686. *doi:https://doi.org/10.1016/j.actamat.2012.06.042*

[90] Kaminaga K, Sei R, Hayashi K, Happo N, Taijiri H, Oka D, Fukumura T and Hasegawa T, A divalent rare earth oxide semiconductor: Yttrium monoxide *Appl. Phys. Lett.* **108** (2016) 122102. *doi:https://doi.org/10.1063/1.4944330*

[91] Fu C-C and Willaime F, Ab initio study of helium in α−Fe: Dissolution, migration, and clustering with vacancies *Phys. Rev. B* **72** (2005) 064117. *doi:https://doi.org/10.1103/PhysRevB.72.064117*

[92] Seletskaia T, Osetsky Y, Stoller R E and Stocks G M, Magnetic interactions influence the properties of helium defects in iron *Phys. Rev. Lett.* **94** (2005) 046403. *doi:https://doi.org/10.1103/PhysRevLett.94.046403*

[93] Zhang P, Ding J, Sun D and Zhao J, First-principles study of noble gas atoms in bcc Fe *J. Nucl. Mater.* **492** (2017) 134. *doi:https://doi.org/10.1016/j.jnucmat.2017.05.022*

[94] Domain C and Becquart C S, Ab initio calculations of defects in Fe and dilute Fe-Cu alloys *Phys. Rev. B* **65** (2001) 1. *doi:https://doi.org/10.1103/PhysRevB.65.024103*

[95] Dudarev S L, Density Functional Theory Models for Radiation Damage *Annu. Rev. Mater. Res.* **43** (2013) 35. *doi:https://doi.org/10.1146/annurev-matsci-071312-121626*

X ------------------------------ X

Appendix-A

Summary of all details related to chapter 3:

Cluster models and their relaxed configurations

Fig. A1: Illustration of the construction of the 6O9v6Y (a) and the 7O9v3Y3Ti (b) clusters within the framework of the Structure Matching (SM) model.

Cluster construction: structure matching Y-O

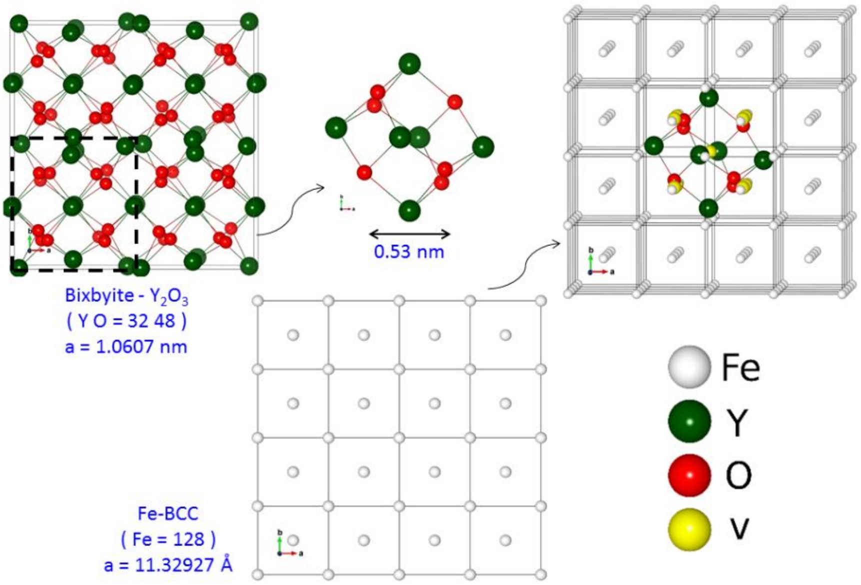

Cluster construction: structure matching Y-Ti-O cluster

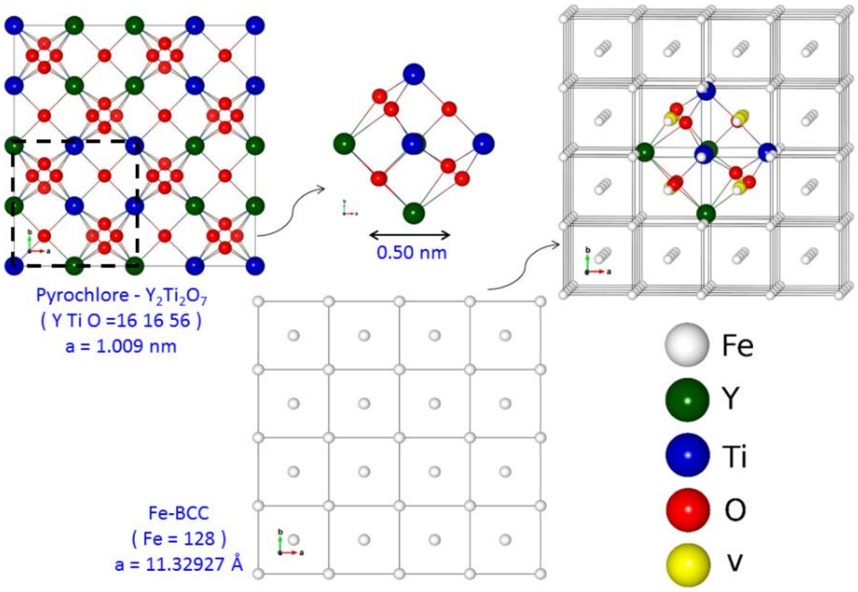

Fig. A2: Complete representation of the small clusters containing O, Y, and vacancies (v): SM, PD, and AS templates (cf. Fig. 3.1, chapter 3) used for the cluster construction (a), pictures of the clusters before (left) and after (right) relaxation (b-kk). Red, green, gray, and yellow spheres show O, Y, Fe atoms, and vacancies, respectively (b-kk). Fig. 3.3 (a) (chapter 3) shows the total binding energy of the relaxed clusters per cluster constituent (O,v,Y).

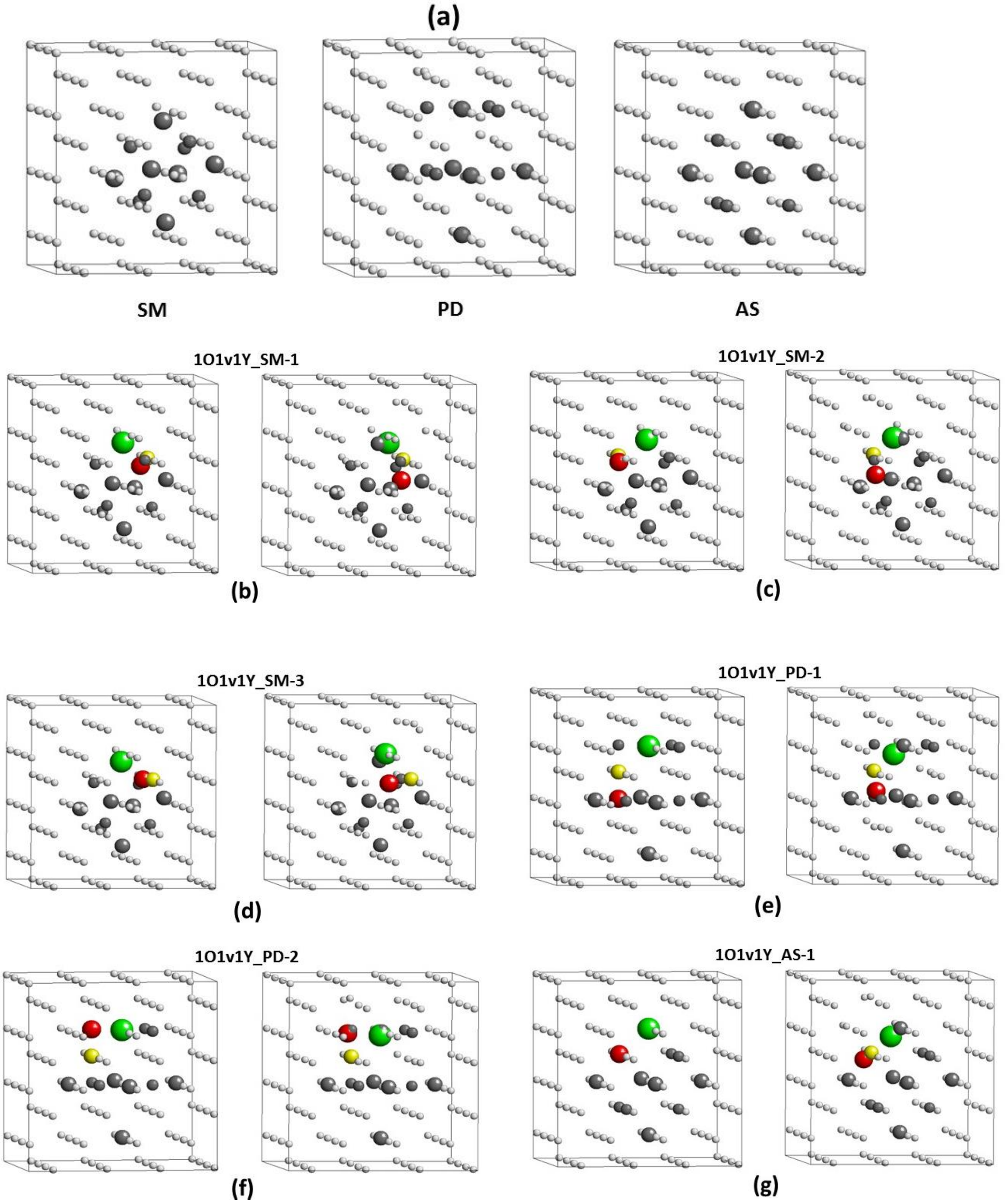

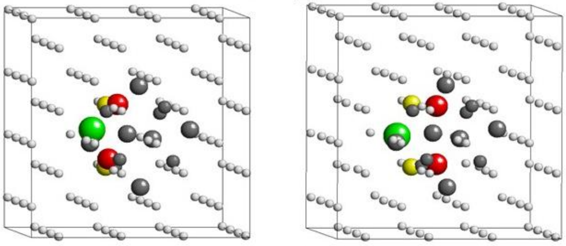

2O2v1Y_SM-1

(h)

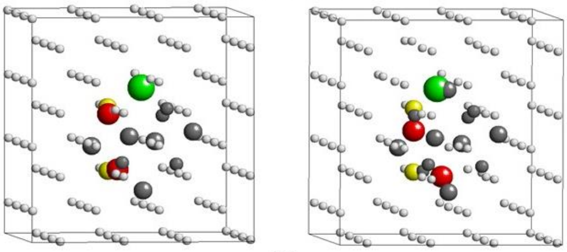

2O2v1Y_SM-2

(i)

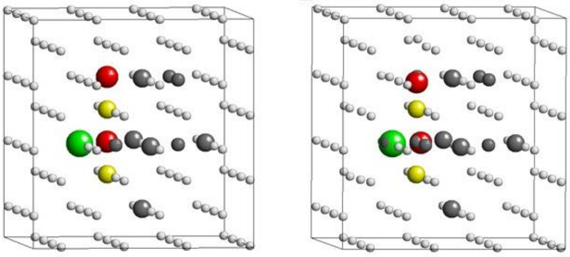

2O2v1Y_PD-1

(j)

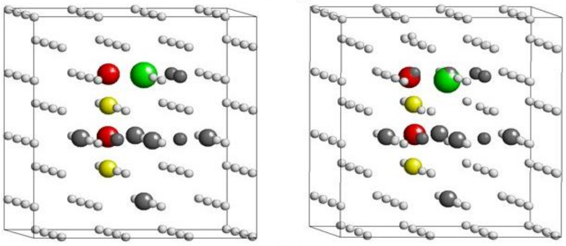

2O2v1Y_PD-2

(k)

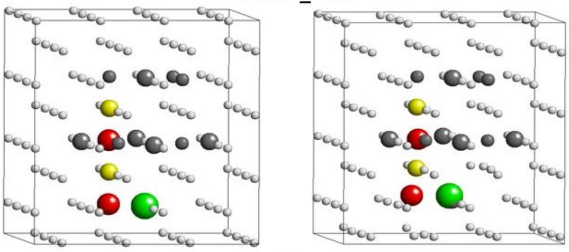

2O2v1Y_PD-3

(l)

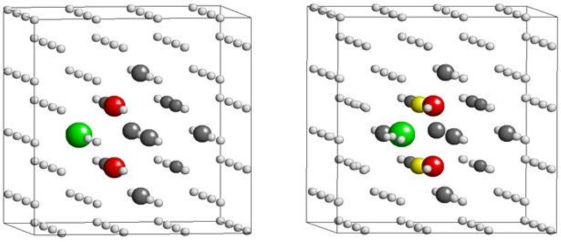

2O2v1Y_AS-1

(m)

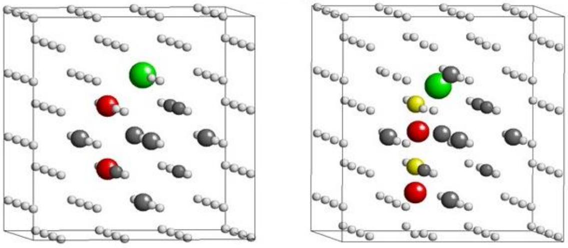

2O2v1Y_AS-2

(n)

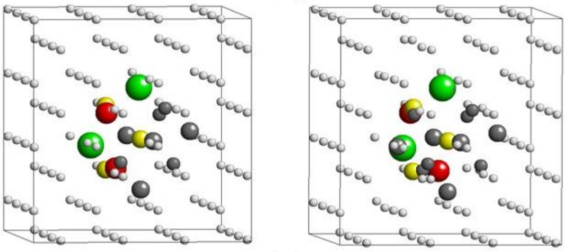

2O3v2Y_SM-1

(o)

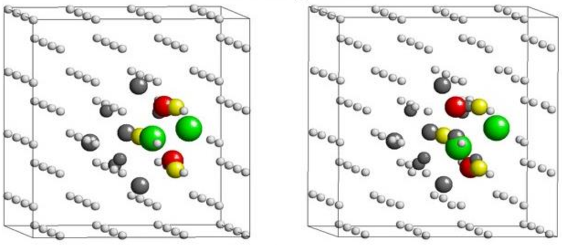

2O3v2Y_SM-2

(p)

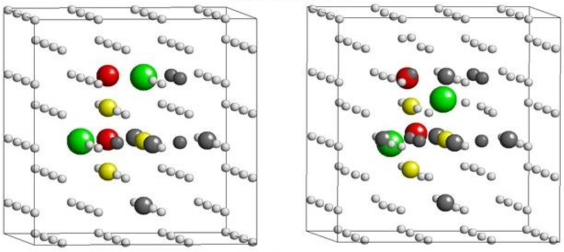

2O3v2Y_PD-1

(q)

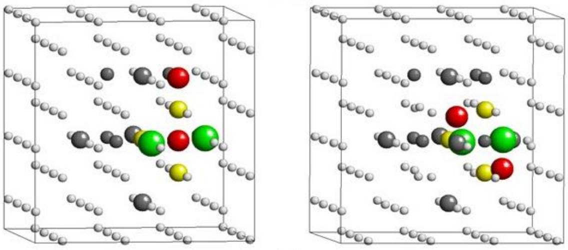

(r)

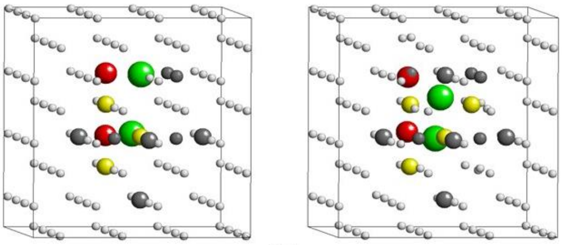

(s)

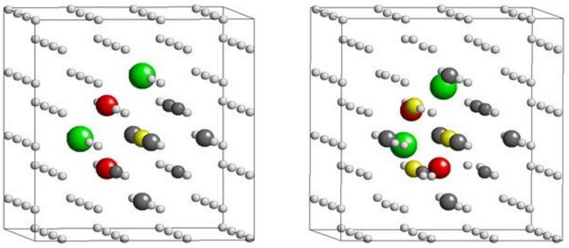

(t)

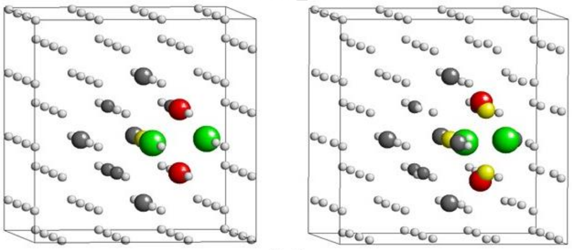

(u)

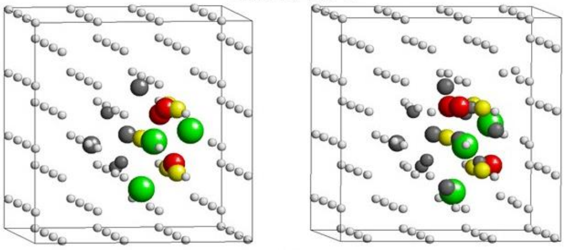

(v)

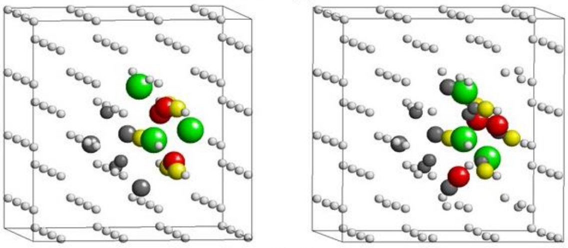

(w)

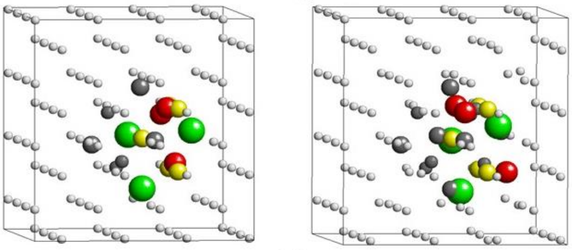

(x)

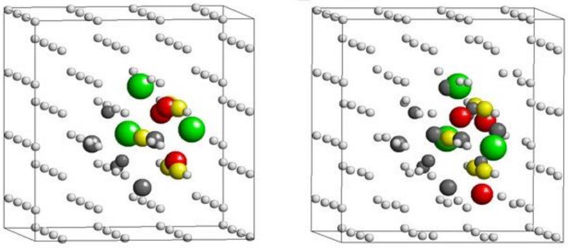

(y)

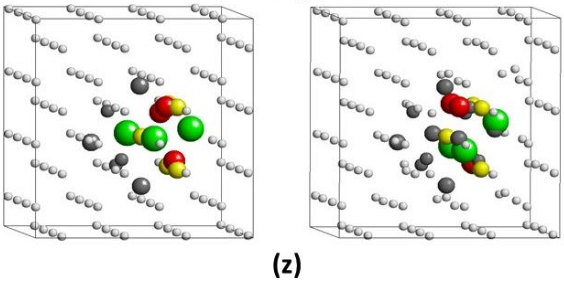

(z)

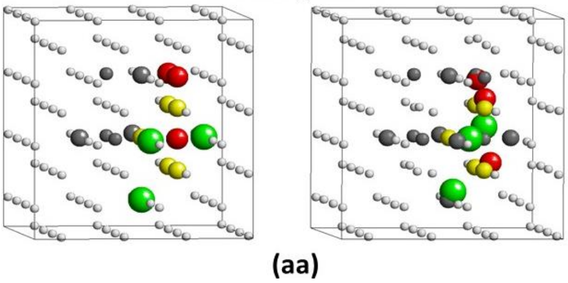

(aa)

3O5v3Y_PD-2

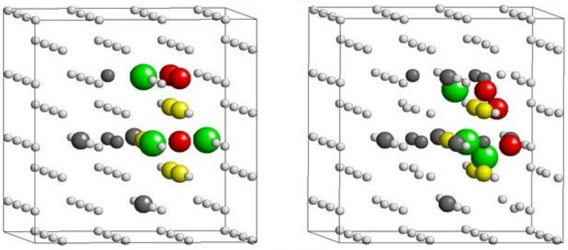

(bb)

3O5v3Y_PD-3

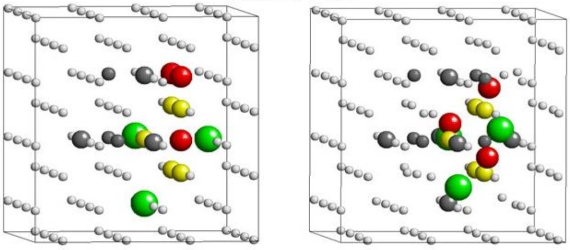

(cc)

3O5v3Y_PD-4

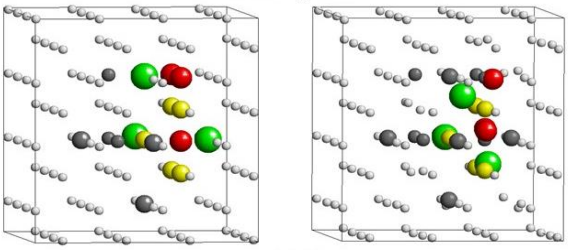

(dd)

3O5v3Y_PD-5

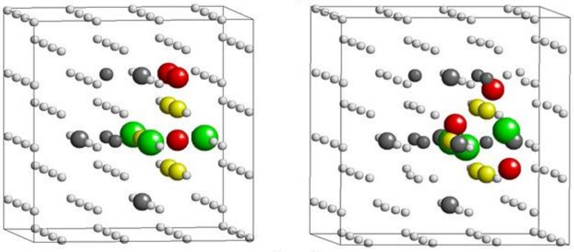

(ee)

3O5v3Y_AS-1

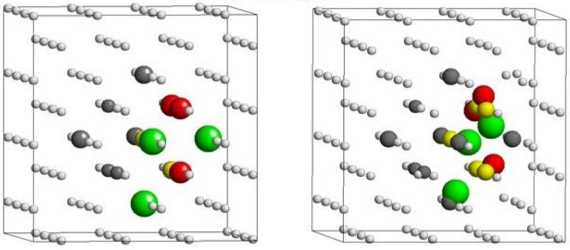

(ff)

3O5v3Y_AS-2

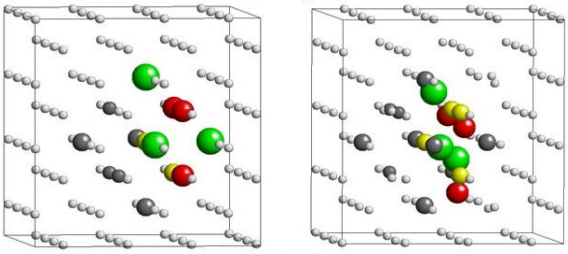

(gg)

3O5v3Y_AS-5

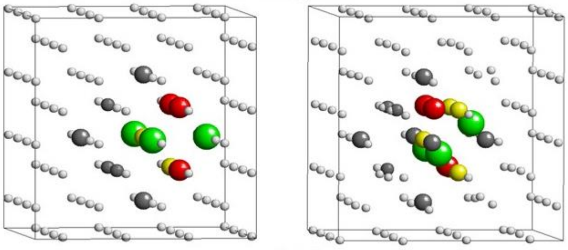

(hh)

3O5v5Y_SM-1

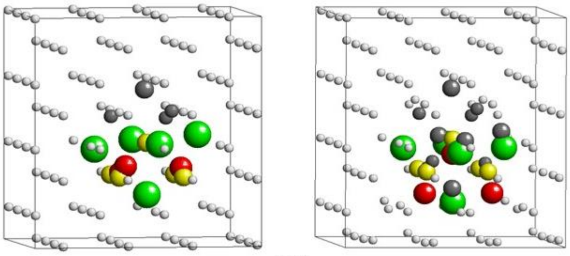

(ii)

3O5v5Y_PD-1

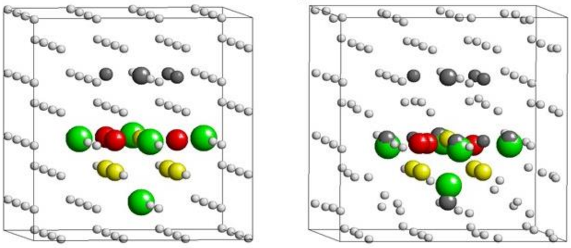

(jj)

3O5v5Y_PD-2

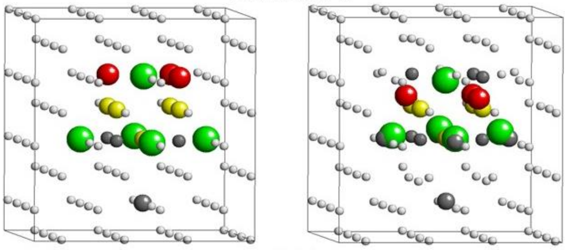

(kk)

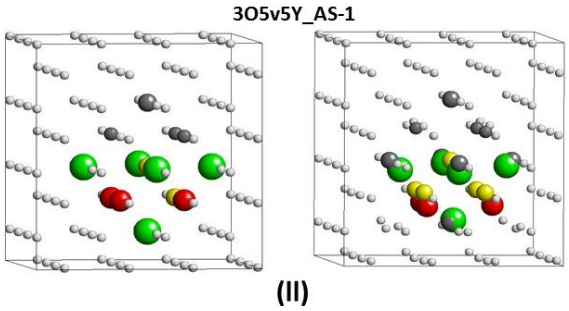

Fig. A3: Complete representation of the small clusters containing O, Y, Ti, and vacancies (v): SM, PD-2, and AS templates (cf. Fig. 3.2, chapter 3) used for the cluster construction (a), pictures of the clusters before (left) and after (right) relaxation (b-mm). Red, green, blue, gray, and yellow spheres show O, Y, Ti, Fe atoms, and vacancies, respectively (b-mm). Fig. 3.3 (b) (chapter 3) shows the total binding energy of the relaxed clusters per cluster constituent (O,v,Y,Ti).

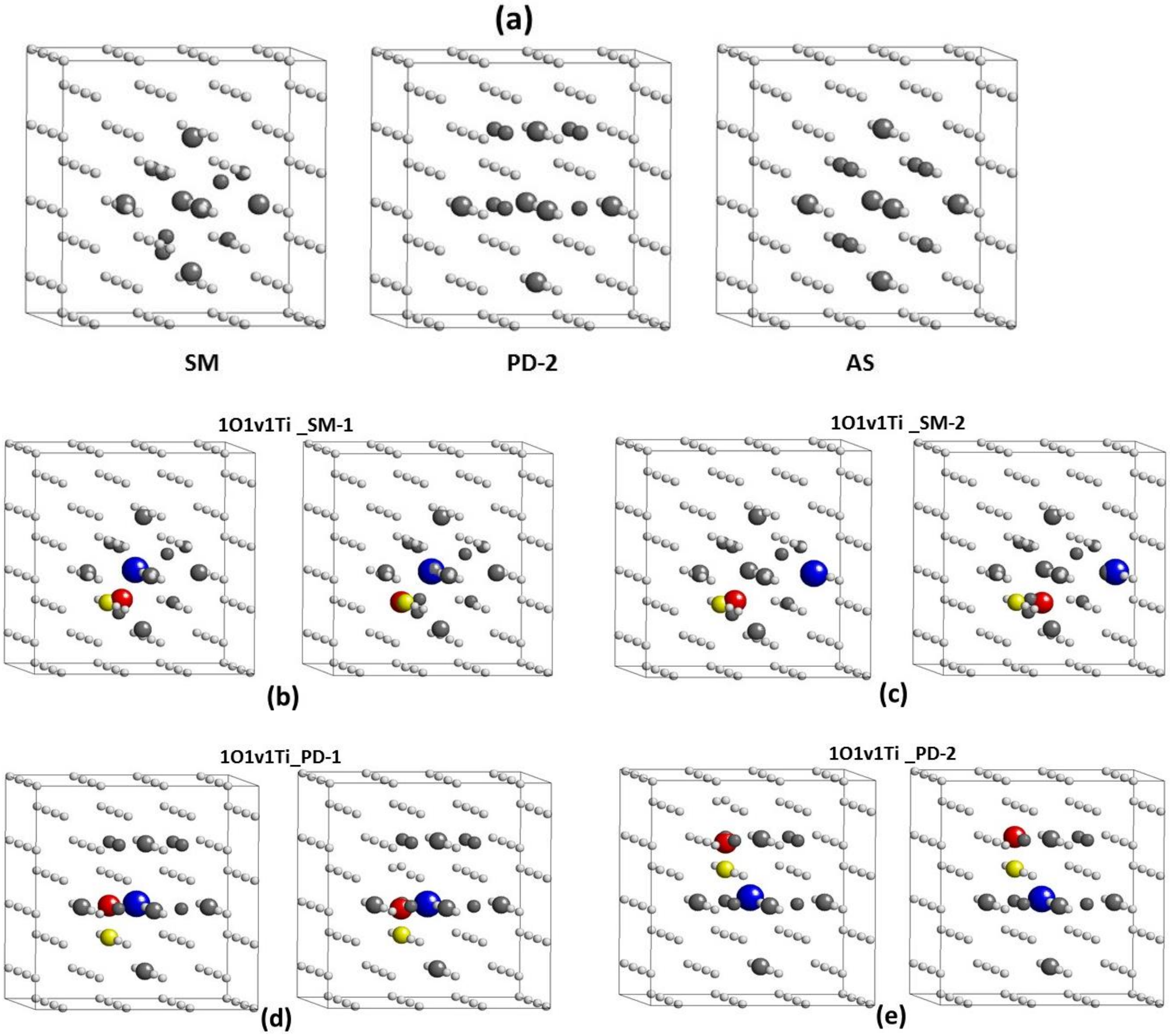

1O1v1Ti_AS-1

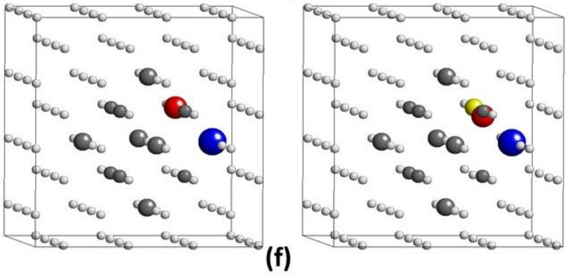

(f)

2O2v1Ti _SM-1

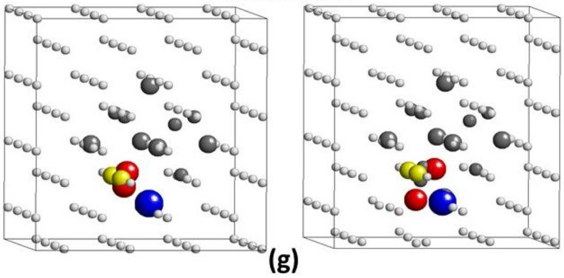

(g)

2O2v1Ti_SM-2

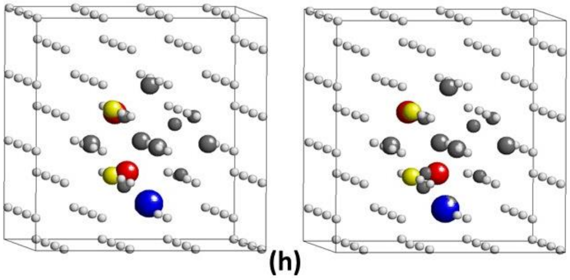

(h)

2O2v1Ti_SM-3

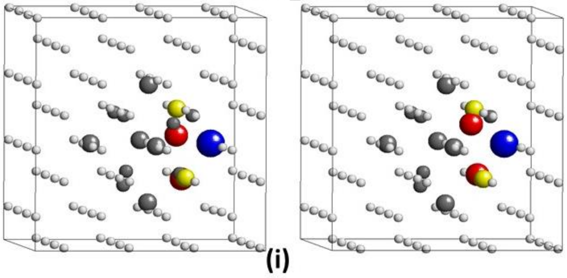

(i)

2O2v1Ti_PD-1

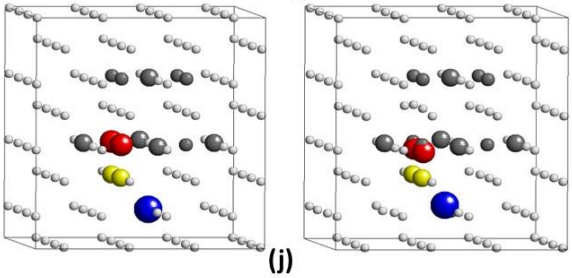

(j)

2O2v1Ti_PD-2

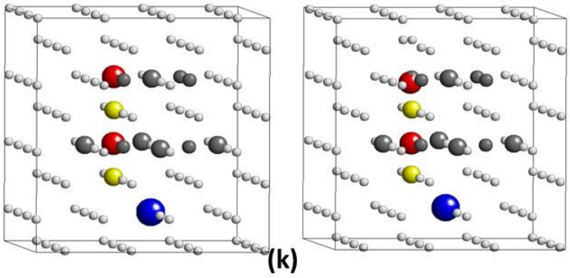

(k)

2O2v1Ti_PD-3

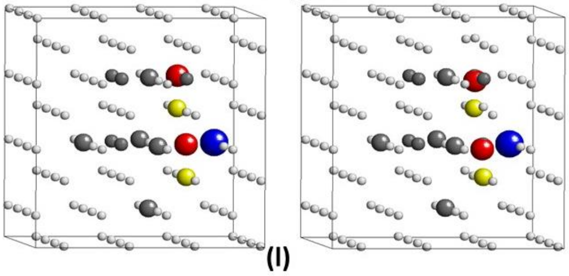

(l)

2O2v1Ti _AS-1

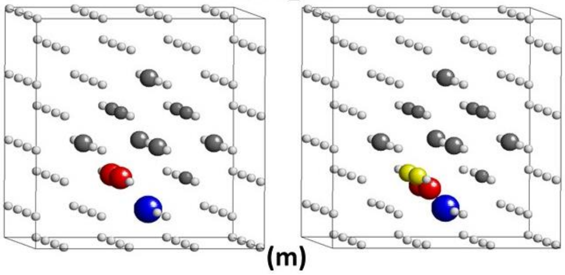

(m)

2O2v1Ti_AS-2

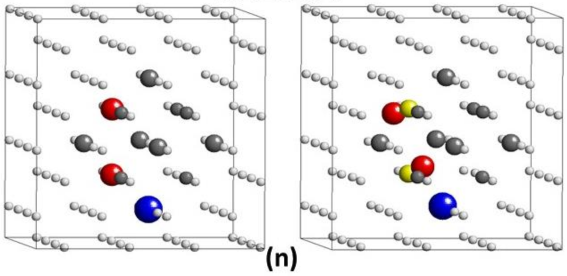

(n)

2O3v1Y1Ti_SM-1

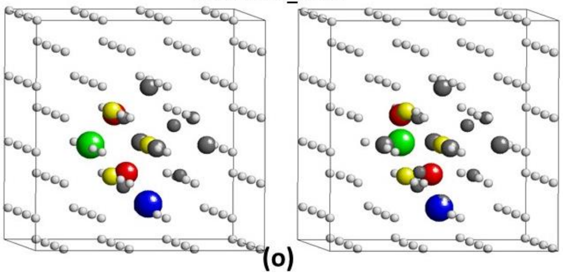

(o)

2O3v1Y1Ti_SM-2

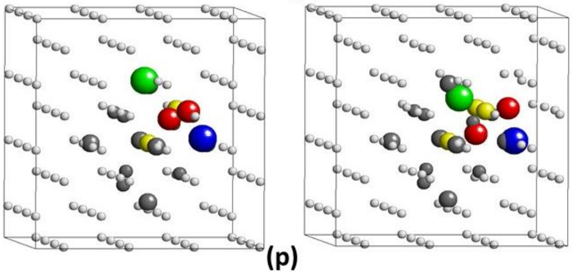

(p)

2O3v1Y1Ti_PD-1

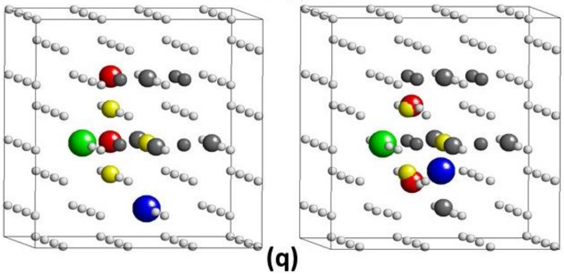

(q)

2O3v1Y1Ti _PD-2

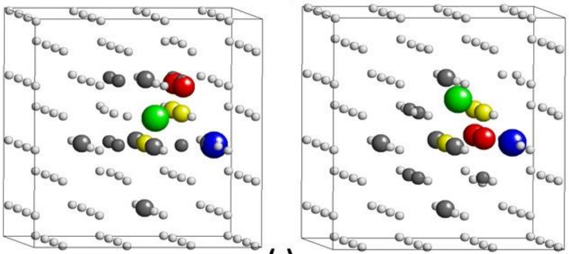

(r)

2O3v1Y1Ti_AS-1

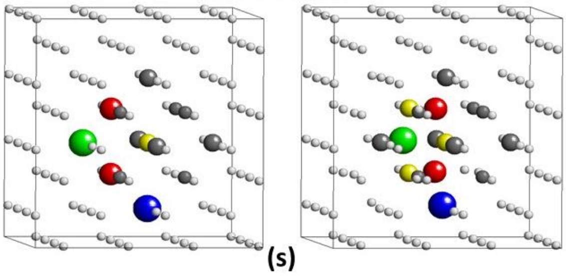

(s)

2O3v1Y1Ti_AS-2

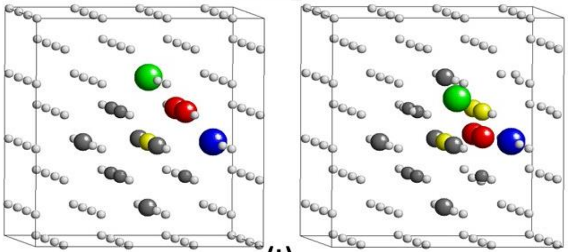

(t)

3O5v0Y3Ti_SM-1

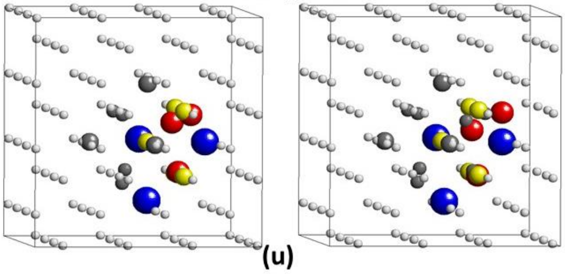

(u)

3O5v0Y3Ti_PD-1

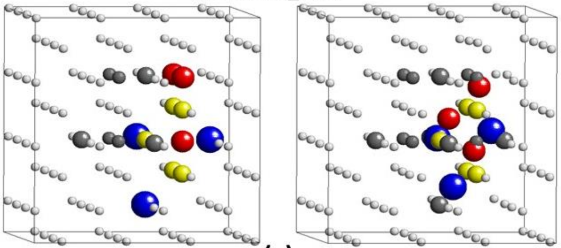

(v)

3O5v0Y3Ti_AS-1

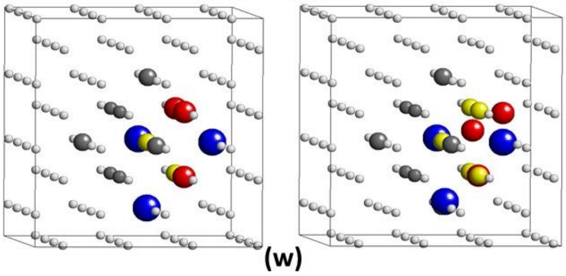

(w)

3O5v1Y2Ti_SM-1

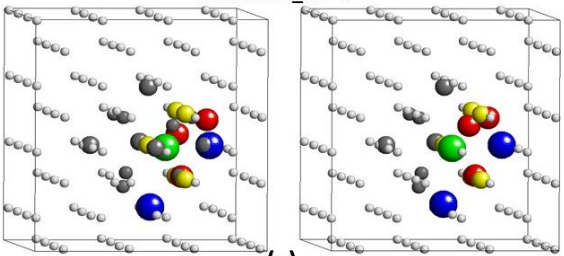

(x)

3O5v1Y2Ti_SM-2

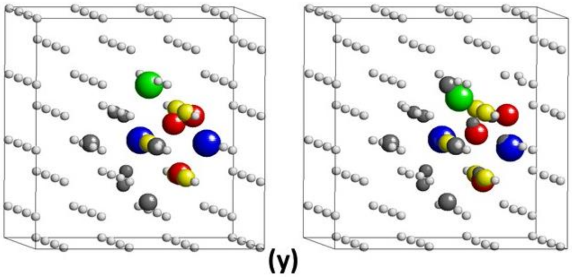

(y)

3O5v1Y2Ti_AS-1

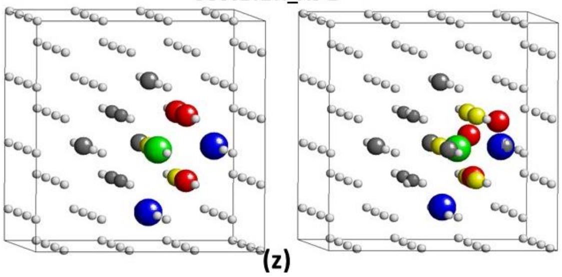

(z)

3O5v1Y2Ti_AS-2

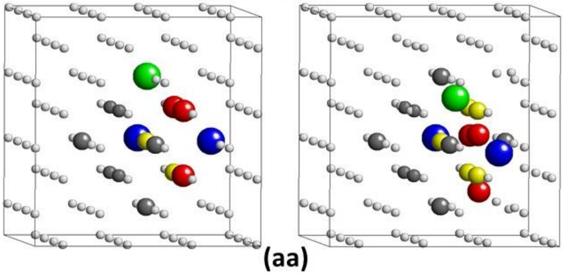

(aa)

3O5v2Y1Ti_SM-1

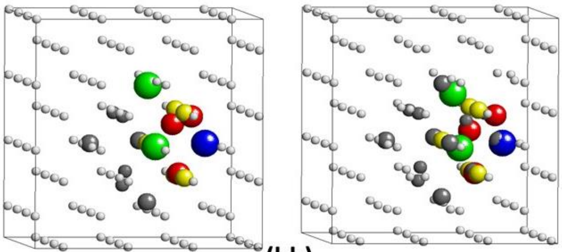

(bb)

3O5v2Y1Ti_PD-1

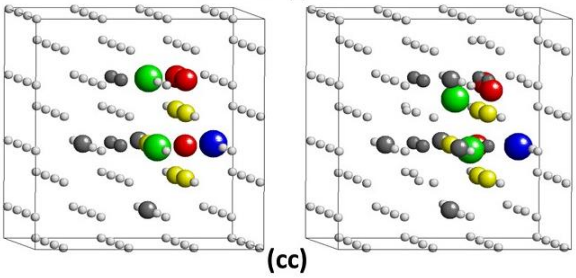

(cc)

3O5v2Y1Ti_AS-1

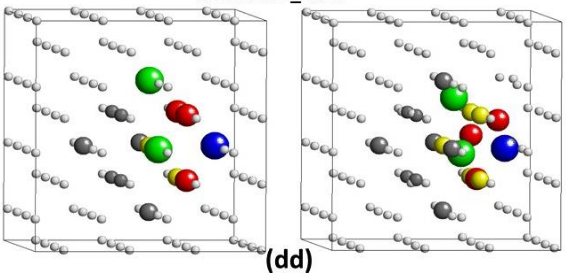

(dd)

3O4v2Y3Ti_SM-1

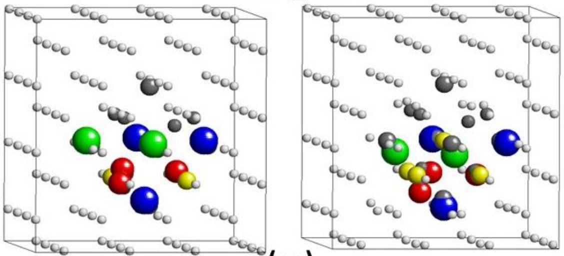

(ee)

3O4v2Y3Ti_PD-1

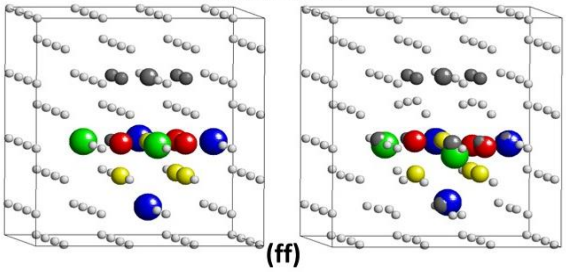

(ff)

3O4v2Y3Ti_AS-1

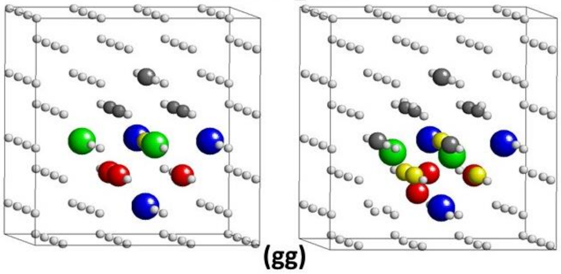

(gg)

3O5v2Y3Ti_SM-1

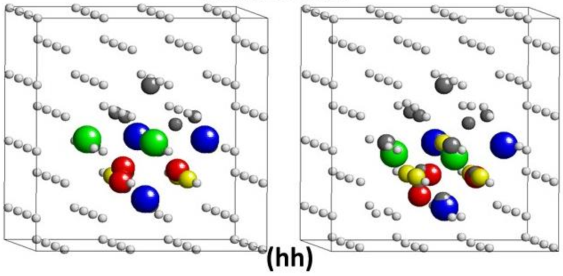

(hh)

3O5v2Y3Ti_PD-1

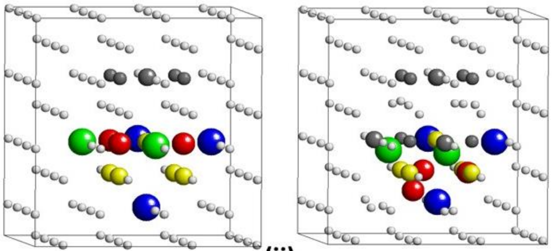

(ii)

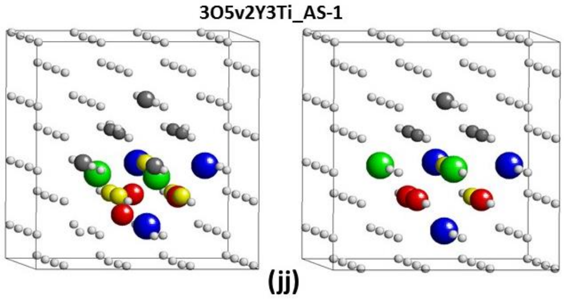
3O5v2Y3Ti_AS-1

(jj)

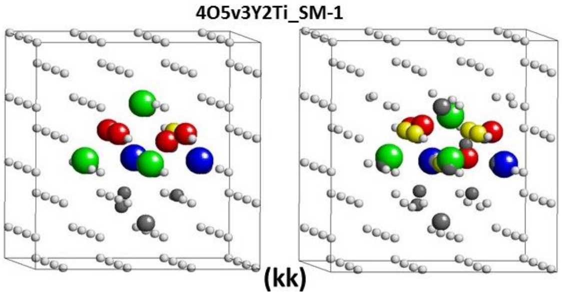
4O5v3Y2Ti_SM-1

(kk)

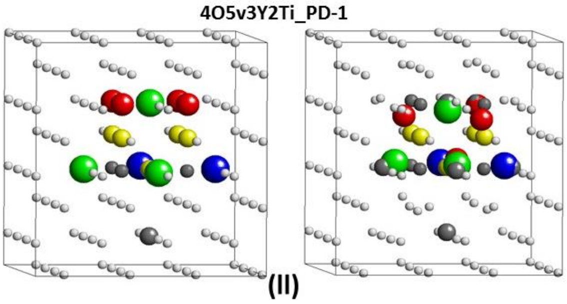
4O5v3Y2Ti_PD-1

(ll)

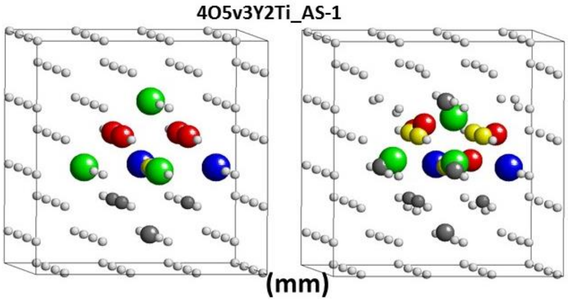
4O5v3Y2Ti_AS-1

(mm)

Fig. A4: 6O9v6Y clusters within a supercell containing 250 bcc lattice sites. The left and right figures show the atomic configurations before and after relaxation, respectively. The total binding energy and other characteristics of these clusters are given in Table 3.1 (chapter 3).

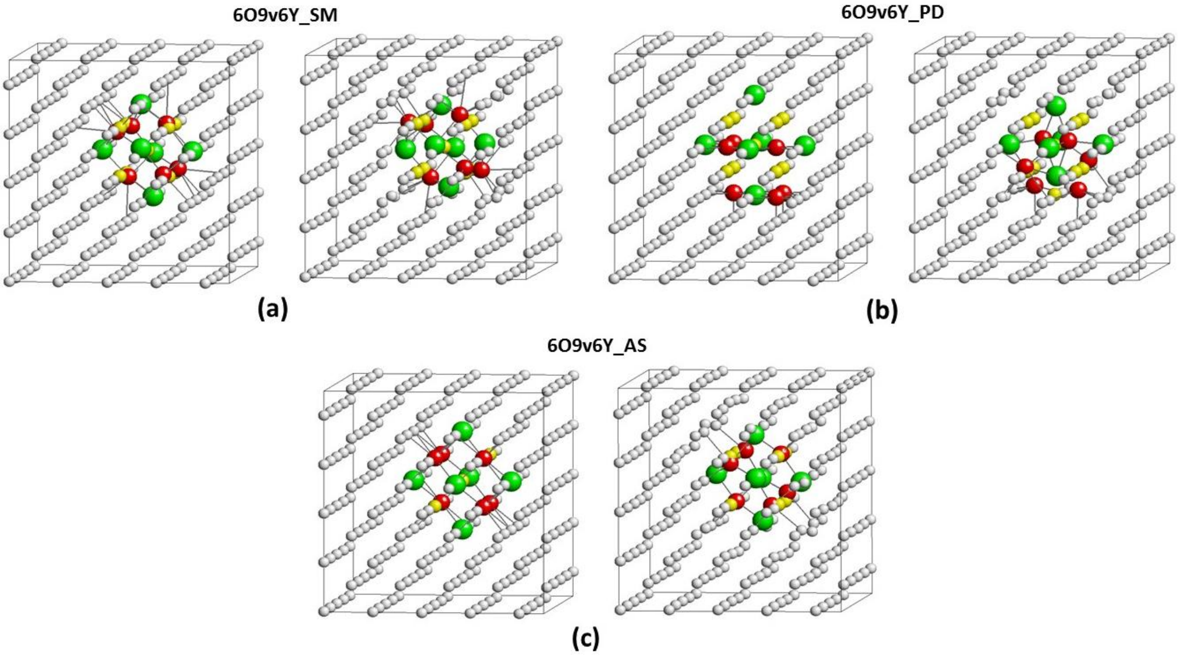

Fig. A5: 7O9v3Y3Ti clusters within a supercell containing 250 bcc lattice sites. The left and right figures show the atomic configurations before and after relaxation, respectively. The total binding energy and other characteristics of these clusters are given in Table 3.1.

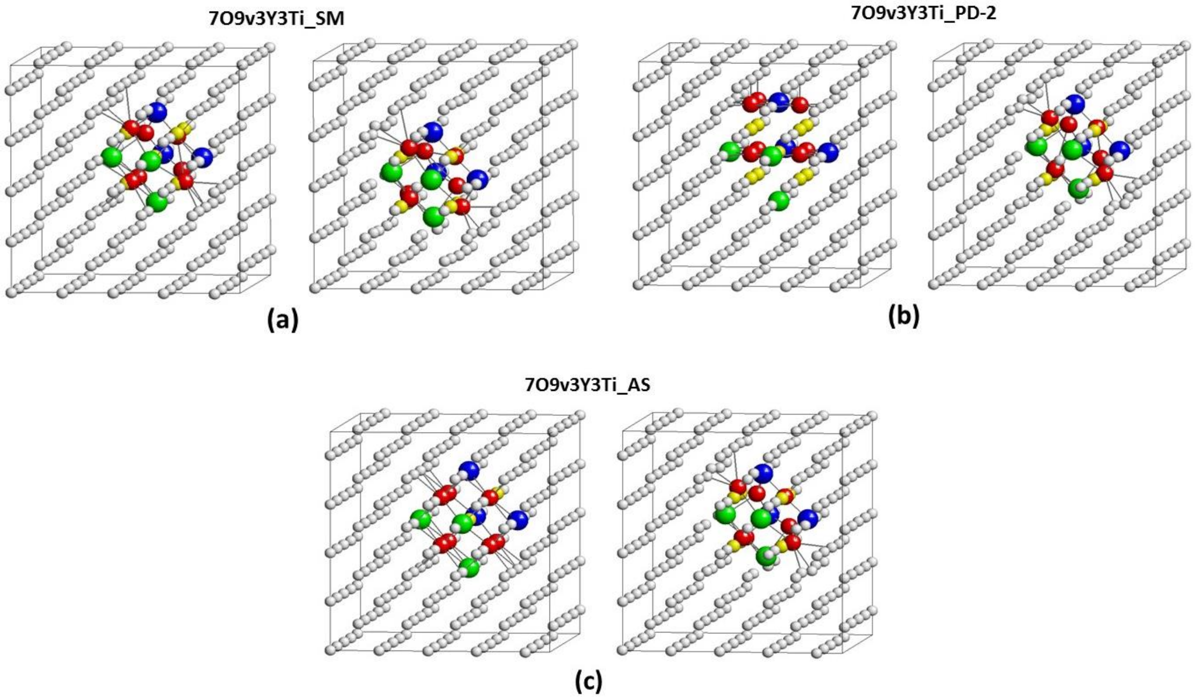

Fig. A6: Complete representation of atomic configurations of 6O9v6Y clusters with one O atom in the center (OC configurations). The left figures show the clusters before relaxation, whereas the middle and the right figures depict the relaxed clusters. Red arrows indicate the site from which one O atom was shifted towards the center (cf. also Fig. 3.1, chapter 3). The black arrows denote the viewing direction, which was applied to get the right figures. The total binding energy and other characteristics of these clusters are given in Table 3.2 (chapter 3).

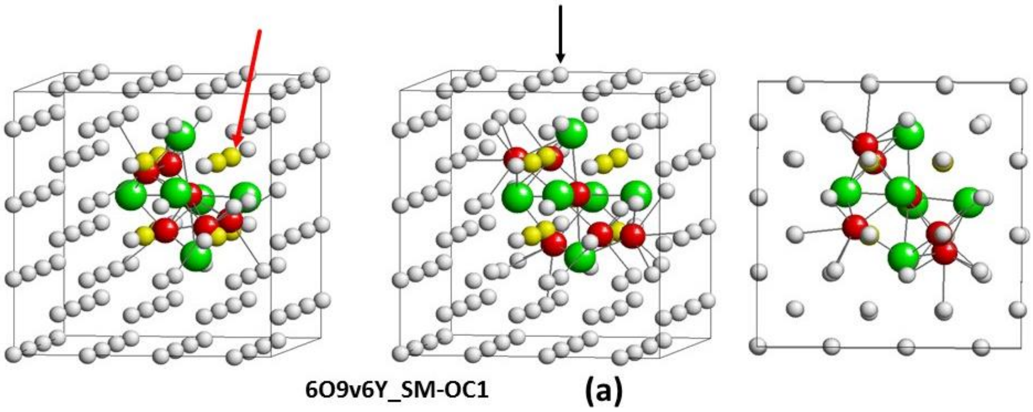

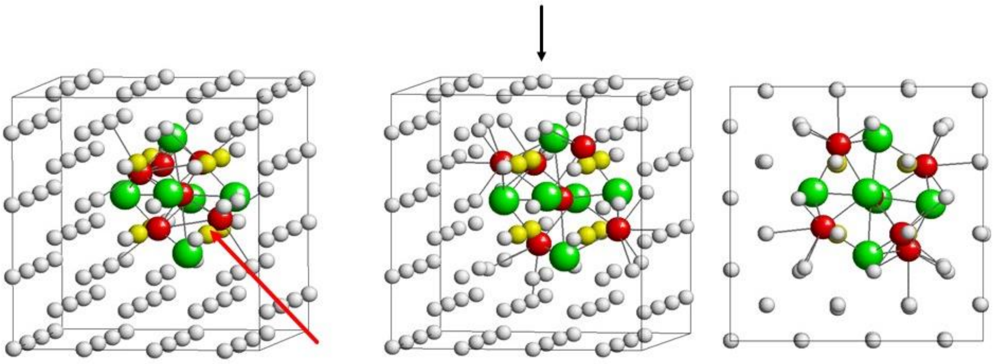

6O9v6Y_SM-OC2 **(b)**

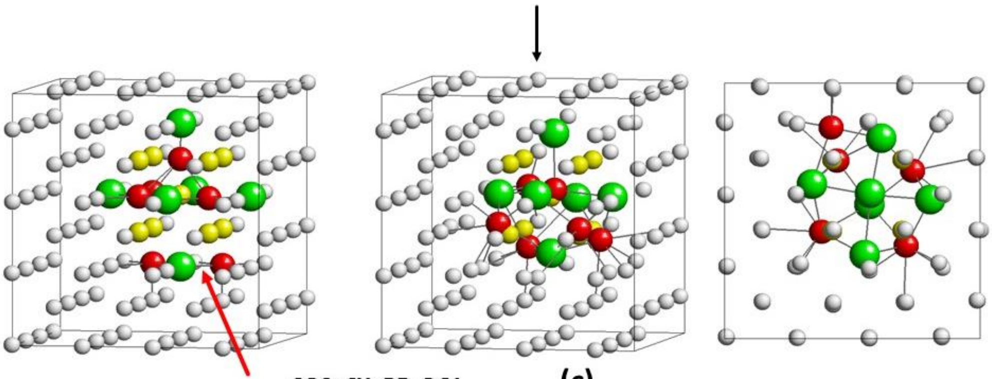

6O9v6Y_PD-OC1 **(c)**

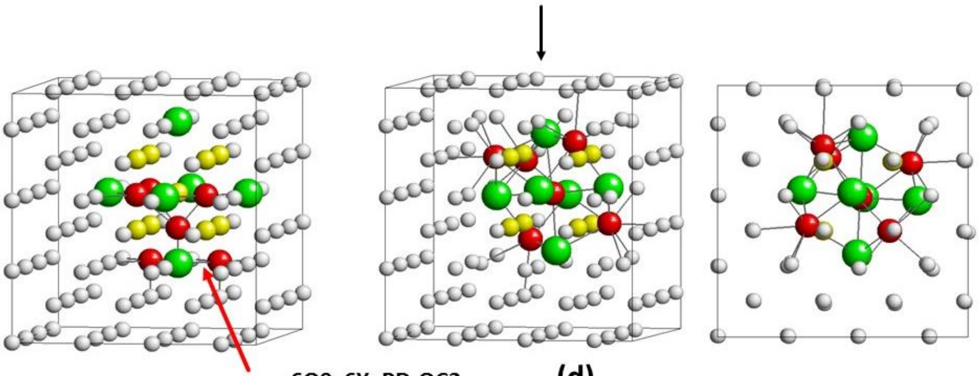

6O9v6Y_PD-OC2 **(d)**

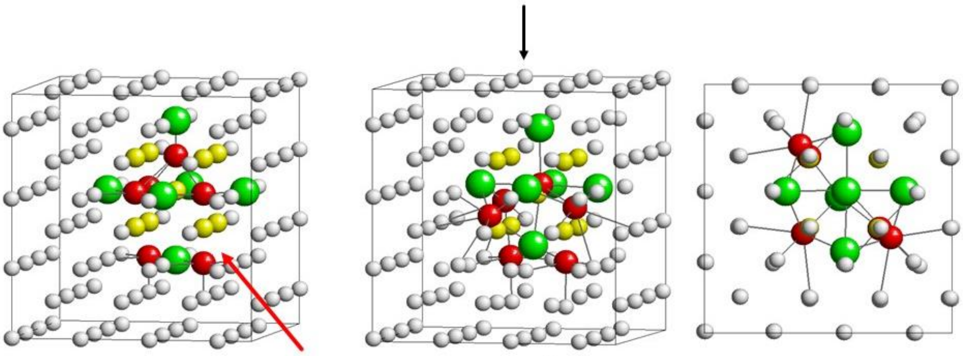

6O9v6Y_PD-OC3 **(e)**

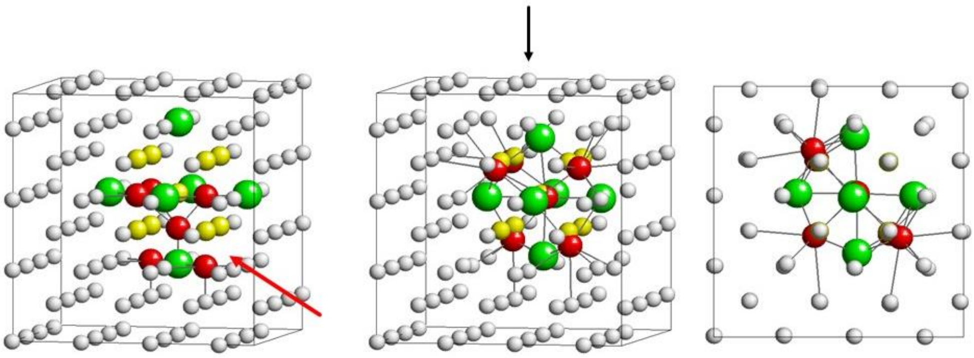

6O9v6Y_PD-OC4 (f)

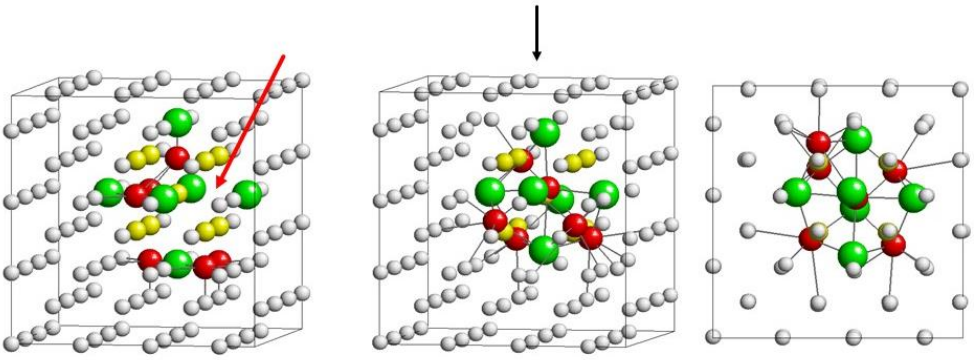

6O9v6Y_PD-OC5 (g)

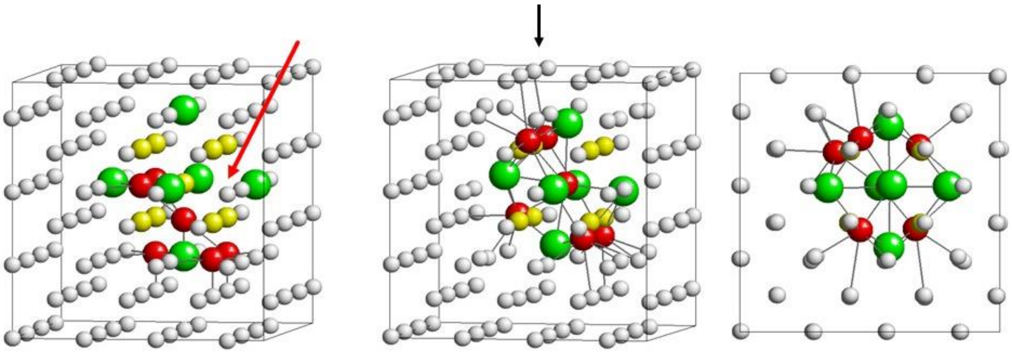

6O9v6Y_PD-OC6 (h)

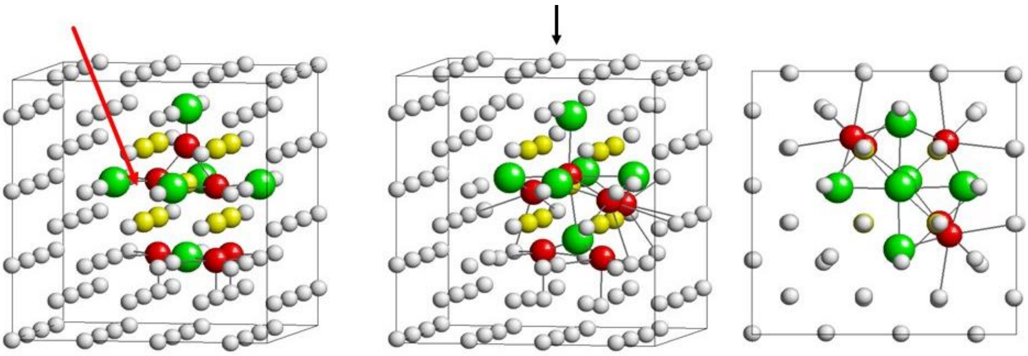

6O9v6Y_PD-OC7 (i)

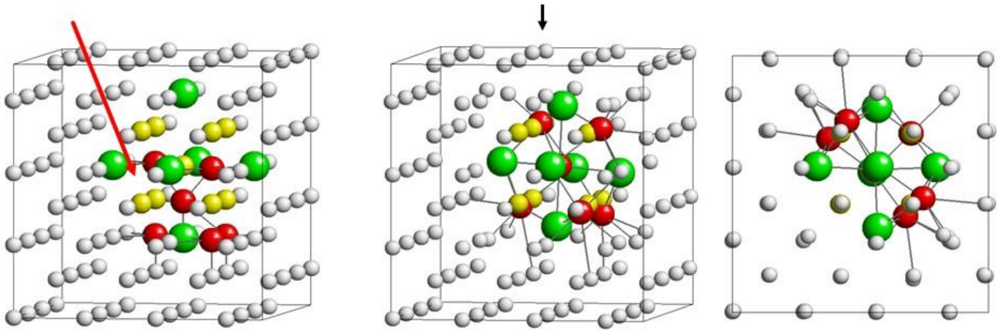

6O9v6Y_PD-OC8 **(j)**

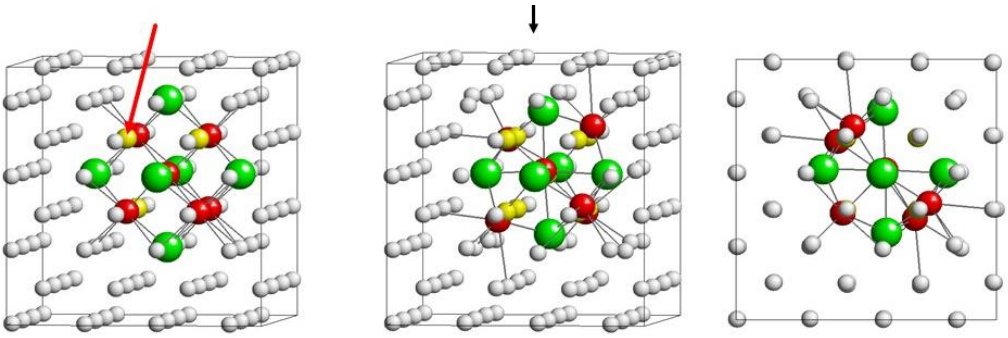

6O9v6Y_AS-OC1 **(k)**

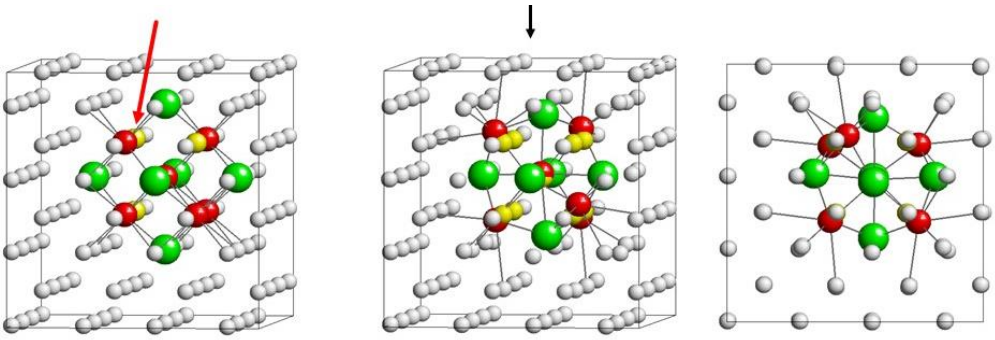

6O9v6Y_AS-OC2 **(l)**

Fig. A7: Complete representation of atomic configurations of 7O9v3Y3Ti clusters with one O atom is in the center (OC configurations). See Fig. A6 for the explanation of the details of the pictures.

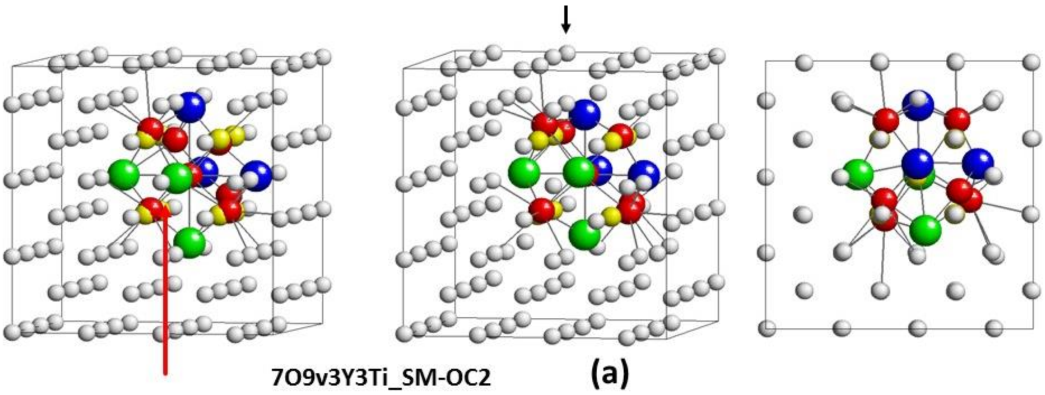

7O9v3Y3Ti_SM-OC2 **(a)**

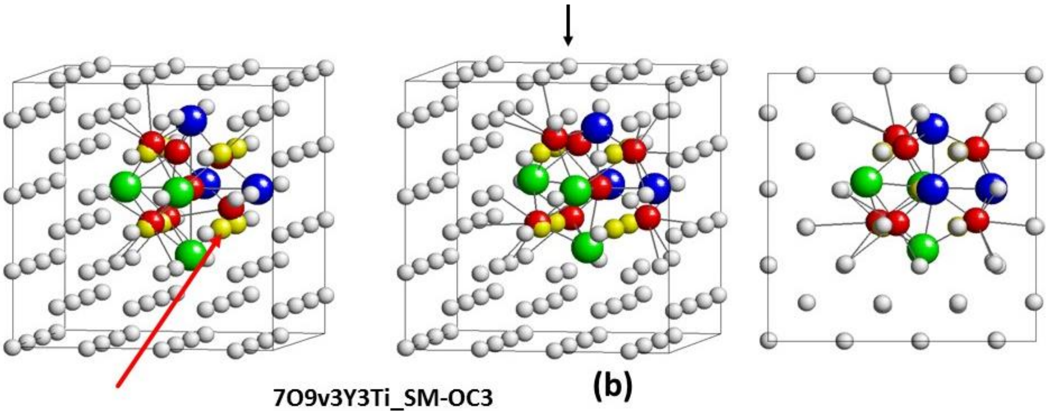

7O9v3Y3Ti_SM-OC3 **(b)**

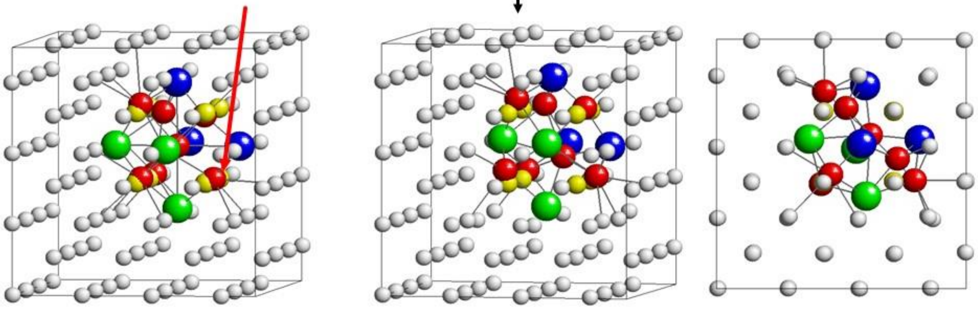

7O9v3Y3Ti_SM-OC4 **(c)**

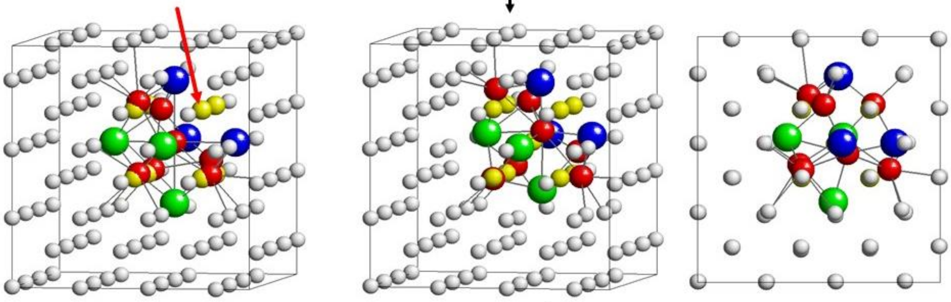

7O9v3Y3Ti_SM-OC5 **(d)**

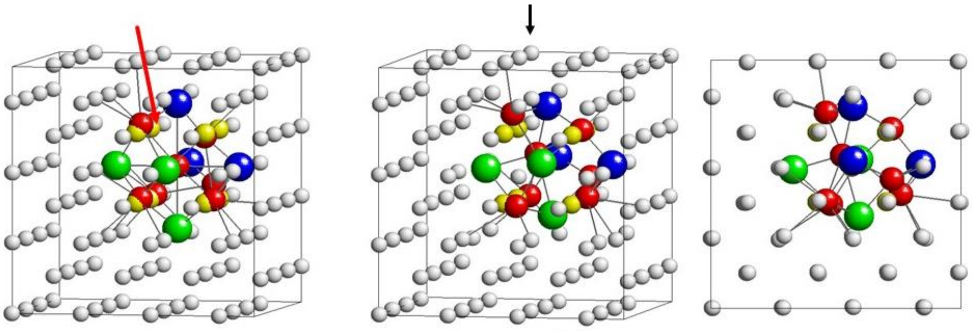

7O9v3Y3Ti_SM-OC6 **(e)**

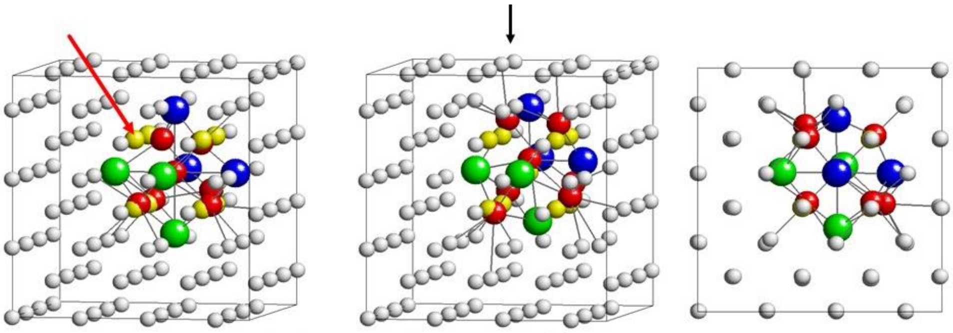

7O9v3Y3Ti_SM-OC7 (f)

Fig. A8: Atomic configurations of 6O9v6Y clusters with one O atom in the center (OC configurations), within a supercell containing 250 bcc lattice sites. See Fig. A6 for the explanation of the details of the pictures.

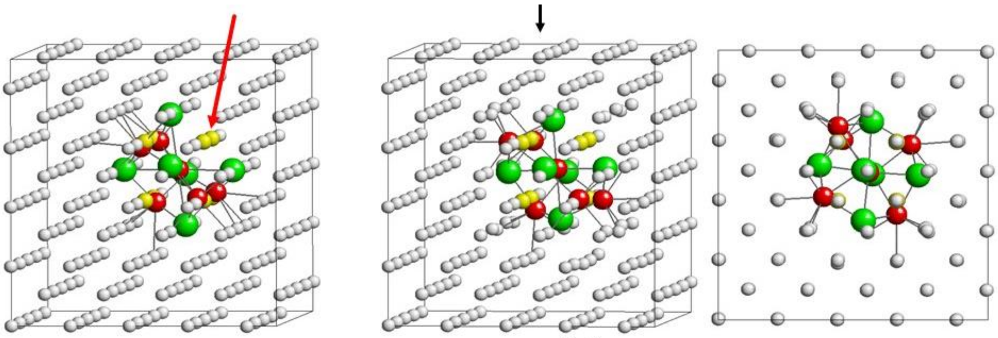

6O9v6Y_SM-OC1 (a)

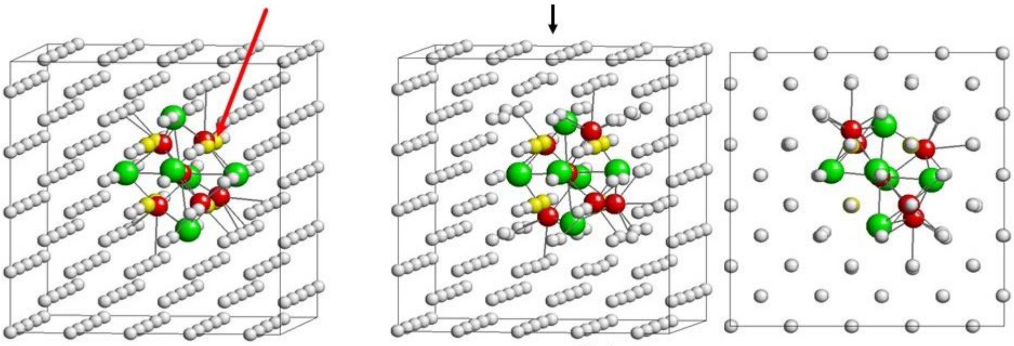

6O9v6Y_SM-OC2 (b)

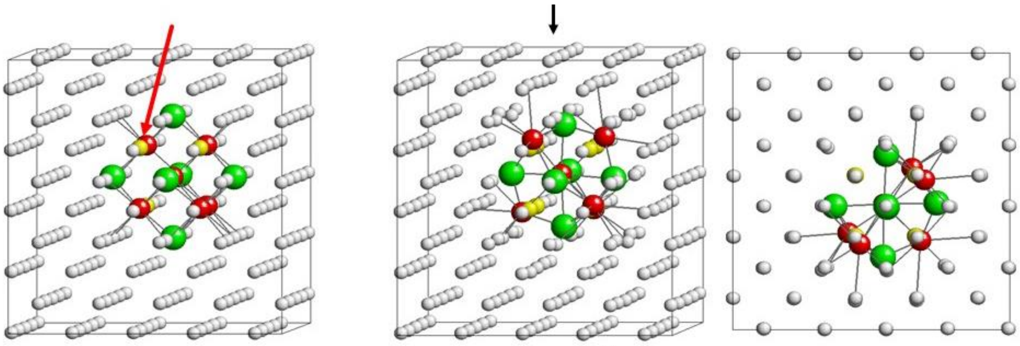

6O9v6Y_AS-OC1 (c)

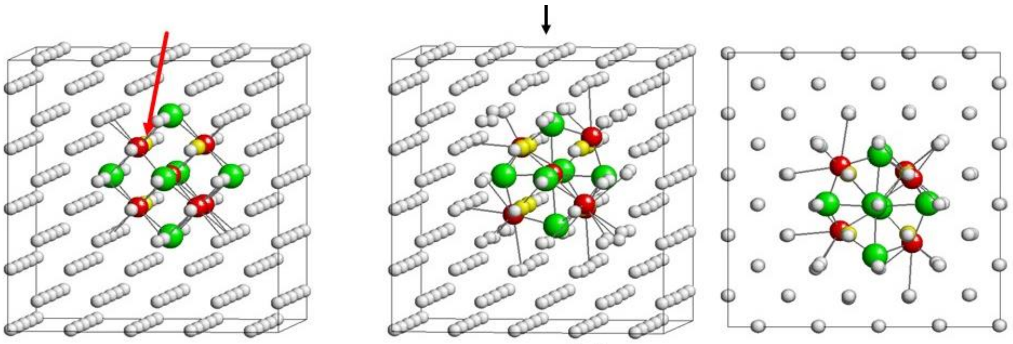

6O9v6Y_AS-OC2 (d)

Appendix-B

Summary of all details related to chapter 4:

Relaxed cluster configurations containing He atoms, vacancies, and self-interstitial atoms

App-B1: Relaxed cluster configurations containing one He atom

In all following figures, the cyan ball represents the He atom. The values of He binding and incorporation energy are given in the form $(E_b^{He},\ E_{incorp}^{He})$. All values are in eV. Only parts of the supercell are shown in the figures.

1. He in the cage-like (CL) O-Y cluster

Fig. B1: The initial He sites considered for the calculation of He interaction with the cage like O-Y (CL) cluster. White, green, and red balls represents Fe, Y, and O, respectively. Gray and magenta balls denote octahedral and tetrahedral interstitial sites in the underlying bcc lattice. Gold and light green balls are vacant sites at the cluster center and the cluster-iron interface. Vacancies which belong to the cluster are represented by yellow balls. Note that all sites of the underlying perfect bcc lattice which are not occupied by metal atoms (Fe, Y, Ti) are counted as vacancies. That means that all O atoms are assigned to vacancies. The above definition of vacancies is not strictly necessary. However, such a definition may be helpful to understand better the properties of the clusters. Purple balls show possible sites for an additional vacancy and an additional self-interstitial atom (see sections *App-B4* and *App-B5*).

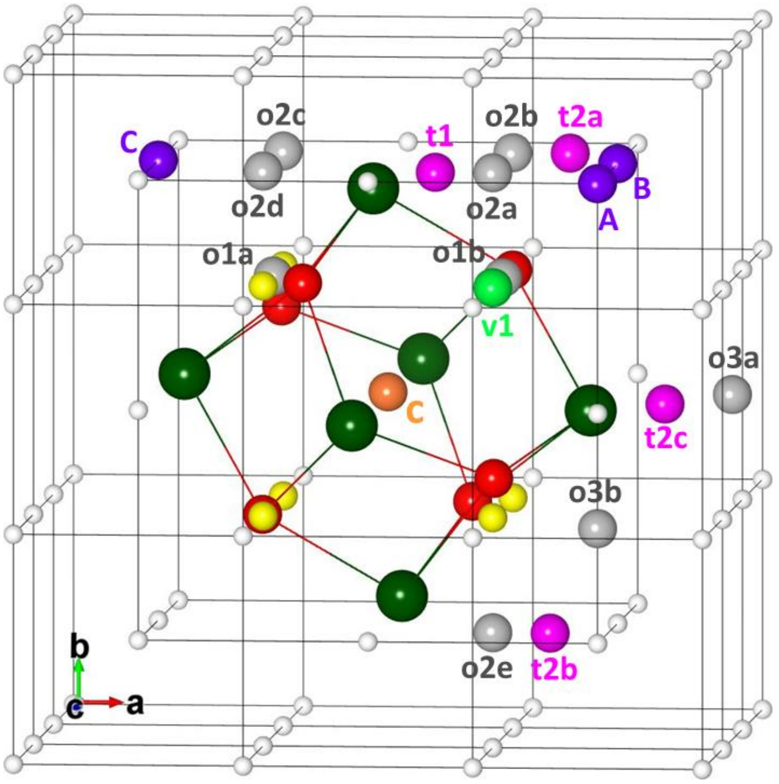

The following figures show relaxed configurations

Fig. B1a: He at the center of cluster stays there.

center (-3.31, 1.25)

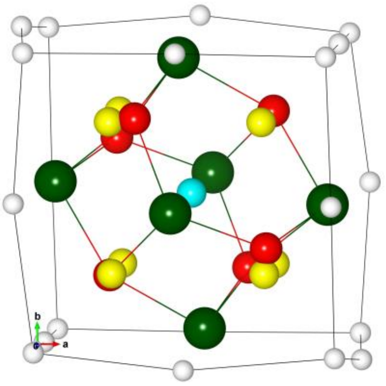

Fig. B1b: He on v1, o1b, o2a, and t1 relaxes to a stable site near the vacancy position v1. In the following such stable site are called interfacial vacant sites (IVS).

v1 (-3.18, 1.37)

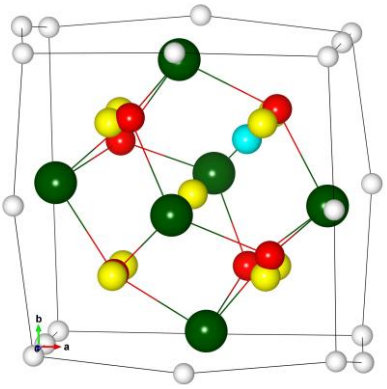

o1b (-3.17, 1.38)

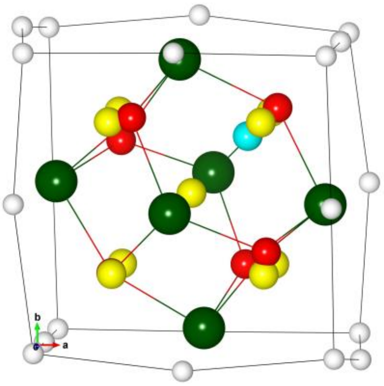

o2a (-3.16, 1.39)

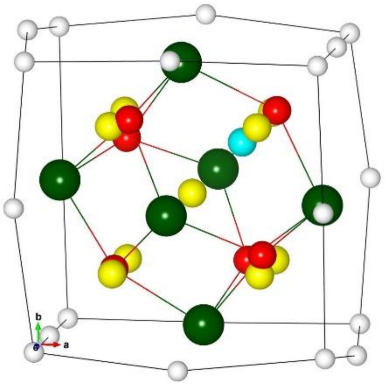

t1 (-3.18, 1.37)

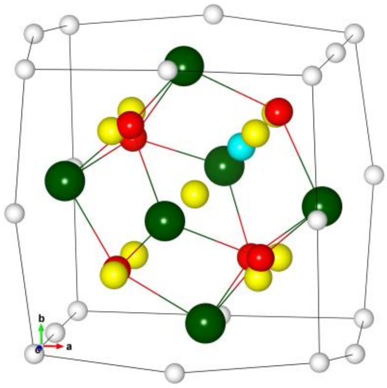

Fig. B1c: In the following nine cases a transformation to cluster configurations with oxygen in the center (OC) occurs, with He on a IVS close to a vacancy position. Here He binding and incorporation energies were determined with OC cluster without He as reference.

o2b (-2.65, 1.91)

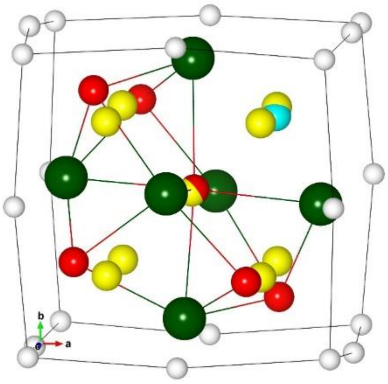

o2c (-2.65, 1.91)

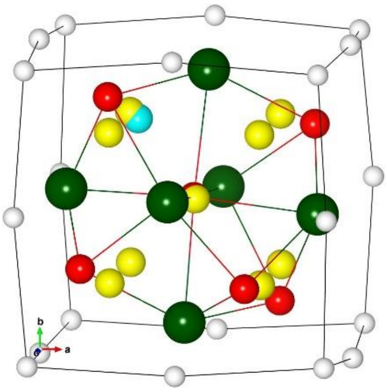

o2d (-2.65, 1.91)

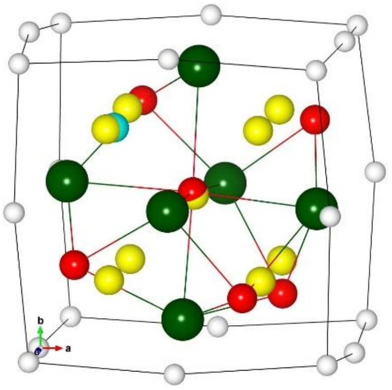

o2e (-2.65, 1.91)

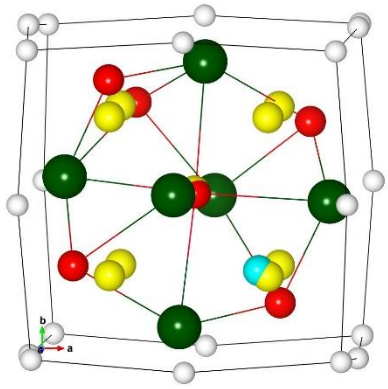

o3a (-2.75, 1.80)

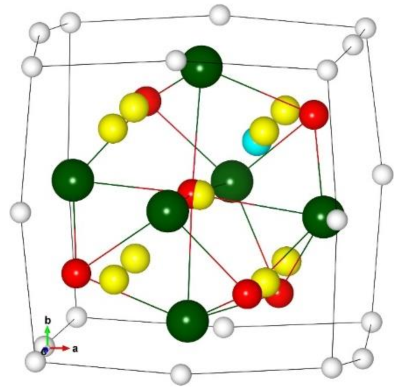

o3b (-2.65, 1.90)

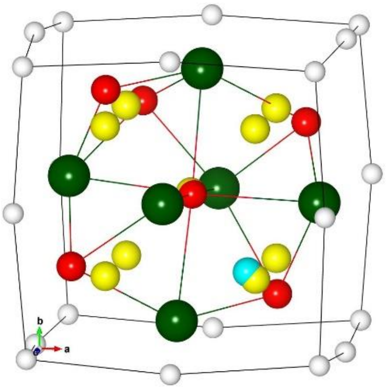

t2a (-2.65, 1.91)

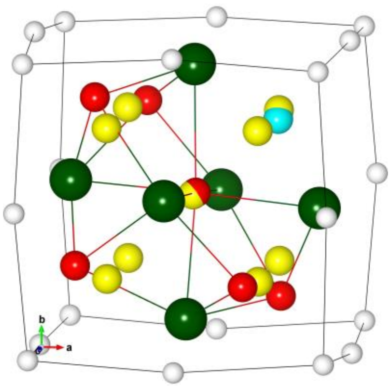

t2b (-2.65, 1.91)

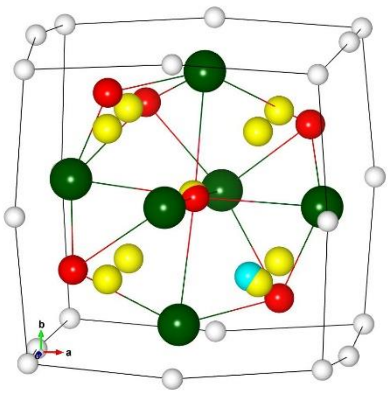

t2c (-2.75, 1.80)

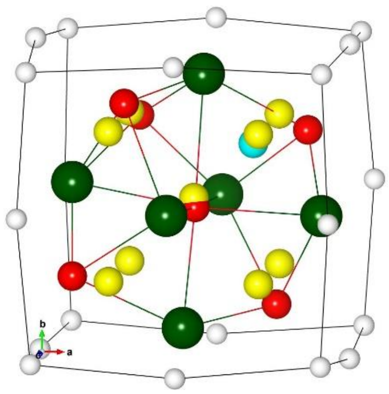

Fig. B1d: He on o1a relaxes to an interfacial interstitial site in vicinity of the octahedron edge with two Y, and close to two O atoms. In the following the term interfacial interstitial site (IIS) is generally used for relaxed He sites which are neither a center site nor an interfacial vacant site (IVS).

o1a (-2.01, 2.54)

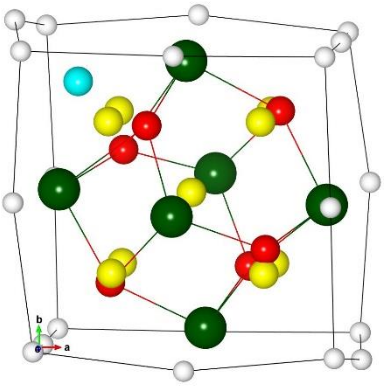

2. He in the O-Y cluster with oxygen in the center (OC)

Fig. B2: The initial He sites considered for the calculation of He interaction with the O-Y cluster with oxygen in the center (OC). White, green, and red balls represent Fe, Y, and O, respectively. Gray and magenta balls denote octahedral and tetrahedral interstitial sites in the underlying bcc lattice. Light green balls are vacant sites at the cluster-iron interface. Vacancies which belong to the cluster are represented by yellow balls. Purple balls show possible sites for an additional vacancy and an additional self-interstitial atom (see sections *App-B4* and *App-B5*).

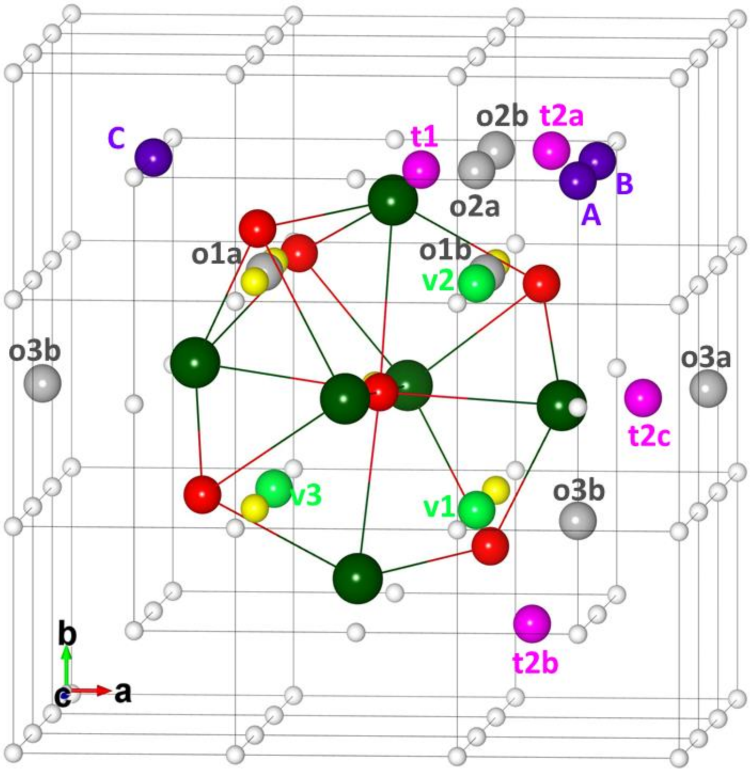

The following figures show relaxed configurations.

Fig. B2a: He on v1, v2, v3 relaxes to nearby IVS.

v1 (-2.56, 2.02)

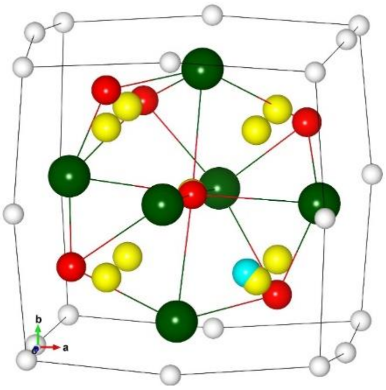

v2 (-2.71, 1.84)

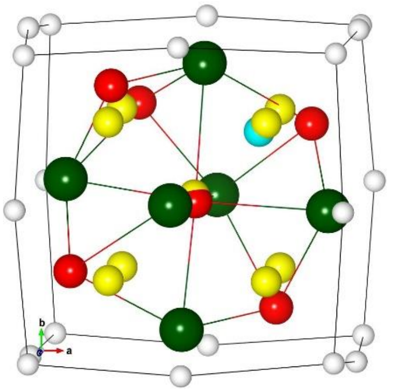

v3 (-2.81,1.74)

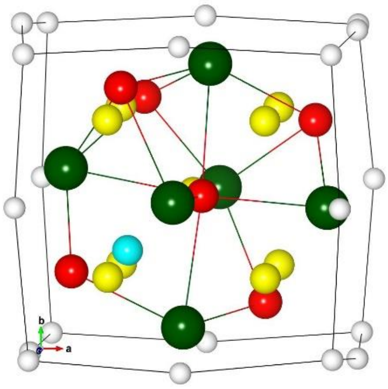

Relaxation to an IVS position close to v1:

o3a (-2.65, 1.91)

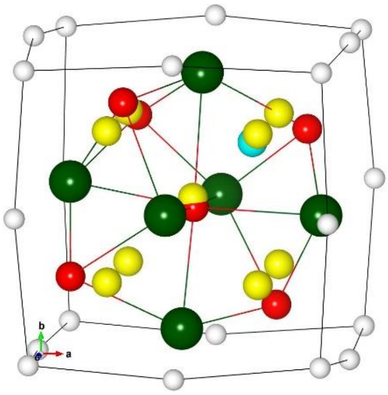

t2b (-2.65, 1.91)

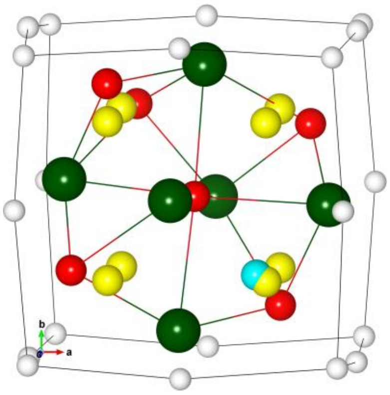

Relaxation to an IVS position close to v2:

o1b (-2.75, 1.80)

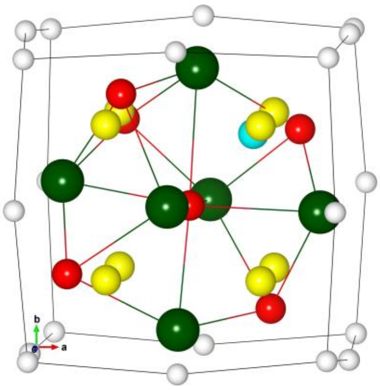

o2a (-2.75, 1.80)

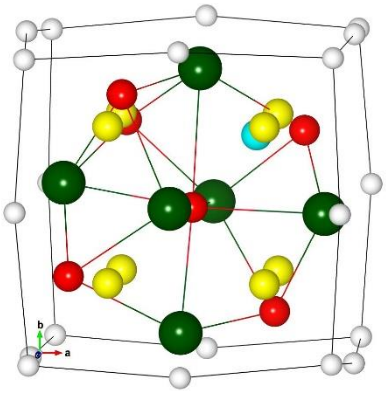

o3b (-2.75, 1.80)

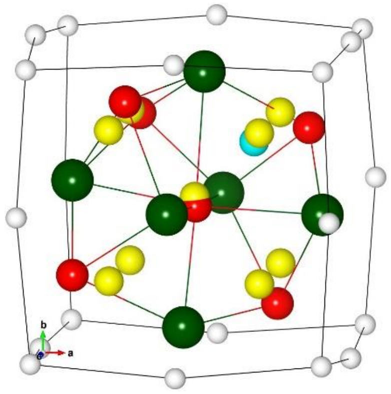

t1 (-2.75, 1.80)

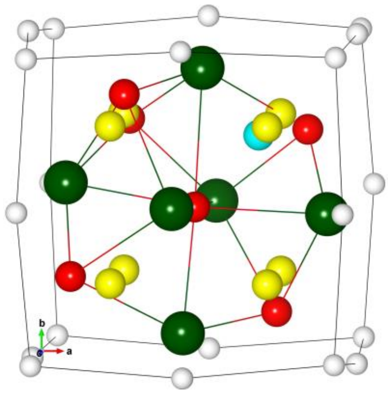

t2a (-2.75, 1.80)

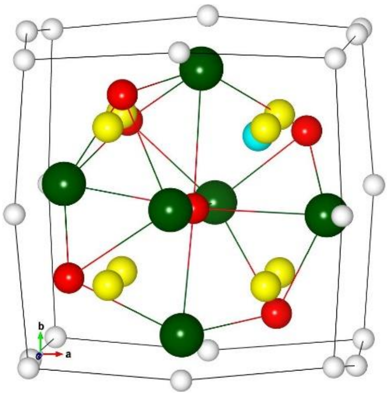

t2c (-2.75, 1.80)

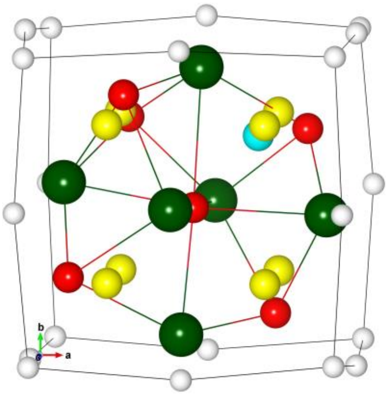

Relaxation to an IVS position close to v3:

o3c (-2.81, 1.74)

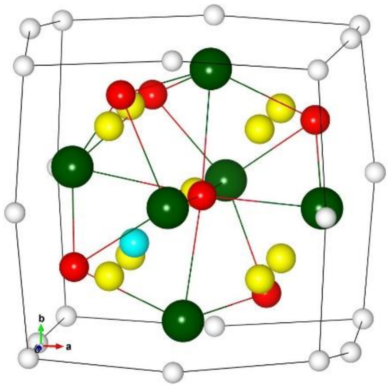

Fig. B2b: He on o1a and o2b relaxes to interfacial interstitial sites (IIS).

o1a (-2.10, 2.46)

He occupies an IIS in the environment of an octahedron edge formed by two Y atoms. with two O atoms in the

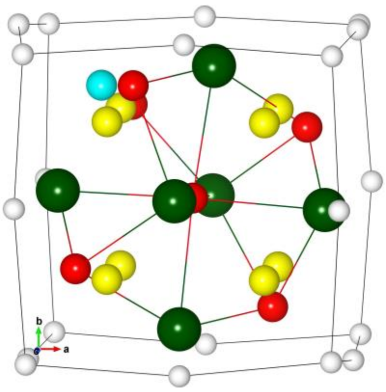

o2b (-2.07, 2.40)

He occupies an IIS in the environment of an octahedron edge formed by two Y atoms, without two O atoms in the

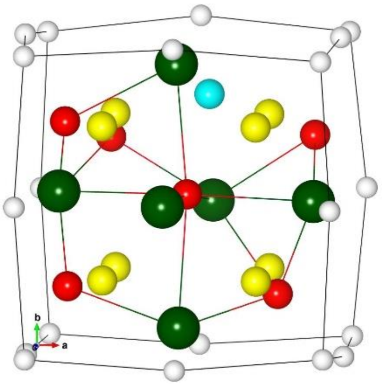

3. He in the cage-like (CL) O-Y-Ti cluster

Fig. B3: The initial He sites considered for the calculation of He interaction with the CL O-Y-Ti cluster. White, green, blue and red balls represent Fe, Y, Ti and O, respectively. Gray and magenta balls denote octahedral and tetrahedral interstitial sites in the underlying bcc lattice. Gold and light green balls are vacant sites at the cluster center and the cluster-iron interface. Vacancies which belong to the cluster are represented by yellow balls. Purple balls show possible sites for an additional vacancy and an additional self-interstitial atom (see sections *App-B4* and *App-B5*).

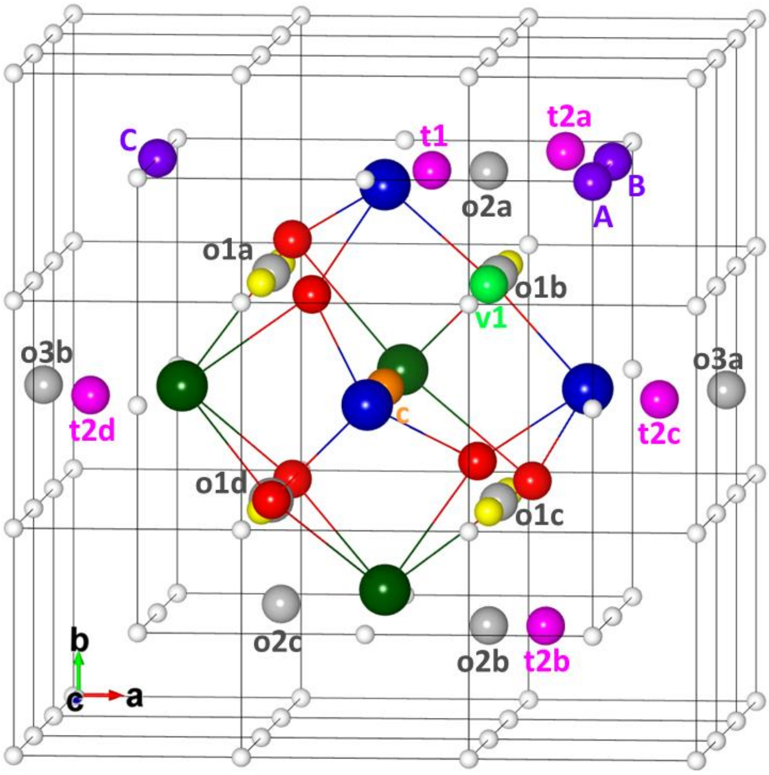

The following figures show relaxed configurations.

Fig. B3a: He at the center of the cluster stays there.

Center (-2.78, 1.78) : This configuration was also found by Danielson et al. (See Fig. 3e in Ref [58]) with the incorporation energy of 1.85 eV.

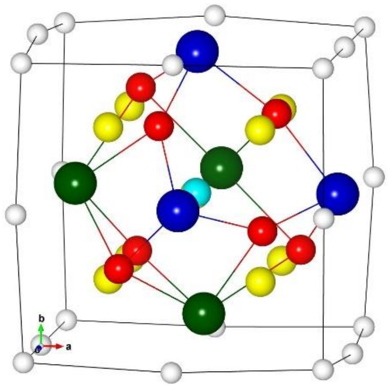

Fig. B3b: He relaxes to an IVS near v1.
(cf. Fig. 3d in Ref [58], incorporation energy of 2.26 eV)

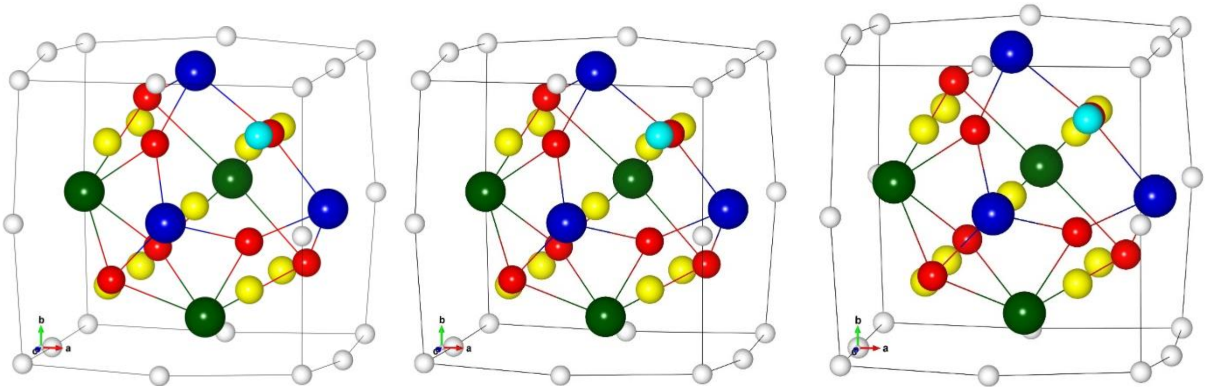
v1 (-2.38, 2.18) o1b (-2.38, 2.18) o2a (-2.38, 2.18)

Fig. B3c: He relaxes to different IIS.

o1d (-2.42, 2.14)

He is on an IIS close to the octahedron edge with 2Y at corners (cf. Fig. 3c in Ref [58] : incorporation energy of 2.19 eV)

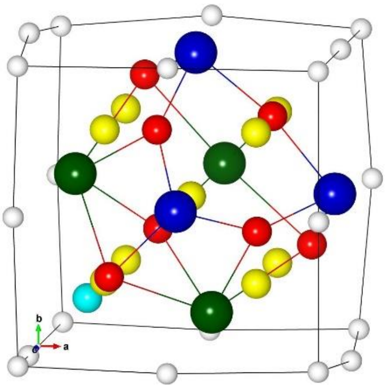

o2b (-2.30, 2.25)

He is on an IIS close to the face with 1 Y and 2 Ti at corners (cf. Fig. 3a in Ref [58] : incorporation energy of 2.31 eV)

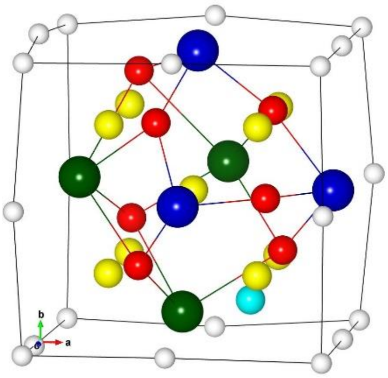

o2c (-2.26, 2.30)

He is on an IIS close to the octahedron face with 3Y at corners (cf. Fig. 3b in Ref [58] : incorporation energy of 2.34 eV)

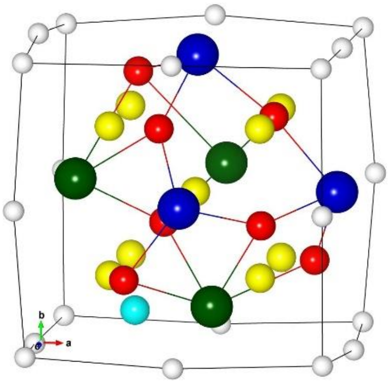

o1a (-2.45, 2.10)

He relaxes to an IIS close to the octahedron edge with 2Y at corners

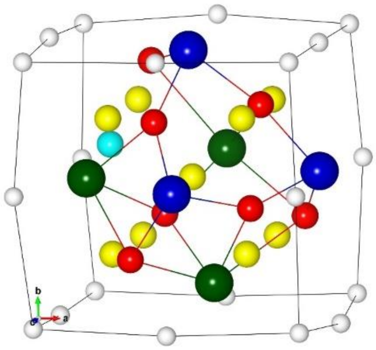

t2d (-2.49 , 2.06)

He relaxes to another IIS close to the octahedron edge with 2Y at corners

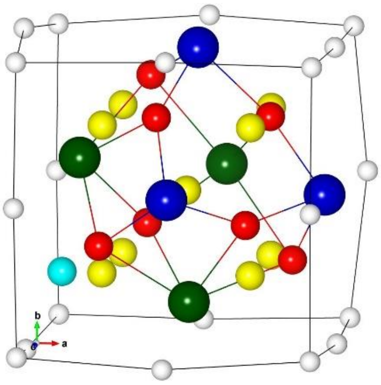

t2b (-2.34, 2.21)

He is on an IIS close to the octahedron face with 1 Y and 2 Ti at corners

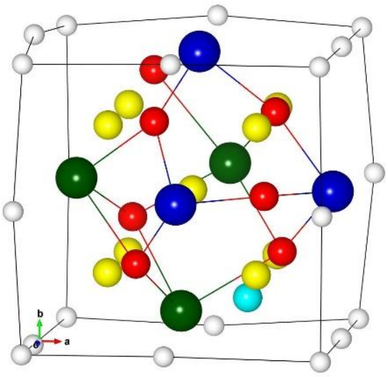

o3b (-2.25, 2.30)

He is on an IIS near the octahedron face with 3Y

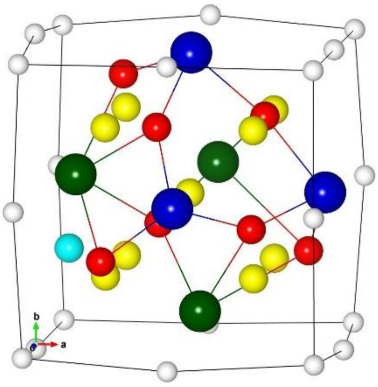

o1c (-2.26, 2.29)

He is on an IIS asymmetrically placed close to the octahedron face with 2 Y and 1 Ti

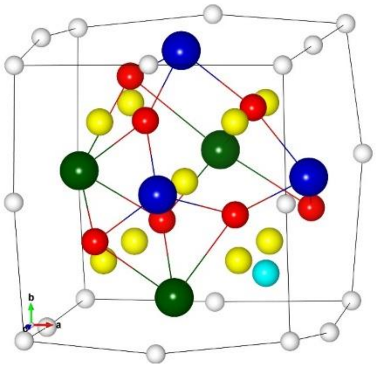

Fig. B3d: He is stable near the initial interstitial sites.

t2a (-1.55, 3.01)

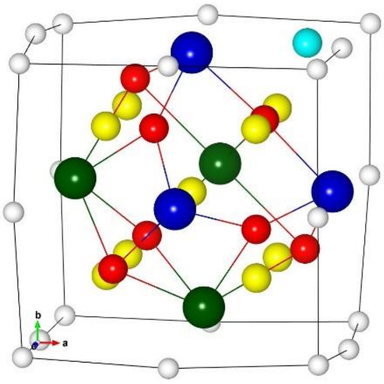

t2c (-0.31, 4.26)

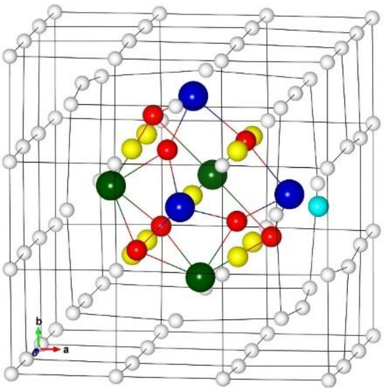

o3a (-0.24, 4.32)

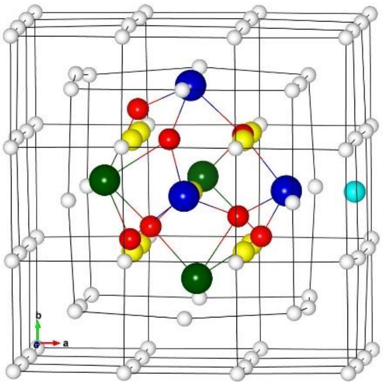

4. He in the O-Y-Ti cluster with oxygen in the center (OC)

Fig. B4: The initial He sites considered for the calculation of the He interaction with the O-Y-Ti cluster with oxygen in the center (OC). White, green, blue and red balls represent Fe, Y, Ti and O, respectively. Gray and magenta balls denote octahedral and tetrahedral interstitial sites in the underlying bcc lattice. Light green balls are vacant sites at the cluster-iron interface. Vacancies that belong to the cluster are represented by yellow balls. Purple balls show possible sites for an additional vacancy and an additional self-interstitial atom (see sections *App-B4* and *App-B5*).

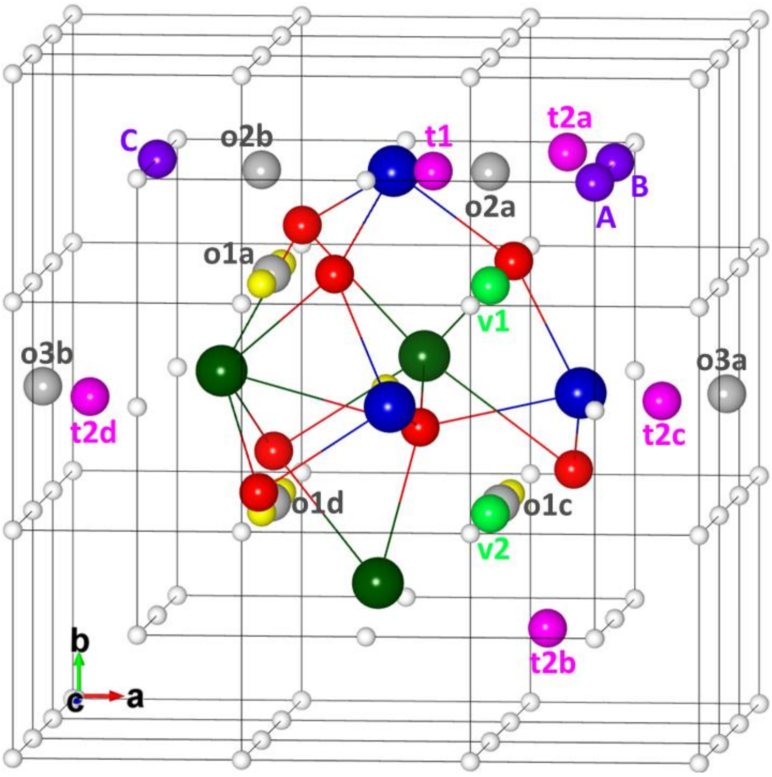

The following figures show relaxed configurations.

Fig. B4a: He is on IVS near v1 or v2

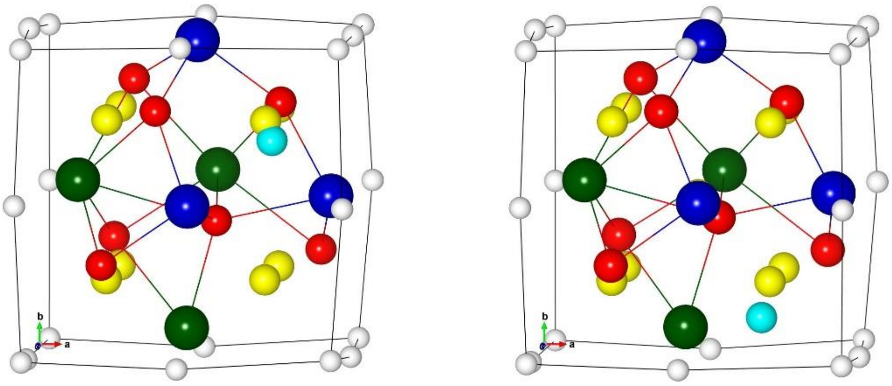

v1 (-2.39, 2.17)

v2 (-2.18, 2.37)

Relaxation to an IVS position close to v1:

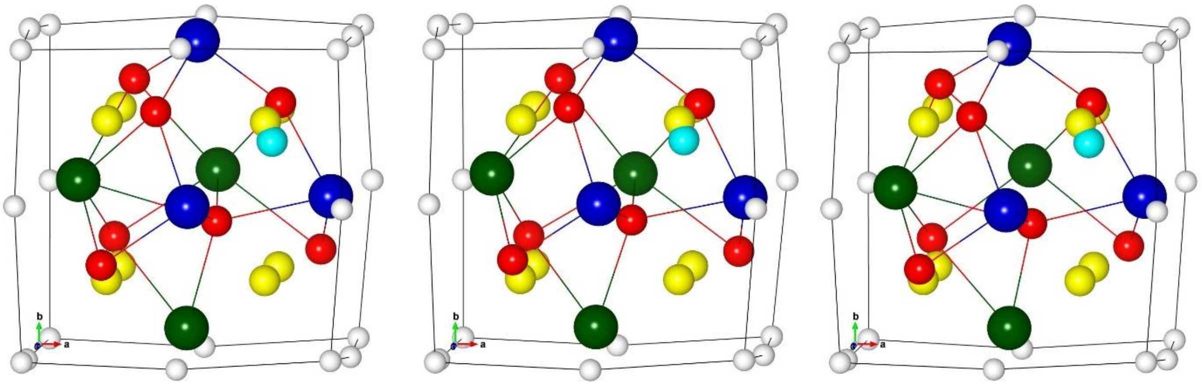

o2a (-2.39, 2.17)

t1 (-2.39, 2.17)

t2c (-2.39, 2.17)

Fig. B4b: Relaxation to IIS

He relaxes to an IIS close to the octahedron face with 2 Ti and one Y on the corners.

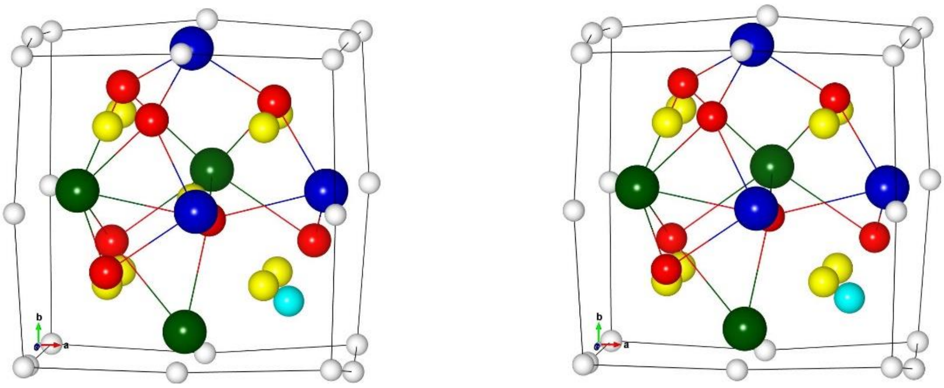

o1c (-2.34, 2.21)

t2b (-2.34, 2.21)

The sites o1a, o1d, o2b, o3a, o3b, t2a, and t2d are not stable: He relaxes to different IIS configurations.

o1a (-1.99, 2.55)

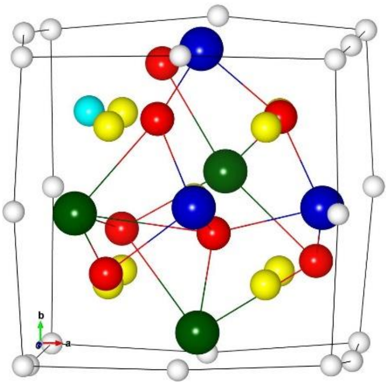

o1d (-2.68, 1.87)

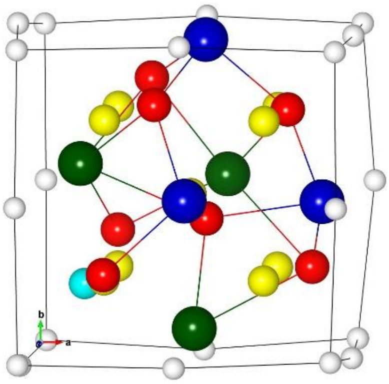

o2b (-1.80, 2.75)

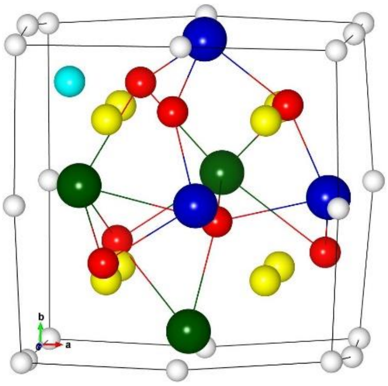

o3a (-1.94, 2.60)

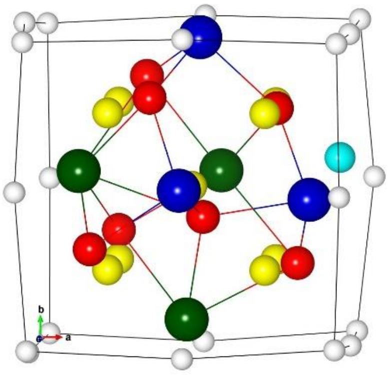

o3b (-2.64, 1.91)

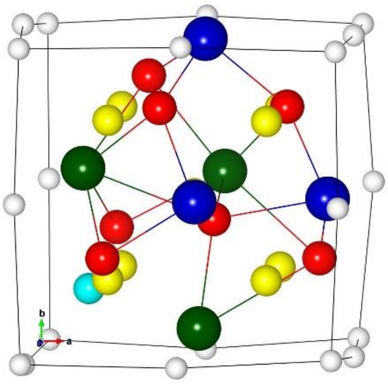

t2a (-2.47, 2.07)

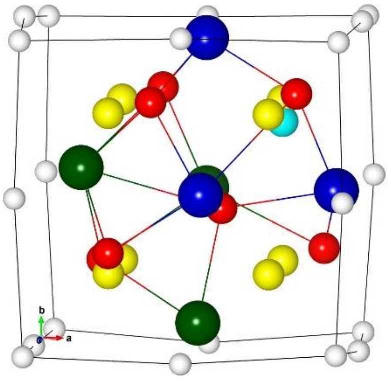

t2d (-2.64, 1.91)

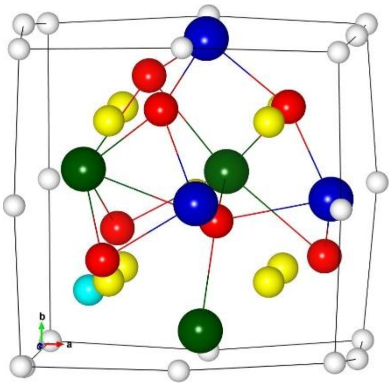

App-B2: Relaxed cluster configurations containing two He atoms

In the following the cyan balls are the two He atoms. Figures on the left side depict the cluster with the initial He sites and on the right side the relaxed configuration is shown. White, green, blue, and red balls represent Fe, Y, Ti, and O, respectively. Vacancies which belong to the cluster are represented by yellow balls. The values of He binding and incorporation energy are given in the form (E_b^{2He} , E_{incorp}^{2He}). All values are in eV. Only parts of the supercell are shown in the figures.

5. Two He in the CL O-Y cluster

Fig. B5a:

Initial configuration: He at center and on an IVS, both He sites correspond to relaxed configurations obtained by adding one He to the cluster.

Relaxed configuration: (-6.51, 2.61)

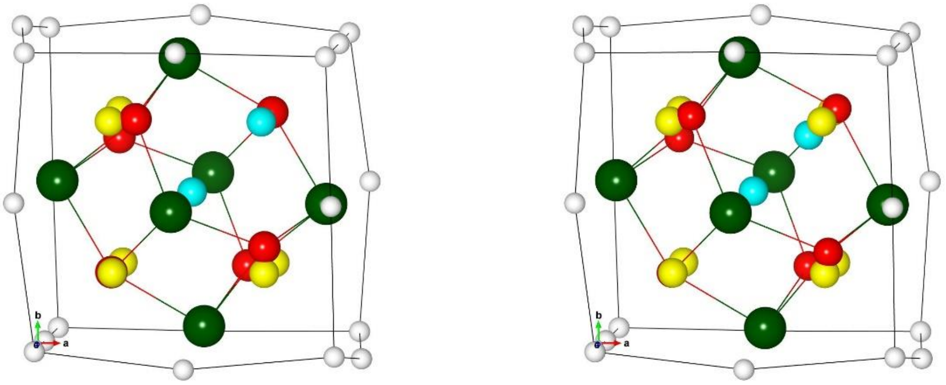

Fig. B5b:

Initial configuration: He on the two available IVS, both He sites correspond to relaxed configurations obtained by adding one He to the cluster.

Relaxed configuration: (-6.33, 2.79)

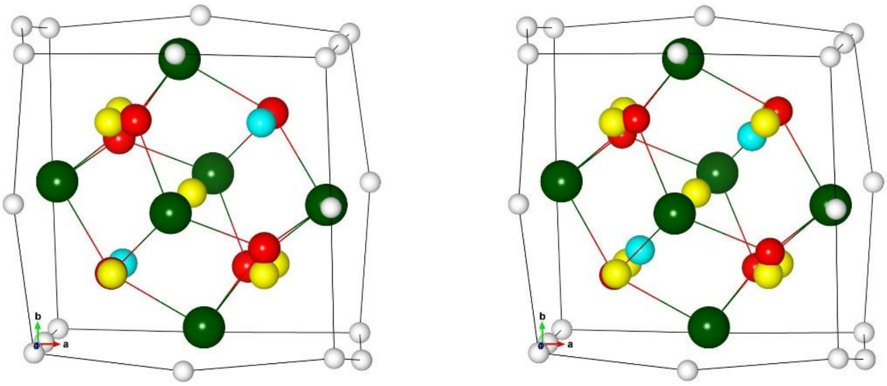

Fig. B5c:

Initial configuration: He at center and on an IIS near a octahedron edge with two Y on the corner and two O and two v in the environment, both He sites correspond to relaxed configurations obtained by adding one He to the cluster.

Relaxed configuration: (-5.32, 3.79)

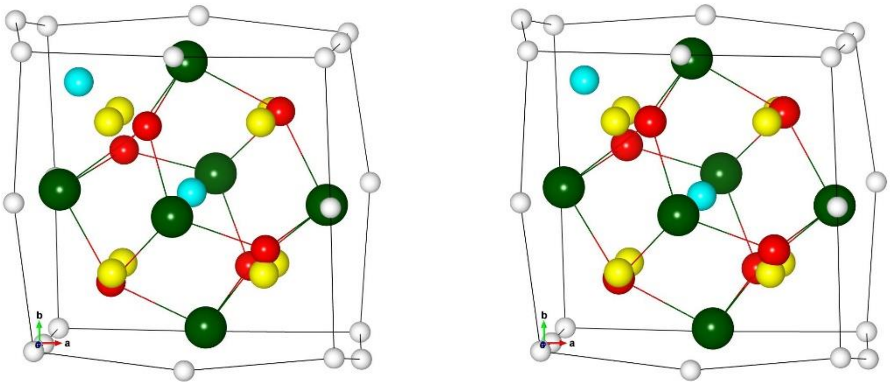

Fig. B5d :

Initial configuration: Two He atoms are placed symmetrically close to v1 with orientation along the <100> direction

Relaxed configuration: (-5.43, 3.69)

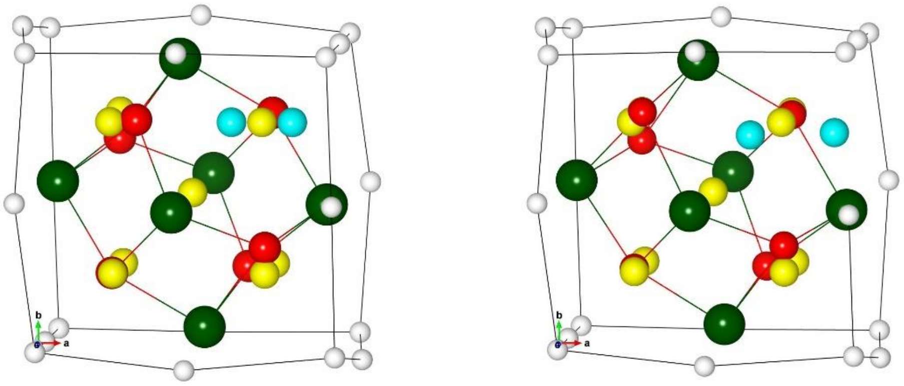

Initial configuration: Two He atoms are placed symmetrically close to v1 with orientation along the <110> direction

Relaxed configuration: (-5.11, 4.01)

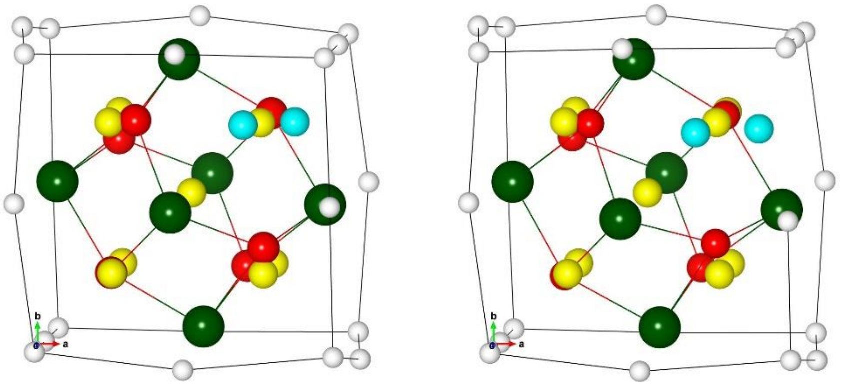

6. Two He in the OC O-Y cluster

Fig. B6a:

Initial configuration: He on two IVS (near v2 and v3), both He sites correspond to relaxed configurations obtained by adding one He to the cluster.

Relaxed configuration: (-5.51, 3.60)

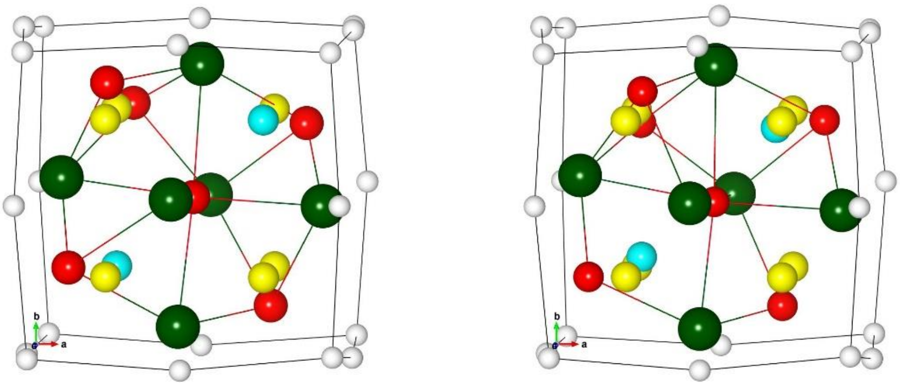

Initial configuration: He on two IVS (near v1 and v3), both He sites correspond to relaxed configurations obtained by adding one He to the cluster

Relaxed configuration: (-5.39, 3.71)

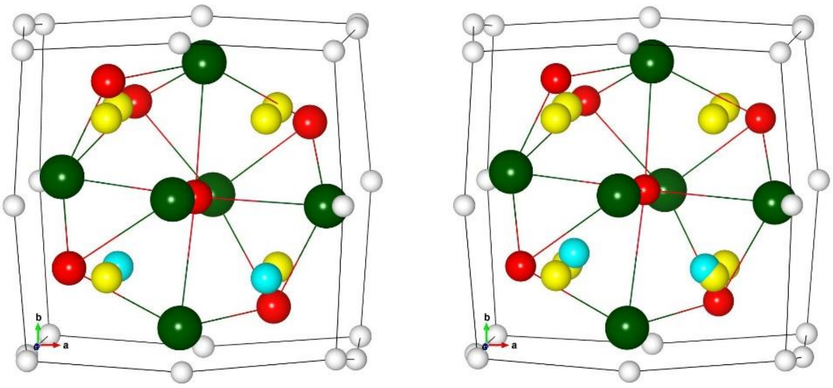

Fig. B6b:

Initial configuration: He on the IVS near v2 and one He on an IIS close to two Y on an octahedron edge, both He sites correspond to relaxed configurations obtained by adding one He to the cluster.

Relaxed configuration: (-4.92, 4.18)

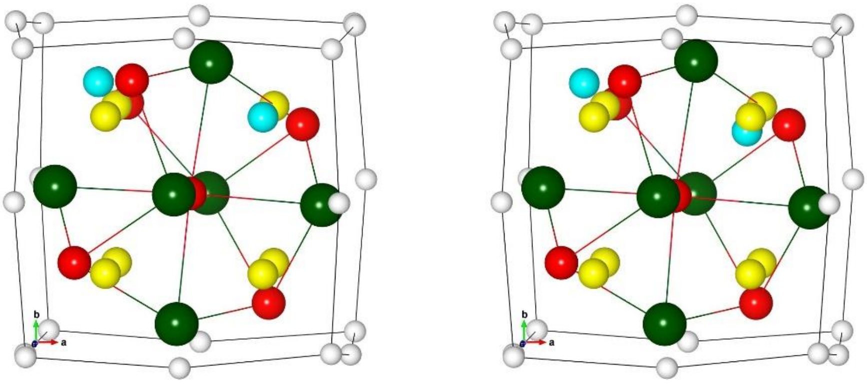

Initial configuration: Two He atoms are placed symmetrically close to v1 with orientation along the <100> direction

Relaxed configuration: (-5.27, 3.83)

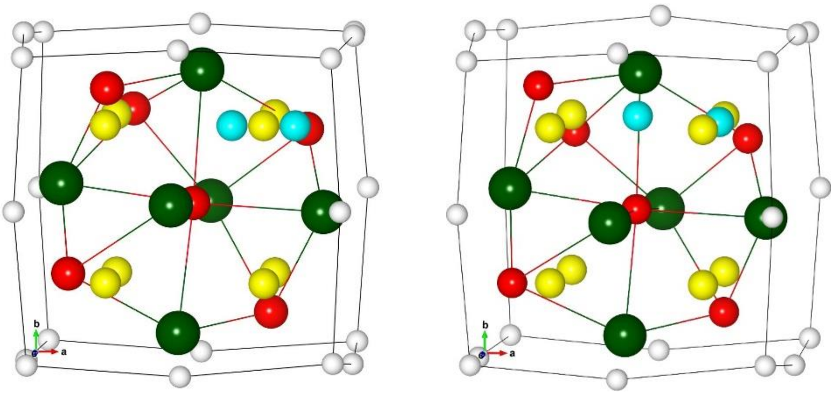

7. Two He in the CL O-Y-Ti cluster

Fig. B7a:

Initial configuration: He at center and on an IVS, both He sites correspond to relaxed configurations obtained by adding one He to the cluster.

Relaxed configuration: (-5.18, 3.93)

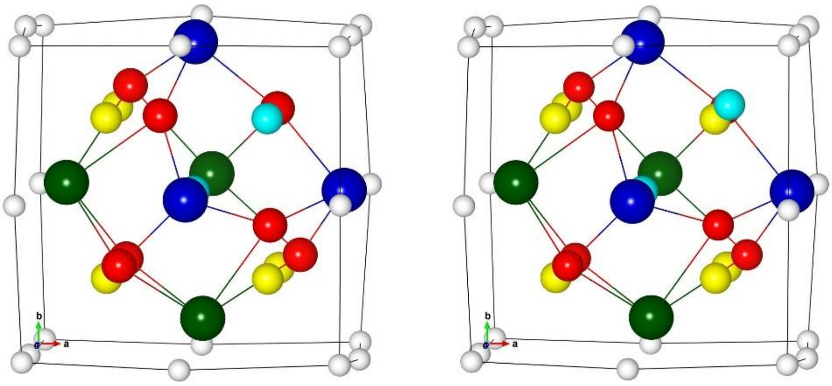

Fig. B7b:

Initial configuration: He at center and on t2d

Relaxed configuration: (-5.42, 3.69),

t2d is relaxed to an IIS close to the two Y at the edge of the octahedron

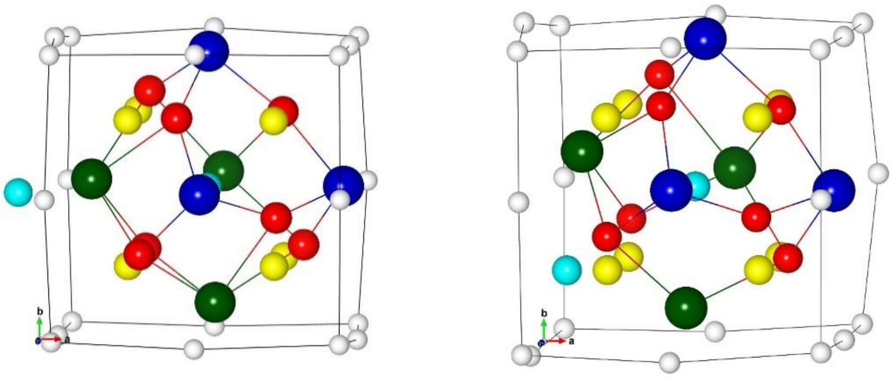

Fig. B7c:

Initial configuration: Two He atoms are placed symmetrically close to v1 with orientation along the <100> direction

Relaxed configuration: (-3.87, 5.23)

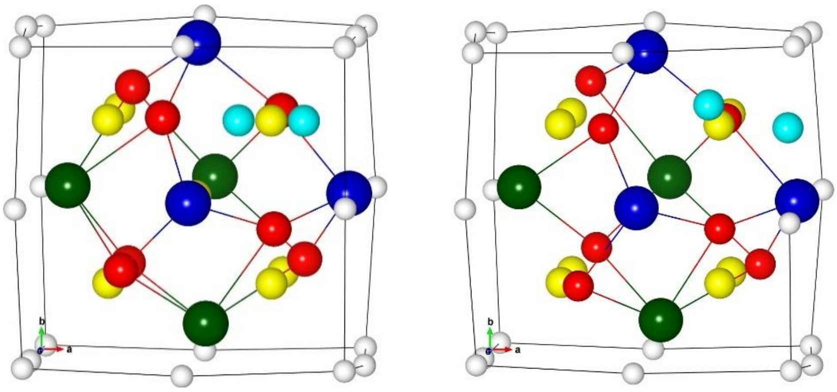

Initial configuration: Two He atoms are placed symmetrically close to v1 with orientation along the <110> direction

Relaxed configuration: (-3.84, 5.27)

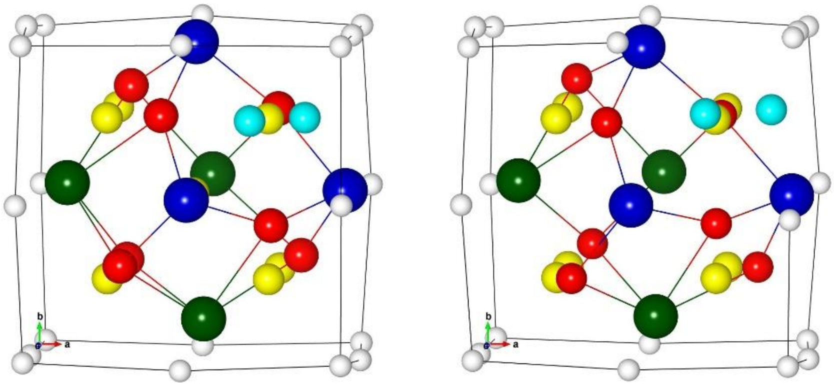

8. Two He in the OC O-Y-Ti cluster

Fig. B8a:

Initial configuration: He on the two available IVS, both He sites correspond to relaxed configurations obtained by adding one He to the cluster.

Relaxed configuration: (-4.69, 4.41)

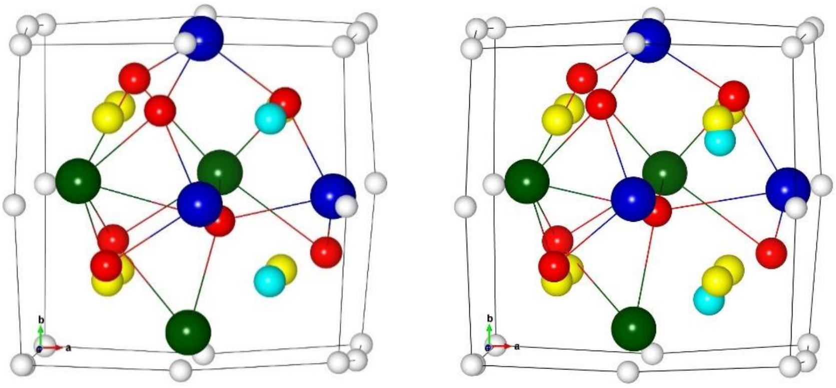

Fig. B8b:

Initial configuration: Two He atoms are placed symmetrically close to v2 with orientation along the <110> direction

Relaxed configuration: (-4.78, 4.32)

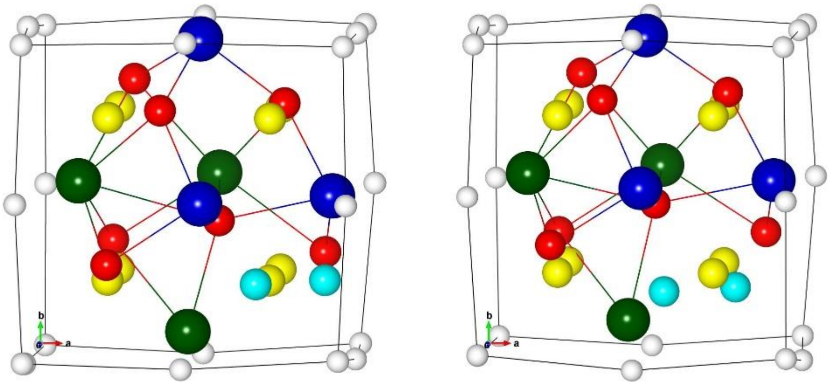

Initial configuration: Two He atoms are placed symmetrically close to v1 with orientation along the <100> direction

Relaxed configuration: (-5.31, 3.80)

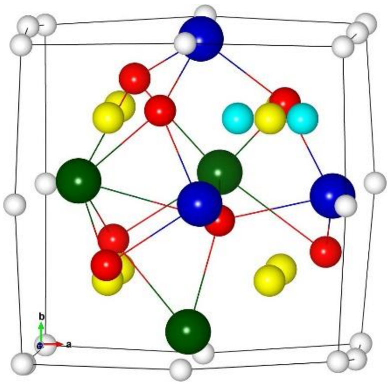

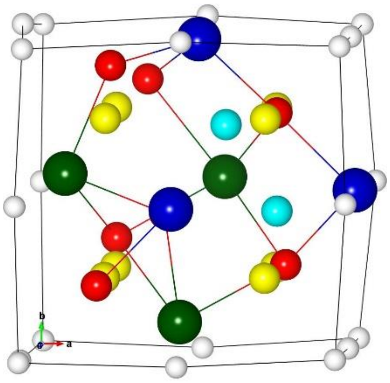

App-B3: Relaxed cluster configurations containing three He atoms

In the following the cyan balls are the three He atoms. Figures on the left side depict the cluster with the initial He sites and on the right side the relaxed configuration is shown. White, green, blue, and red balls represent Fe, Y, Ti, and O, respectively. Vacancies which belong to the cluster are represented by yellow balls. The values of He binding and incorporation energy are given in the form $(E_b^{3He}, E_{incorp}^{3He})$. All values are in eV. Only parts of the supercell are shown in the figures.

9. Three He in the CL O-Y cluster

Fig. B9a:

Initial configuration: He at center and on two IVS; these three He sites correspond to relaxed configurations obtained by adding one He to the cluster.

Relaxed configuration: (-9.68, 3.99)

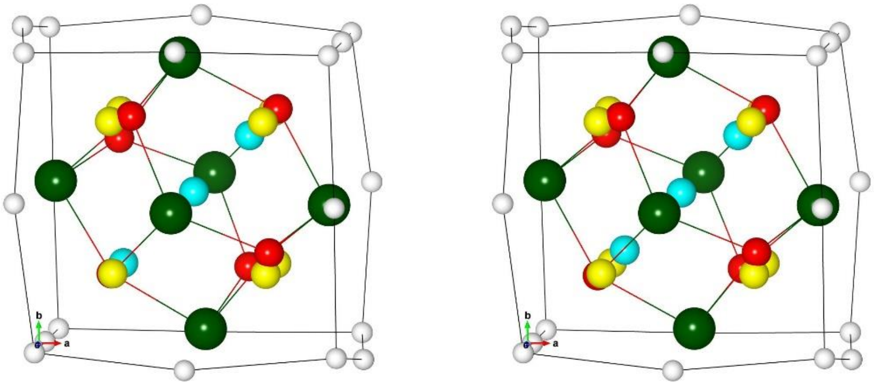

Fig. B9b:

Initial configuration: The first He is at the center, the second on an IVS, and the third on a IIS close to the two Y atoms at the corner of an octahedron edge; these three He sites correspond to relaxed configurations obtained by adding one He to the cluster

Relaxed configuration: (-8.50, 5.18)

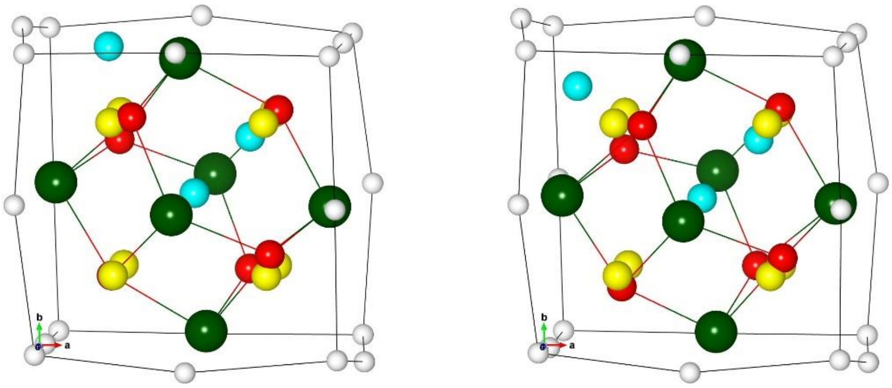

Fig. B9c:

Initial configuration: 3 He symmetrical to v1 in a {100} plane

Relaxed configuration: (-8.41, 5.26)

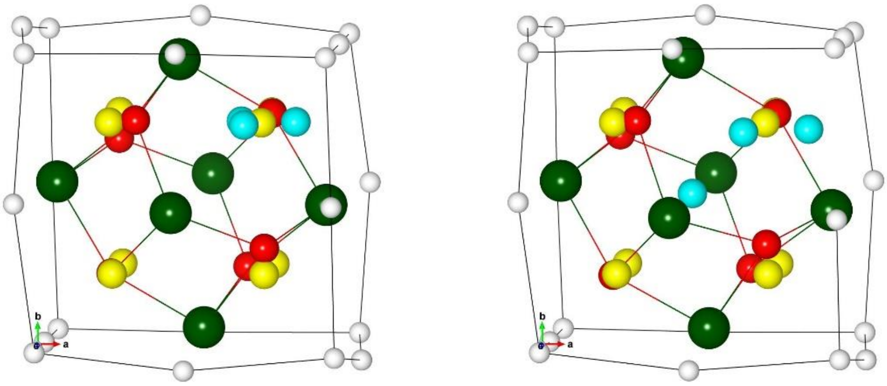

10. Three He in the OC O-Y cluster

Fig. B10a:

Initial configuration: He on the three available IVS; these three He sites correspond to relaxed configurations obtained by adding one He to the cluster

Relaxed configuration: (-8.11, 5.54)

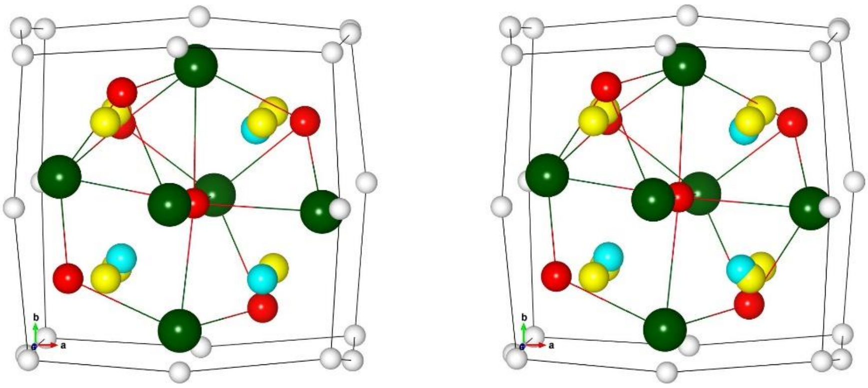

Fig. B10b:

Initial configuration: Two He on IVS near v2 and near v3, the third He on an IIS close to the two Y atoms at the corner of an octahedron edge (with two O atoms in the environment); these three He sites correspond to relaxed configurations obtained by adding one He to the cluster

Relaxed configuration: (-7.61, 6.05)

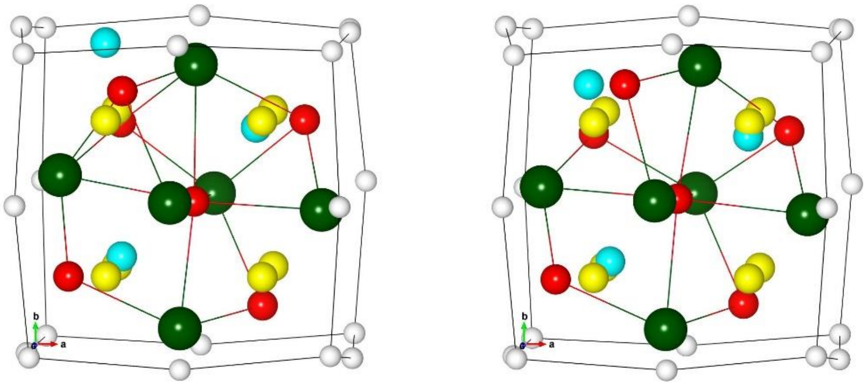

Fig. B10c :

Initial configuration: Three He atoms in a {100} plane, symmetric, near v2

Relaxed configuration: (-7.97, 5.69)

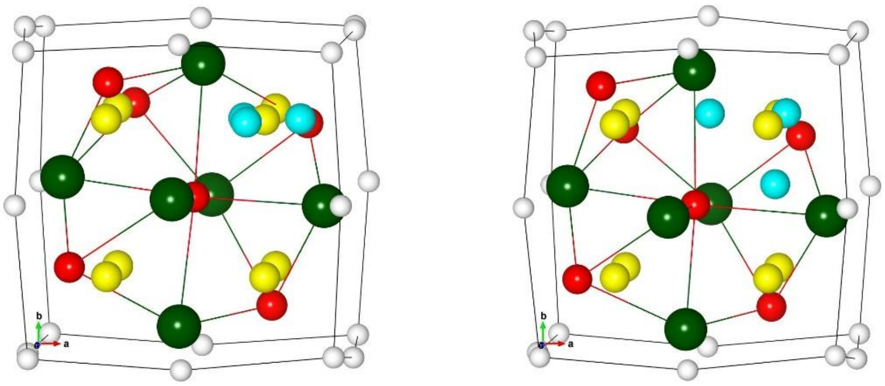

11. Three He in the CL O-Y-Ti cluster

Fig. B11a:

Initial configuration: He at center, on IVS near v1, and on o2b

Relaxed configuration: (-7.82, 5.84)

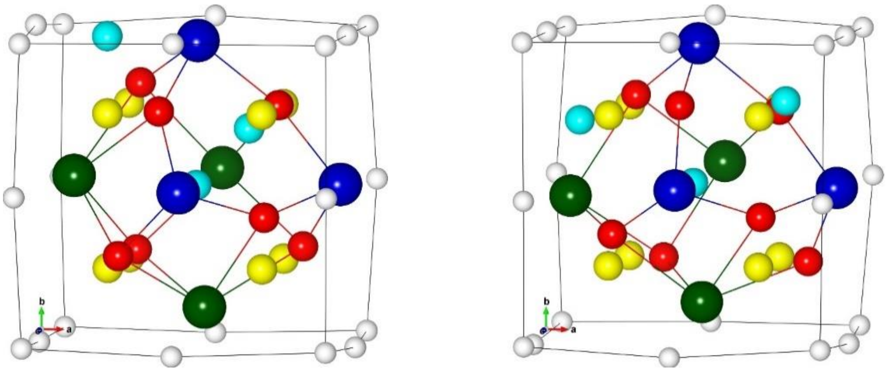

Fig. B11b:

Initial configuration: Three He atoms in a {100} plane, symmetric, near v1

Relaxed configuration: (-5.23, 8.44)

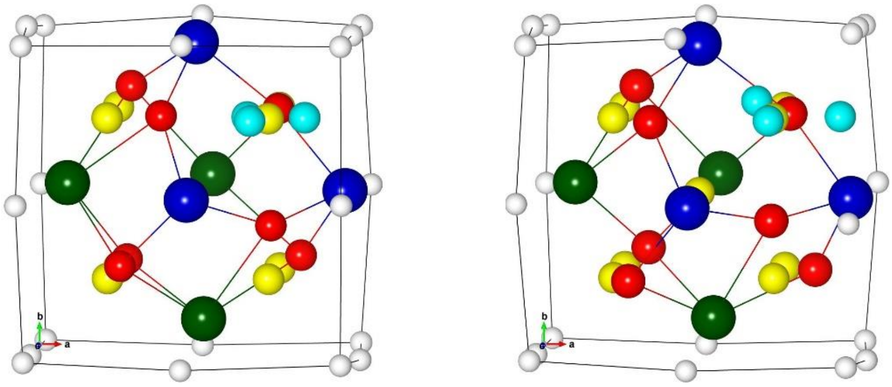

12. Three He in the OC O-Y-Ti cluster

Fig. B12a:

Initial configuration: Two He on IVS near v1 and v2, and a third He on o2b

Relaxed configuration: (-6.89, 6.77)

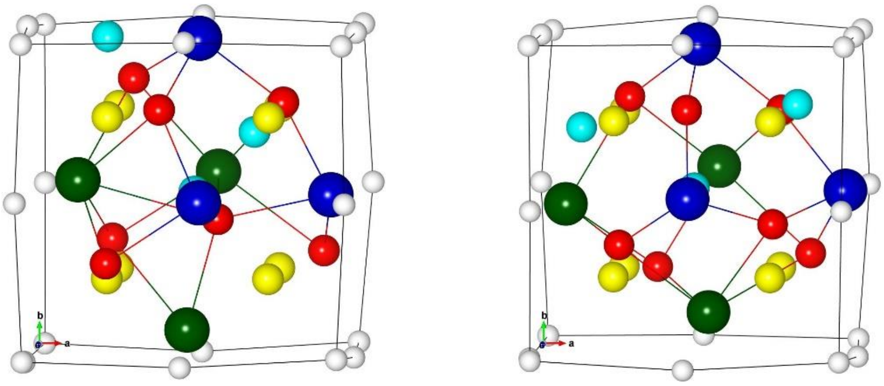

Fig. B12b:

Initial configuration: Three He atoms in a {100} plane, symmetric, near v1

Relaxed configuration: (-6.16, 7.50)

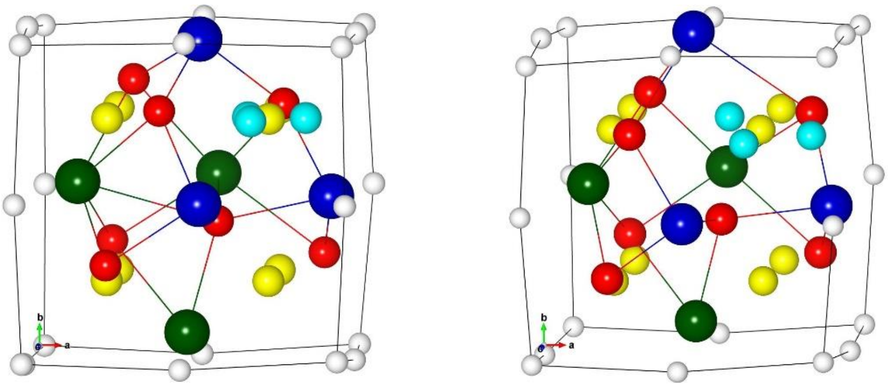

App-B4: Relaxed cluster configurations with an additional vacancy (v)

In the following, the magenta ball is the additional vacancy. Figures on the left side depict the cluster with the initial v site and on the right side the relaxed configuration is shown. White, green, blue, and red balls represent Fe, Y, Ti, and O, respectively. Yellow balls represent vacancies, which belong to the cluster. The values of v binding and incorporation energy are given in the form (E_b^V , E_{incorp}^V). All values are in eV. Only parts of the supercell are shown in the figures.

13. Extra vacancy in the environment of the CL O-Y cluster

Fig. B13:

Initial configuration: v on site A

Relaxed configuration: (-0.076, 2.09)

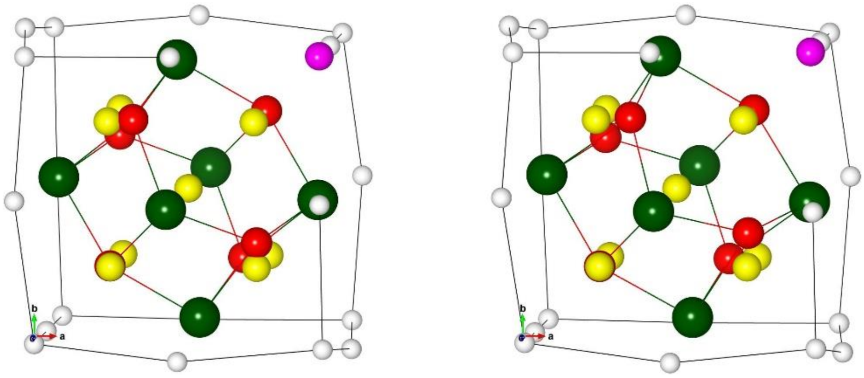

Initial configuration: v on site B

Relaxed configuration: (-0.79, 1.38)

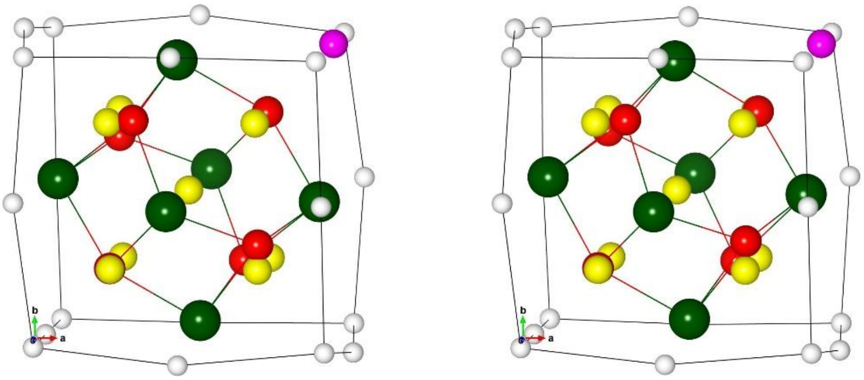

Initial configuration: *v* on site C

Relaxed configuration: (-1.99, 0.18)

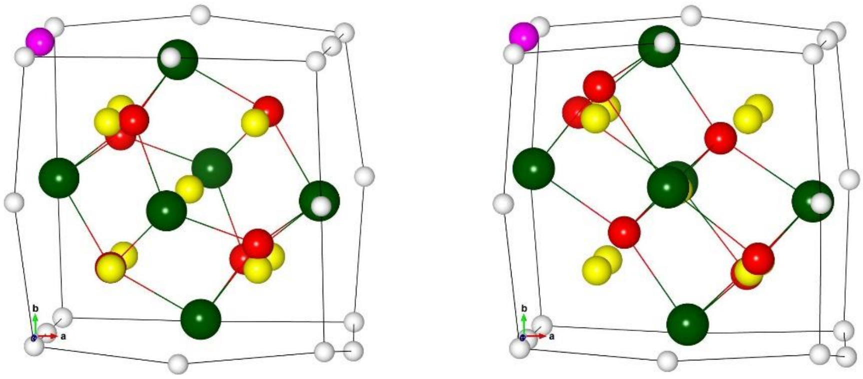

14. Extra vacancy in the environment of the OC O-Y cluster

Fig. B14:

Initial configuration: v on site A

Relaxed configuration: (-0.012, 2.15)

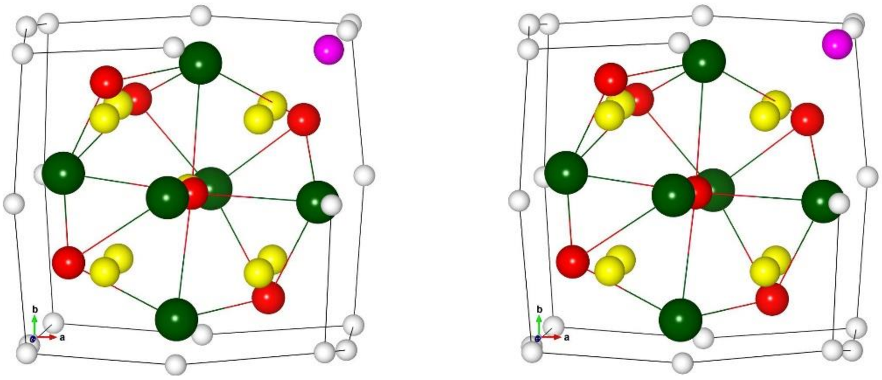

Initial configuration: v on site B

Relaxed configuration: (-1.06, 1.11)

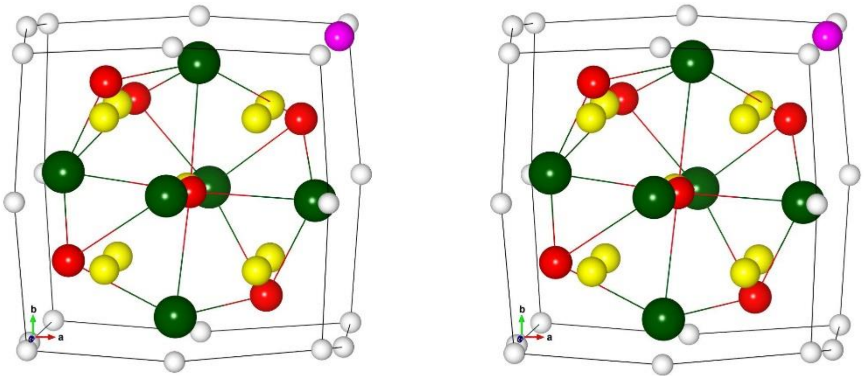

Initial configuration: v on site C

Relaxed configuration: (-1.97, 0.20)

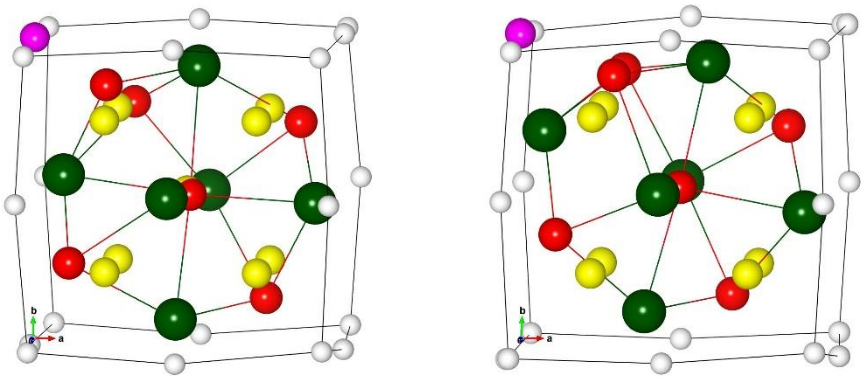

15. Extra vacancy in the environment of the CL O-Y-Ti cluster

Fig. B15:

Initial configuration: v on site A

Relaxed configuration: (-0.24, 1.93)

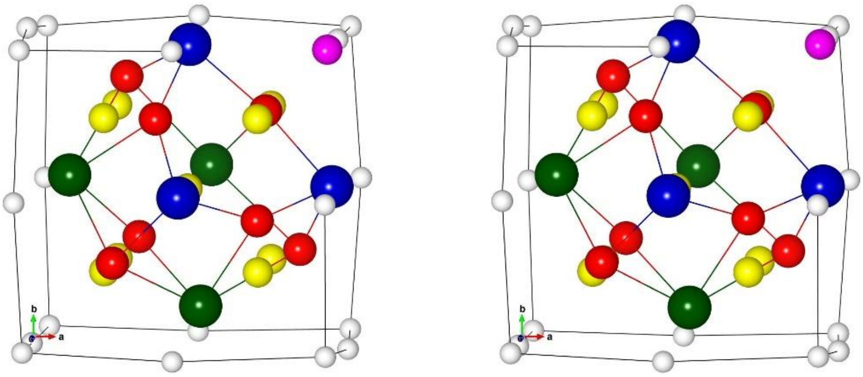

Initial configuration: v on site B

Relaxed configuration: (-0.40,1.77)

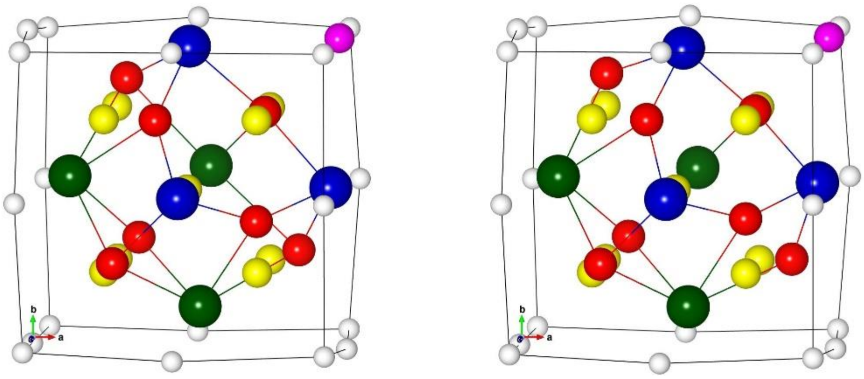

Initial configuration: v on site C

Relaxed configuration: (-1.85, 0.32)

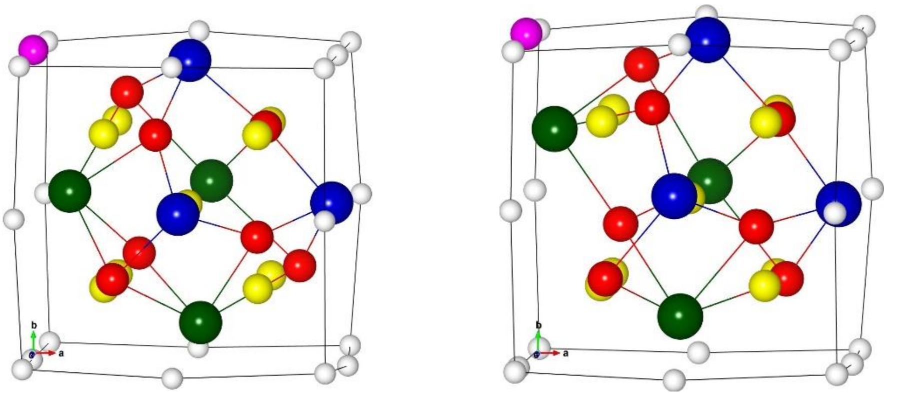

16. Extra vacancy in the environment of the OC O-Y-Ti cluster

Fig. B16:

Initial configuration: v on site A

Relaxed configuration: (-0.16, 2.00)

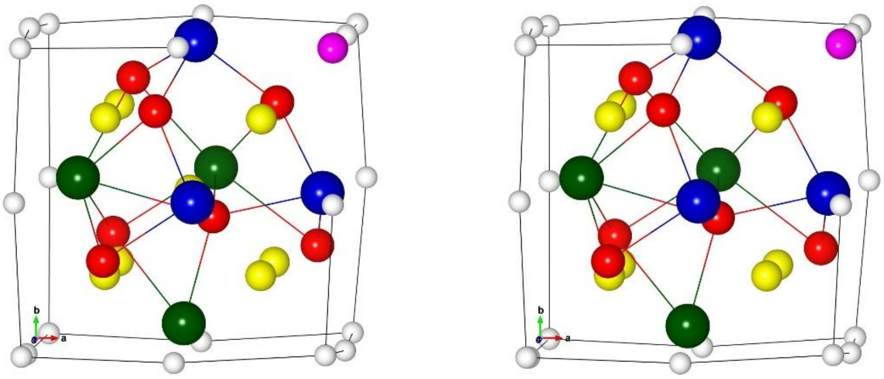

Initial configuration: v on site B

Relaxed configuration: (-0.98,1.19)

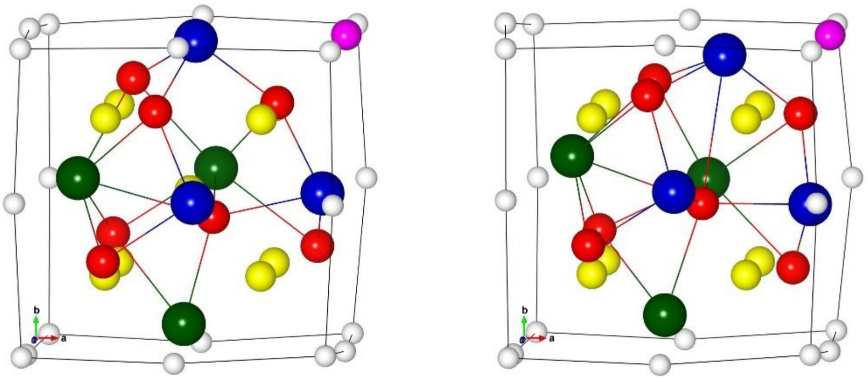

Initial configuration: v on site C
Relaxed configuration: (-1.73, 0.43)

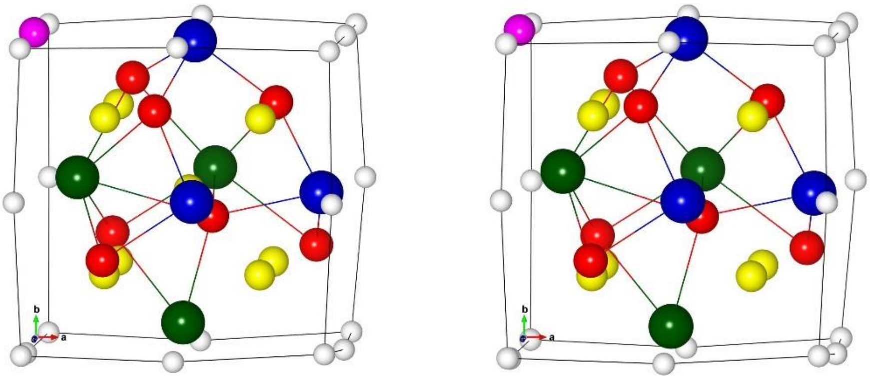

App-B5: Relaxed cluster configurations with an additional self-interstitial atom (SIA)

In the following, the two light magenta balls are the atoms of the dumbbell which forms the SIA. Figures on the left side depict the cluster with the initial SIA site and on the right side the relaxed configuration is shown. White, green, blue, and red balls represent Fe, Y, Ti, and O, respectively. Yellow balls represent vacancies, which belong to the cluster. The values of SIA binding and incorporation energy are given in the form (E_b^{SIA} , E_{incorp}^{SIA}). All values are in eV. Only parts of the supercell are shown in the figures.

17. SIA in the environment of the CL O-Y cluster

Fig. B17:

Initial configuration: SIA on site A

Relaxed configuration: (-3.50, 0.42), recombination with a v of the cluster

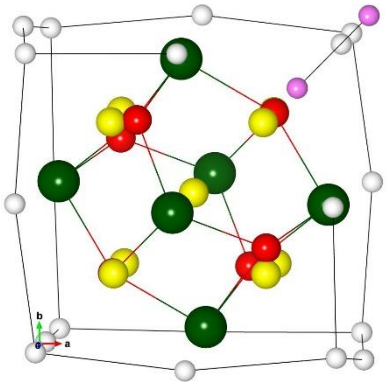

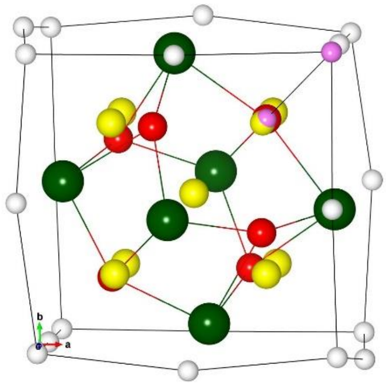

Initial configuration: SIA on site B

Relaxed configuration: (-4.19, -0.27), recombination with a v of the cluster

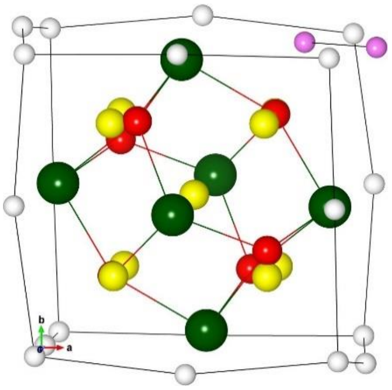

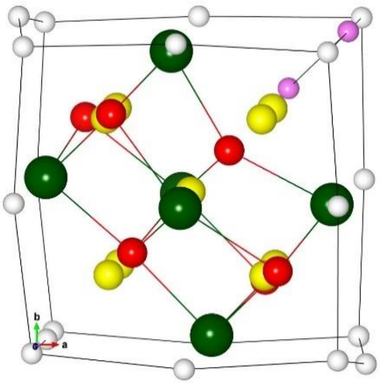

Initial configuration: SIA on site C

Relaxed configuration: (-2.98, 0.94), recombination with a v of the cluster

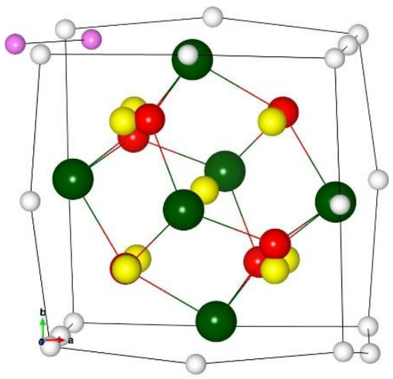

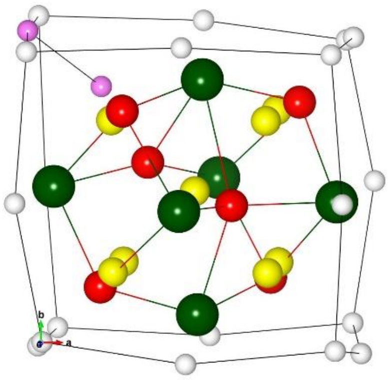

18. SIA in the environment of the OC O-Y cluster

Fig. B18:

Initial configuration: SIA on site A

Relaxed configuration: (-3.70, 0.22), recombination with a v of the cluster

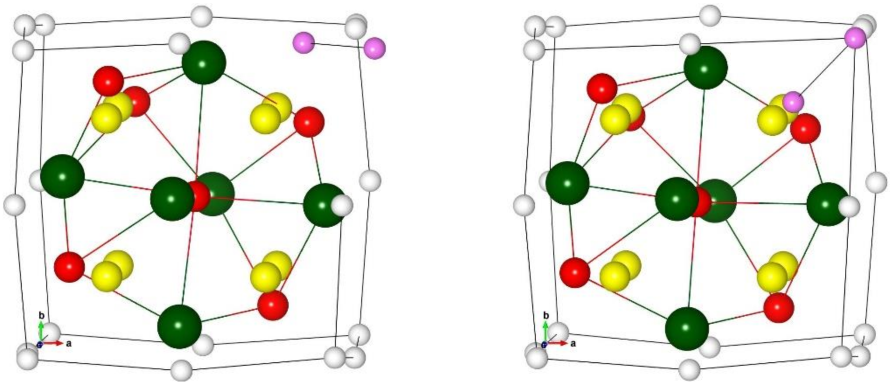

Initial configuration: SIA on site B

Relaxed configuration: (-2.08, 1.84), recombination with a v of the cluster

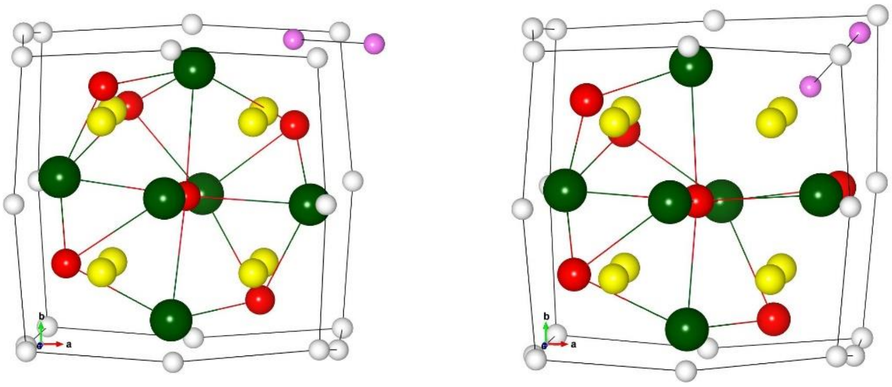

Initial configuration: SIA on site C

Relaxed configuration: (-1.91, 2.00), recombination with a v of the cluster

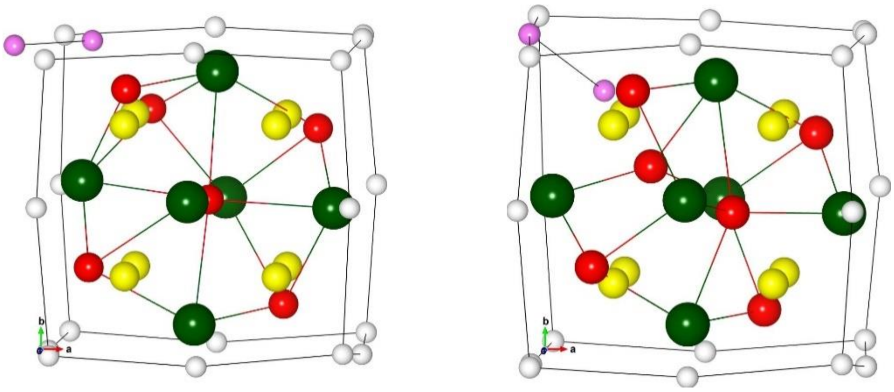

19. SIA in the environment of the CL O-Y-Ti cluster

Fig. B19:

Initial configuration: SIA on site A

Relaxed configuration: (-3.41, 0.51), recombination with a v of the cluster

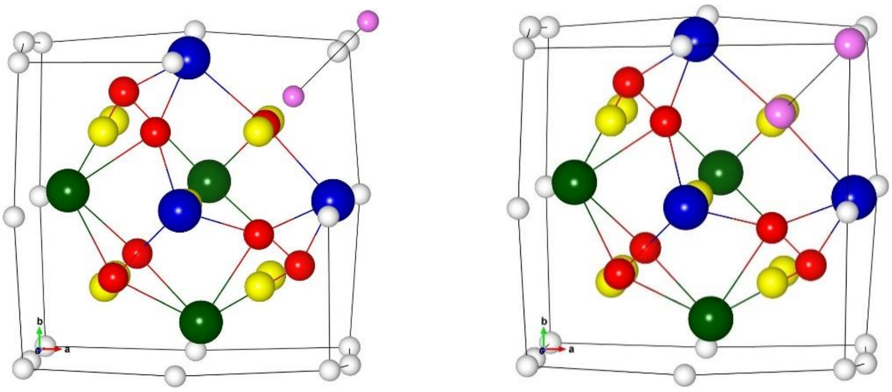

Initial configuration: SIA on site B

Relaxed configuration: (-3.89, 0.029), recombination with a v of the cluster

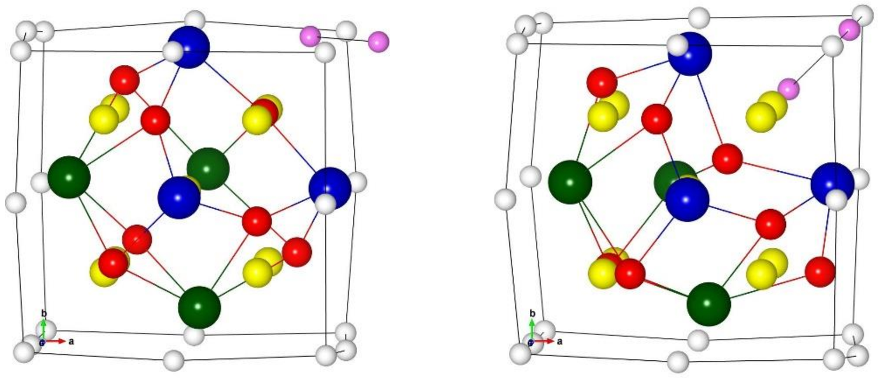

Initial configuration: SIA on site C

Relaxed configuration: (-3.58, 0.33), recombination with a v of the cluster

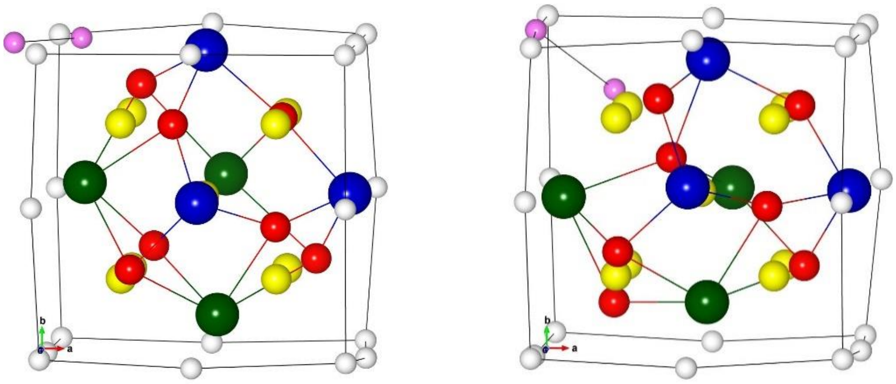

20. SIA in the environment of the OC O-Y-Ti cluster

Fig. B20:

Initial configuration: SIA on site A

Relaxed configuration: (-3.55, 0.36), recombination with a v of the cluster

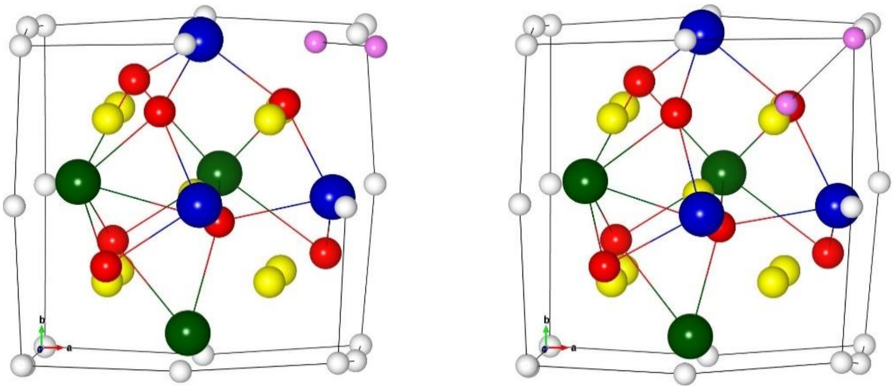

Initial configuration: SIA on site B

Relaxed configuration: (-4.21, -0.30), recombination with a v of the cluster

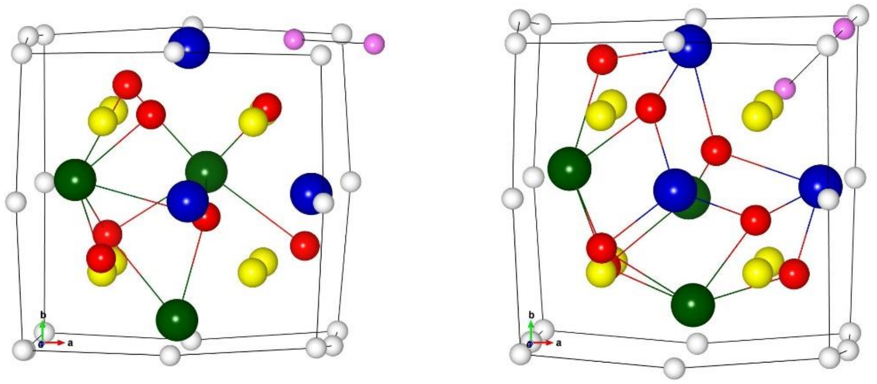

Initial configuration: SIA on site C

Relaxed configuration: (-3.98, -0.061), recombination with a v of the cluster

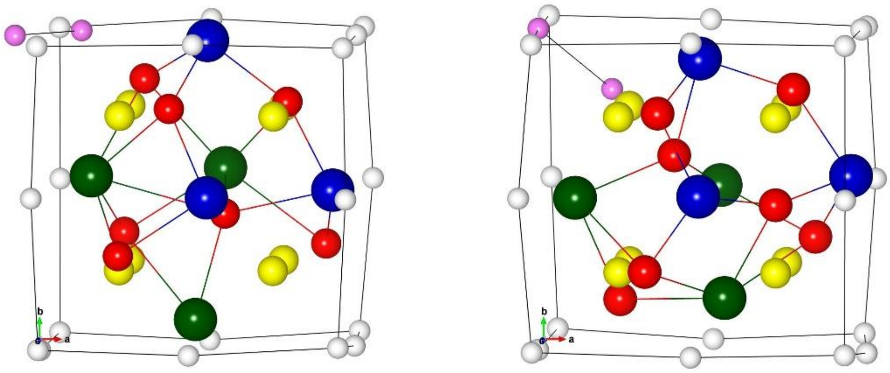

App-B6: Relaxed cluster configurations containing one He atom in a supercell with 250 bcc lattice sites

In all following figures, the cyan ball represents the He atom. The values of He binding and incorporation energy are given in the form (E_b^{He} , E_{incorp}^{He}). All values are in eV. Only parts of the supercell are shown in the figures.

21. He in the cage-like (CL) O-Y cluster

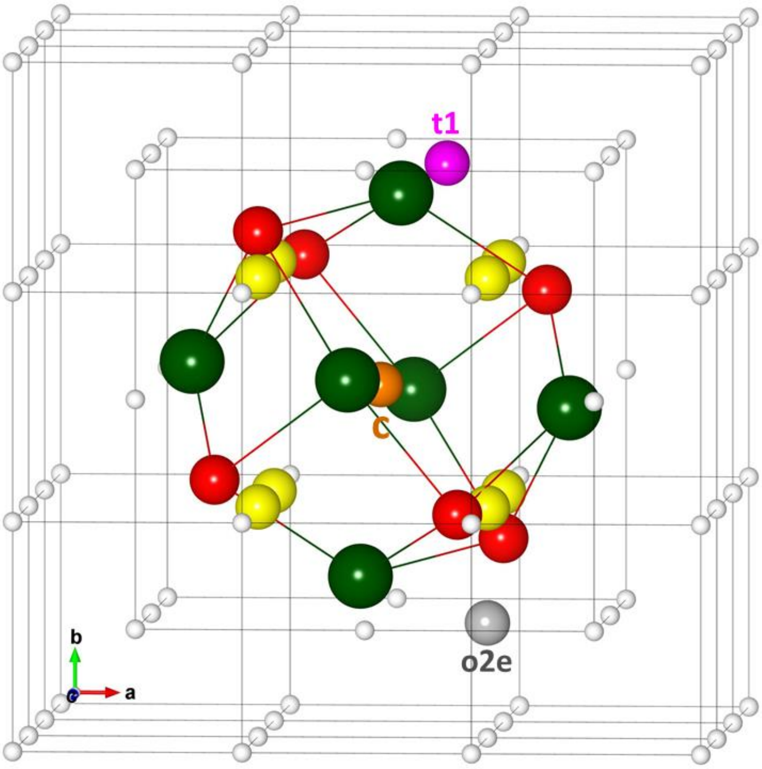

Fig. B21: The initial He sites considered for the calculation of He interaction with the CL O-Y cluster White, green, and red balls represent Fe, Y, and O, respectively. Gray and magenta balls denote octahedral and tetrahedral interstitial sites in the underlying bcc lattice. The gold ball denotes the vacant site at the cluster center. Vacancies which belong to the cluster are represented by yellow balls

The following figures show relaxed configurations

Fig. B21a: He at the center of cluster stays there.

center (-3.29, 1.23)

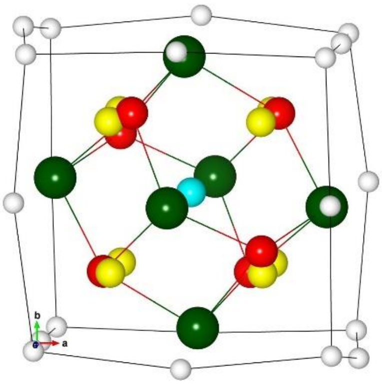

Fig. B21b: He on t1 relaxes to an interfacial vacant site (IVS).

t1 (-3.21, 1.31)

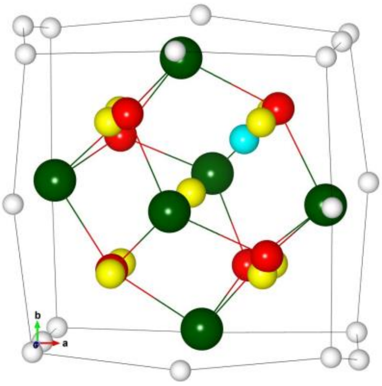

Fig. B21c: o2e relaxes to a cluster configuration with oxygen in the center (OC), with He on a IVS close to a vacancy position. Here He binding and incorporation energies were determined with OC cluster without He as reference.

o2e (-2.57, 1.93)

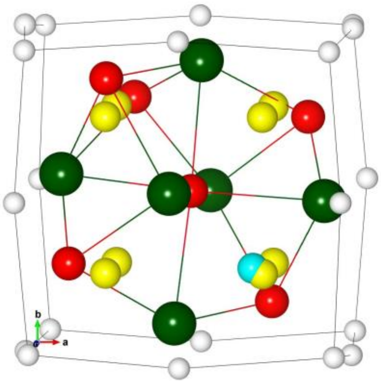

22. He in the O-Y cluster with oxygen in the center (OC)

Fig. B22: The initial He sites considered for the calculation of He interaction with the O-Y cluster with oxygen in the center (OC). White, green, and red balls represent Fe, Y, and O, respectively. Gray and magenta balls denote octahedral and tetrahedral interstitial sites in the underlying bcc lattice. The light green ball is a vacant site at the cluster-iron interface. Vacancies which belong to the cluster are represented by yellow balls.

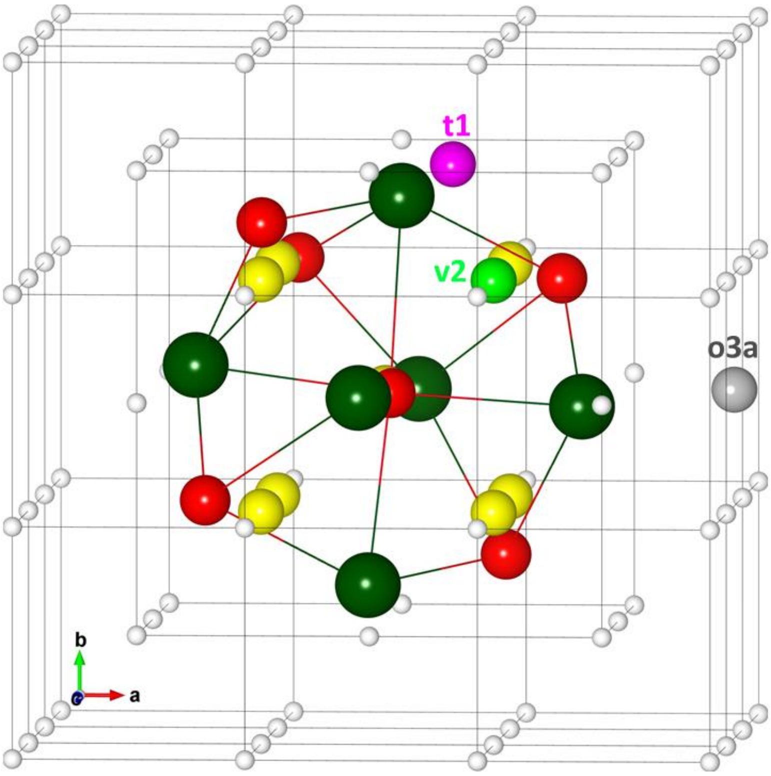

The following figures show relaxed configurations.

Fig. B22a: He on v2 and on t1, and o3a relaxes to a interfacial vacant site (IVS)

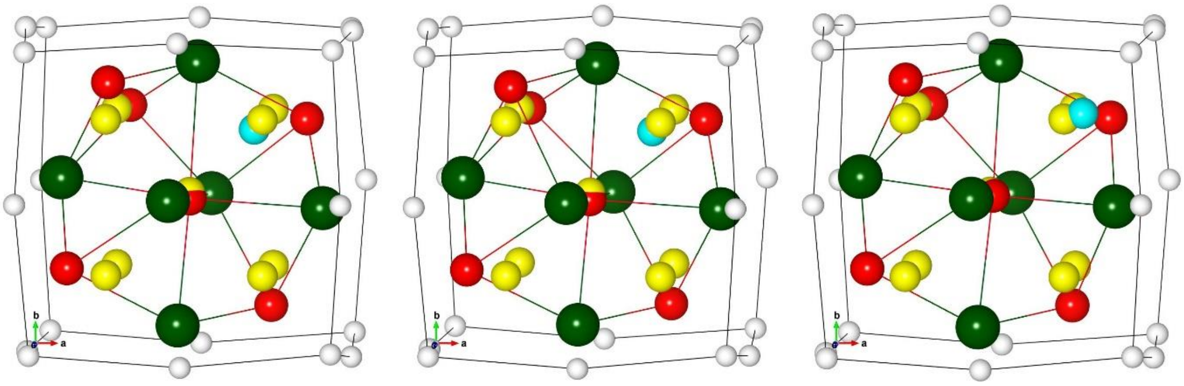
v2 (-2.69, 1.83) t1 (-2.69, 1.83) o3a (-2.61, 1.91)

23. He in the cage-like (CL) O-Y-Ti cluster

Fig. B23: The initial He sites considered for the calculation of He interaction with the CL O-Y-Ti cluster. White, green, blue and red balls represent Fe, Y, Ti and O, respectively. The gray ball denotes an octahedral interstitial site in the underlying bcc lattice. Gold and light green balls are vacant sites at the cluster center and the cluster-iron interface. Vacancies which belong to the cluster are represented by yellow balls.

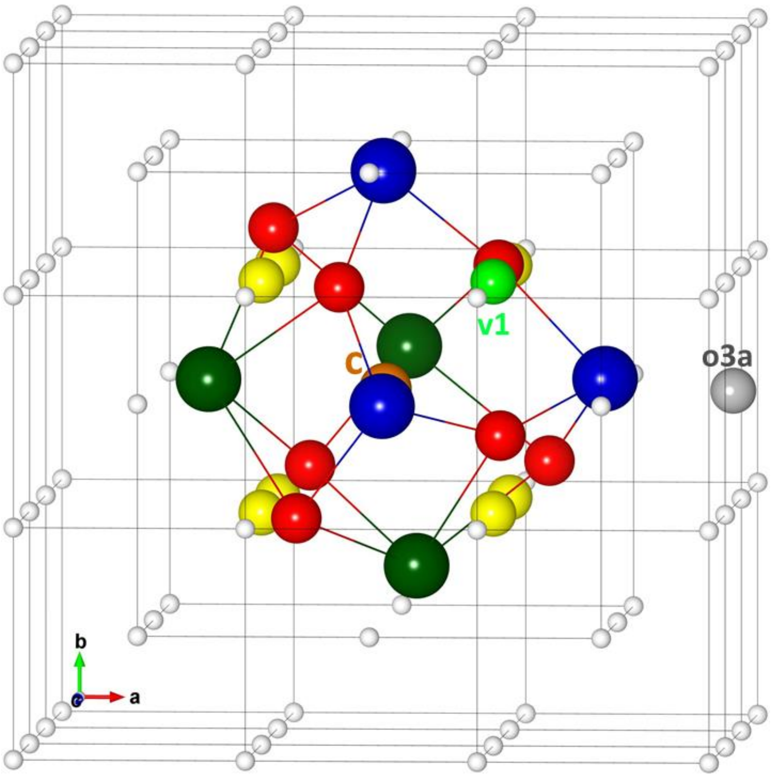

The following figures show relaxed configurations

Fig. B23a: He at the center of cluster stays there.
center (-2.59, 1.93)

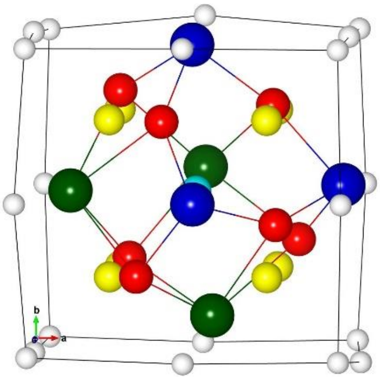

Fig. B23b: He on v1 relaxes to a nearby IVS.
v1 (-2.37,   2.15)

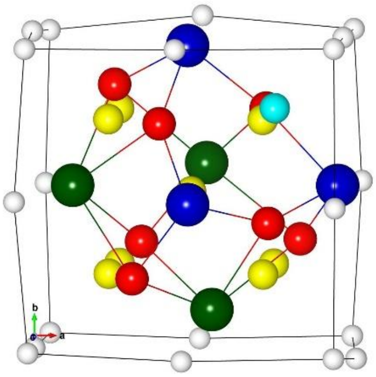

Fig. B23b: He is on a stable near the initial interstitial sites.
o3a (-0.191, 4.33)

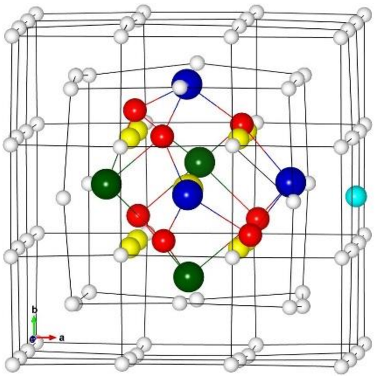

24. He in the O-Y-Ti cluster with oxygen in the center (OC)

Fig. B24: The initial He sites considered for the calculation of the He interaction with the O-Y-Ti cluster with oxygen in the center (OC). White, green, blue and red balls represent Fe, Y, Ti and O, respectively. The gray ball denotes an octahedral interstitial site in the underlying bcc lattice. Vacancies which belong to the cluster are represented by yellow balls.

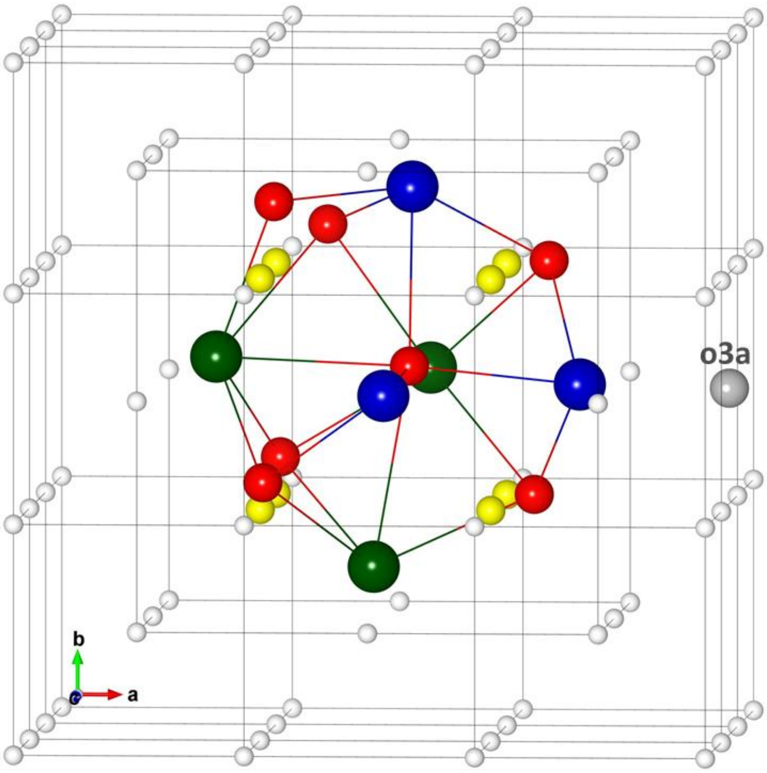

The following figure shows a relaxed configuration

Fig. B24a: He on o3a relaxes to an IIS.

o3a (-1.87, 2.65)

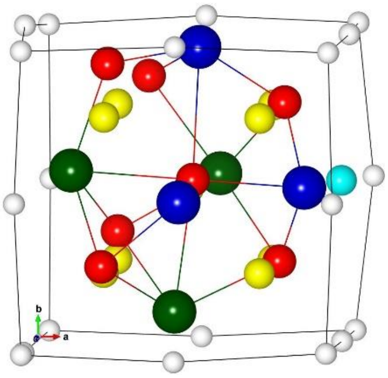

X ------------------------------ X

List of figures

List of tables

List of symbols

Symbol	Meaning
E_b^{mHe}	Binding energy of m He atoms
E_b^{O}	Binding energy of one oxygen atom
E_b^{V}	Binding energy of vacancy
E_b^{SIA}	Binding energy self-interstitial atom
$E_c[n(\vec{r})]$	Correlation functional
E_{cut}	Energy cutoff
$E^A\left(Fe\right)$	Energy per Fe atom
$E_x[n(\vec{r})]$	Exchange functional
E_f^{v}	Formation energy of vacancy
E_{incorp}^{SIA}	Incorporation energy of self-interstitial atom
E_{incorp}^{V}	Incorporation energy of vacancy
E_{bind}	Total binding energy
E^0	Total energy of bcc Fe
$E^A\left(He\right)$	Total energy He atom
E	Total energy of system
$E(X_i)$	Total energy of supercell containing monomer

e	Charge of electron
$\mathbf{F}_i$	Force on image
$\vec{G}$	Reciprocal lattice vector
K	Spring constant
m	Mass of electron
$\vec{k}$	Wave vector
$n(\vec{r})$	Electron density
n_{v}	Number of vacancies
$\vec{R}$	Lattice vector in real space
$\vec{r}$	Position vector
$T[n(\vec{r})]$	Density functional of the kinetic energy
$U[n(\vec{r})]$	Density functional of the electron-electron interaction
$V[n(\vec{r})]$	Density functional of the external potential
∇	Momentum operator
$\hbar$	Reduced Planks constant
ψ	Wave function
σ	Spin of electron
$\boldsymbol{\tau}_i$	Normalized local tangent

List of publications

Articles

1. Investigation of structural models for O–Y and O–Y–Ti clusters in bcc Fe: a density functional theory study

   Muthu Vallinayagam, Matthias Posselt and Jürgen Faßbender, *J. Phys.: Condens. Matter* ***31*** (2019) 095701.
2. Interaction of O–Y and O–Y–Ti clusters embedded in bcc Fe with He, vacancies and self-interstitial atoms

   Muthu Vallinayagam, Matthias Posselt and Jürgen Faßbender, *J. Phys.: Condens. Matter* ***31*** (2019) 485702.
3. Electronic and thermodynamic effects of Zr doping on oxygen vacancy formation in cubic $BaTiO_3$ - ***in preparation***
4. Thermoelectric properties of chalcogenides doped MoS2 layer- A comparison with Janus monolayers - ***in preparation***

Conference contributions

1. *Helium interactions with (Y, Ti, O) nanoclusters in bcc Fe*
   1. EUROMAT - European congress and exhibition on advanced materials and processes, 01.10.2019 - 05.10.2019, Stockholm, Sweden.
2. *DFT studies on the nature of Y-Ti-O nanoclusters in bcc Fe*
   1. The Nuclear Materials Conference, 14.10.2018 - 18.10.2018, Seattle, USA
   2. 14th Int. Conf. on Computer Simulation of Radiation Effects in Solids, 18.06.2018 - 22.06.2018, Shanghai.
3. *Structure and energetics of Y-Ti-O nanoclusters in bcc Fe*
   1. DPG-Frühjahrstagung und EPS-CMD27, 11.03.2018 - 16.03.2018, Technical University Berlin, Germany.
   2. NSF/CECAM school on Computational Materials Science: From Basics to Applications, 17.07.2017 - 27.07.2017, Lausanne, Switzerland.
   3. 4th Int. Workshop on ODS Materials, 26.06.2017 - 28.06.2017, HZDR, Germany

Acknowledgment

It is a matter of joy to express my grateful appreciation to all who have enabled me to accomplish this thesis.

Foremost, I express most sincere thanks with deepest respect to *Prof. Dr. Jürgen Faßbender*, Institut für Ionenstrahlphysik und Materialforschung, Helmholtz-Zentrum Dresden-Rossendorf (FWI, HZDR) for accepting me as his PhD student and giving the opportunity to work and utilize the facilities of FWI*,* HZDR.

It is impossible to express to heartfelt gratitude to *Dr. Matthias Posselt*, FWI, HZDR who have been with me from the first day to till now in Dresden. He had supported me in all moment and has taught me many things. He was so patient whenever I committed mistakes, lagged in understanding thing etc. The inspiration provided by him has certainly promoted my interest towards research work.

I extend my thanks to *Dr. Sharath Chandra,* Scientist, IGCAR, Chennai and Assistant Professor *Dr. Murali Devaraj,* Indian Institute of Information Technology, Design and Manufacturing, Kurnool. *Dr. Sharath Chandra* appreciated me immediately when I have got PhD offer at HZDR. *Dr. Murali Devaraj* had recommended me this institution.

As a theoretician, my bread and butter will be my computer. In this sense, IT people from HZDR and TUD supported me in great deal. They had helped promptly in all computational issues whenever I faced. My special thanks to everyone from IT team.

We need to pull up one another whenever we felt discouraged. In this sense, I am gifted in such a way by having friendly research scholars at HZDR. I have to thank them with big smile. In addition, I thank my friends in Dresden.

At personal note, it is great moment to submit my hearty thanks *Mr. Kumar* and his sister *Ms. Valli* who helped for my education financially. I remember their hard effort to raise funds for my education. In short, you are the major part of who am I today.

Physics is a word bitter fruit for so many students. Only a perfect teacher knows how to make students to eat physics interestingly. In this aspect, I am very gifted by having my physics teacher *Mr. Muthu Krishnan,* Thirthapathi Hr., Sec., School, Ambasamudram who tuned my interest in physics and paved path to my career in physics.

Last not least. Words are insufficient to express my acknowledgements to my parents and my brother, *Mr. Sathaya* for their unconditional infinite patience and love.

Erklärung

Hiermit versichere ich, dass ich die vorliegende Arbeit ohne unzulässige Hilfe Dritter und ohne Benutzung anderer als der angegebenen Hilfsmittel angefertigt habe; die aus fremden Quellen direkt oder indirekt übernommenen Gedanken sind als solche kenntlich gemacht.

Die Arbeit wurde bisher weder im Inland noch im Ausland in gleicher oder ähnlicher Form einer anderen Prüfungsbehörde vorgelegt.

Die vorliegende Arbeit wurde am Institut für Ionenstrahlphysik und Materialforschung des Helmholtz-Zentrum Dresden-Rossendorf e.V., unter der wissenschaftlichen Betreuung von Prof. Dr. Jürgen Faßbender und Dr. Matthias Posselt angefertigt.

Dresden, Muthu Vallinayagam